Mechanical properties of nanoporous metals: model experiments and technology-relevant materials

Vom Promotionsausschuss der
Technischen Universität Hamburg

zur Erlangung des akademischen Grades

Doktor-Ingenieur (Dr.-Ing.)

genehmigte Dissertation

von
Lukas Phillip Cedric Lührs

aus
Hamburg

2020

Gutachter:
Prof. Dr.-Ing. Jörg Weißmüller
Prof. Dr.-Ing. Markus Rutner
Prof. Dr. Erica Lilleodden

Vorsitz des Prüfungsauschusses:
Prof. Dr.-Ing. Dr. h.c. Stefan Heinrich

Datum der mündlichen Prüfung:
20.05.2020

Digital object identifier (DOI):
10.15480/882.2778

Abstract

In this thesis, nanoporous metals are investigated with respect to their mechanical deformation behavior. At small scales, the literature reports distinct strengthening behavior in the form of a "smaller is stronger" relation. Yet, for specimen sizes below around 100 nm, numerical studies predict a reduction in compressive strength due to the action capillary forces at the surface of the material. So far, experiments exploring this notion are missing.

In the present work, nanoporous gold (np Au) is used to investigate this asymmetric yielding by macroscale testing of mm-sized samples. The analysis is based on the concept that uniaxial deformation of networks – such as np Au – contains signatures of both, tensile and compressive deformation. These deformation modes can be identified from the transverse plastic response of np Au during uniaxial compression.

The impact of the surface on the mechanical behavior is systematically varied by thermal tuning of the ligament size and electrochemical modulation. In agreement with theoretical considerations, the experiments find a distinct susceptibility of the transverse plastic response towards the action of capillary forces. Therefore, the present work provides the first experimental proof of surface-induced tension–compression asymmetry at the nanoscale.

Moreover, numerous studies demonstrate that nanoporous metals exhibit considerable application potential as functional materials. Still, the preparation of mechanically robust nanoporous metals with relevant functionality has been limited to precious – and thereby costly – metals.

For these reasons, a novel synthesis procedure is developed to produce cost-efficient nanoporous copper-nickel (np CuNi). By electrochemical dealloying, crack-free macroscopic samples are obtained. A nanocrystalline microstructure is observed with ligament sizes that can be tuned from 13 nm to 40 nm by thermal annealing. Compression experiments on np CuNi find a high strength and considerable plasticity. Electrical potential variations in alkaline electrolyte produce large actuation strains. The measurement serves as a proof of principle for the distinct functionalization potential of np CuNi. This work describes the first successful synthesis scheme for a mechanically robust nanoporous base metal with considerable functionality.

Contents

List of Figures

1 Introduction

1.1 Functional materials based on controlled modification of surfaces

Functional materials exhibit outstanding characteristics due to their native proprietary functions, a considerable advantage compared to conventionally engineered devices with numerous combined components. In this field, nanoporous metals offer many amenities due to their versatile synthesis and functionalization opportunities. Nanoporous metals have been proposed for a variety of applications such as actuators [1–5], sensors [5, 6], catalysts [7–9], bioanalytical systems [10], semiconductor interconnects [11, 12], microfluidic pumps [13], gas filters [14] and energy storage [15]. Moreover, tunable mechanical properties [16–20] have been reported for nanoporous metals and this creates numerous additional application scenarios.

All of the aforementioned studies have in common that their functional properties arise from interactions at the free surface of the material. Surfaces constitute the termination of the bulk crystal, hence the outer atomic layer exhibits reduced coordination compared to bulk lattice atoms, see Figure 1.1 (a). Therefore, the surface's electronic structure differs significantly from the interior material. This aspect can be manipulated to control chemical reactivity [21] and mechanical properties of surfaces alike [22].

Even though surfaces determine the material's interaction with the environment, the influence of surface processes in bulk materials is generally considered small. This is due to the negligible fraction of surface atoms compared to the total volume [23]. However, nanostructured materials may exhibit very high surface area to volume ratios. In these materials, the fraction of surface atoms becomes more pronounced with decreasing feature size (Figure 1.1 (b)). Altered characteristics emerge when surfaces start to dominate the entire material behavior, since surface properties can deviate considerably from the underlying material. Novel design strategies arise as manipulation of surface states allows for direct control of physical and chemical properties and – by implication – the functionalization of the material.

The interfaces of nanostructured materials can be tailored to requirement in several ways: Variation in the elemental composition is an obvious option. Tuning of the microstructural features, such as size [26], local curvature [27] and surface structure [28] affords the alteration of the interfacial contribution, too. While previous methods irreversibly change the surface state, interfaces can also be modified reversibly by exposition to external stimulation. For instance, through the variation of the surrounding gas composition [29] or by electrochemical modulation [3].

Nanoporous metals attract particular interest as they appear as ideal materials for the exploration of various interface-related phenomena. Monolithic metal bodies are formed by homogeneous, bicontinuous nanoscale network structures that can be fabricated in macroscopic dimensions – i.e. several mm or more in size. The small lower size limit of the microstructural constituents – the *ligaments* – combined with a facile size control between a few and several hundred nm enables a convenient way to experimentally single

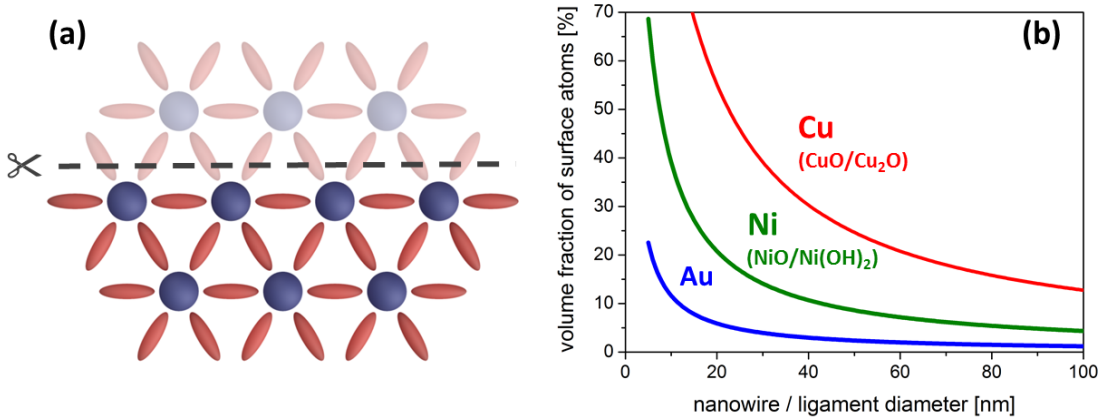

Figure 1.1: Interface contributions in nanostructured materials with high surface area. (a) Schematic illustration of broken chemical bonds at a material's surface. (b) Fraction of surface atoms approximated for cylindrical nanowires and ligament structures. For Au (blue), interfacial contribution is limited to a single atomic monolayer with an estimated size of around 0.3 nm. Under ambient conditions, Ni's native surface layer (green), composed of layered NiO and $Ni(OH)_2$, extends to a thickness of about 1.1 nm [24] whereas Cu exhibits a CuO/Cu_2O passive layer in air of 3.3 nm [25]. Adopted from Reference [23].

out interface contributions on the materials properties. When wetted by electrolyte, nanoporous metals can be used as hybrid systems that enable reversible modulation of the surface state by varying an applied electrical potential [16]. Reaching high structural definition, nanoporous metals appear as excellent model materials in the investigation of small-scale mechanics. Moreover, they promise substantial application potential as mechanically resilient functional materials.

1.2 Synthesis strategies for nanoporous metals

Monolithic bodies of nanoporous metals can be fabricated using a wide variety of synthesizing techniques. In a multiphase alloy, porosity can be obtained by selective leaching of a phase that is rich in less noble elements. In this scenario, the formation of nanoporous bodies requires an interconnected phase structure with a feature size in the nm-range. As a consequence, the morphology of nanoporous metals fabricated by selective leeching is determined by the precursor's microstructure. Nanoporous metals have been prepared by selective leaching of melt-spun foils of spinodally decomposed alloys [30], fine grained microstructures obtained by torsion compaction of metallic powders [31] and precipitates from very large grains or single crystals [14, 32, 33], as shown in Figure 1.2 (a).

A straightforward yet laborious approach to synthesizing nanoporous metals is the utilization of decorated templates. Scaffolds made from polymers [34–36], Silica [37] or other nanoporous metals [38] serve as negative models that are coated with metals. Subsequent selective removal of the template material constitutes the nanoporous metal structure.

Nanoporous metals can also be fabricated by mechanical compaction of self-assembled nanoparticles. Loosely connected particle networks are synthesized through the reduction of metal salts in a solution at room temperature, see Figure 1.2 (b). After drying, the

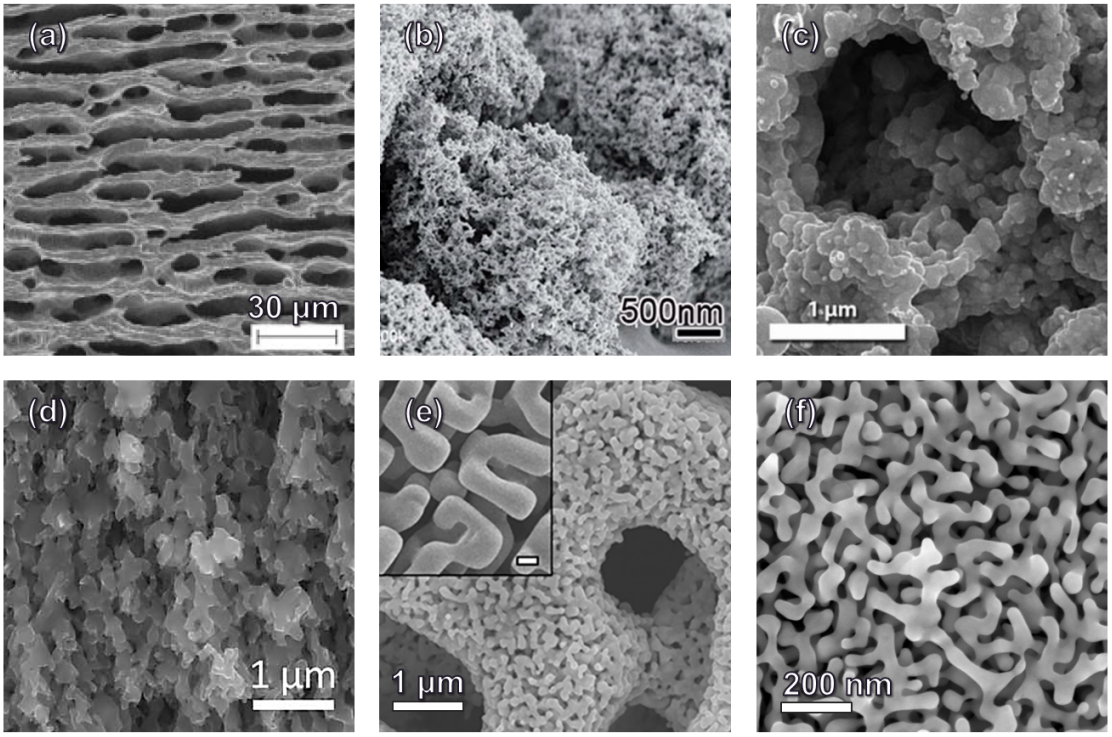

Figure 1.2: Nanoporous microstructures obtained from different synthesis strategies. (a) Superalloy membrane fabricated by selective leeching of precipitates [14]. (b) Self-assembled Ag-nanoparticles prior to compaction [39]. (c) Au-foam synthesized through autocombustion [43]. (d) Directionally grown Al-ligaments made by galvanic replacement [45]. (e) Hierarchical Au-network prepared by reduction-induced decomposition. Inset shows upper hierarchy level [46]. (f) Electrochemically dealloyed nanoporous Au (this work). (a-e) Reprinted with permission.

metallic particles are pressed to from monolithic nanoporous bodies [39–41].

Another processing method for the formation of nanoporous bodies is autocombustion. Metal complexes containing high energetic ligands are pressed into pellets and ignited in an inert gas atmosphere. During the self-propagating reaction, metal atoms are reduced and cluster into nm-sized grains. Agglomeration of the nanograins yield network structures whose spatial arrangement is determined by the evolving N_2-gas [42–44] (Figure 1.2 (c)).

Galvanic replacement has been introduced recently as a processing method to form sheets of nanoporous Al [45] (Figure 1.2 (d)). The replacement reaction takes place between a sacrificial metal sheet and a surrounding salt precursor, e.g. an ionic liquid, comprised of a less active metal. Ions are interchanged between electrolyte and massive material as the salt is reduced by the chemically more active metal sheet. Prerequisite for the formation of an interconnected porous body is that the deposited volume of the inward-growing phase is lower than that of the dissolving sacrificial material [45].

Recently, *Wang and Chen* [46] demonstrated a method for making sheets of monolithic nanoporous metal through reduction-induced decomposition. Precursors of bulk metal salt are immersed in a reducing aqueous environment. During the decomposition, anions are dissolved in the solution while a homogeneous network structure is formed by the metal product [46]. With this method, synthesis of hierarchically structured materials is

rendered possible as shown in Figure 1.2 (e).

Originally investigated as a source of stress-corrosion cracking [47], dealloying of single-phased metal alloys has proven an accessible method to fabricate nanoporous metals with a uniform bicontinuous network and a high degree of structural definition. During dealloying one component is selectively dissolved from an alloy while the remaining atoms rearrange to form the network structure. Selective dissolution can be prompted by evaporation [48] – a recent method to prepare thin nanoporous sheets from melt spun ribbons – and by corrosion in molten metal [49–51] and aqueous electrolytes [52–55] (Figure 1.2 (f)).

Using liquid metal as a dissolution medium requires negative enthalpies of mixing between the sacrificial alloy component and the molten metal. Consequently, the enthalpy of mixing between the persisting component that ultimately forms the porous body and the melt needs to be positive. After solidification, the porosity is obtained through leaching of the dissolution medium. Preparation of porous niobium, titanium and stainless steel have been demonstrated in this way [51,56–58]. However, dealloying in liquid metal typically yields ligament sizes well above a few hundred nm, an aspect that prevents surface-driven functionalization as well as studies on small-scale mechanics.

While many methods are suitable for fabrication of monolithic nanoporous metals, requirements for many technology-relevant applications have yet not been met. Often, samples are limited in size by the processing routine to merely several tens of µm in the smallest dimension [30, 34, 35, 46, 48–50, 59, 60]. Others produce inhomogeneous microstructures [31,39,40,42–44] or exhibit cracks [39–41,45]. So far, dealloying in aqueous media is the only technique to yield homogeneous and mechanically robust bulk samples with macroscopic dimensions – mm-sized or larger – and sufficiently small ligament sizes [52, 61–63]. In general, two methods are used to dissolve the sacrificial component from the precursor alloy: chemical and electrochemical dealloying. Chemical dealloying constitutes a free corrosion process where the less noble component is selectively dissolved in a solution [62, 64–66]. Electrochemical dealloying allows for direct control of the corrosion process by applying an electrical potential [52]. This is of importance as the networks morphology depends on the dissolution rate of metal ions [67], as detailed in Section 2.1.

Yet, good mechanical behavior of nanoporous metals with macroscopic dimensions seems to be limited to precious metals. Plastic deformation behavior – and with that a certain amount of damage tolerance – has been reported for nanoporous Au [61,63,68,69], Pt [70] or Pd [71, 72] during macroscopic mechanical testing. While these materials are highly resistant against environmental influences, they are also expensive.

Cu and Ni appear as economical alternatives for dealloying in aqueous solutions, as they are rather electropositive, compared to other cost-efficient base metals [73]. Nanoporous Cu has been prepared by dealloying from Cu-alloys with different sacrificial components that include Mn [9, 64, 74], Zn [75, 76] and Al [75, 77, 78]. In view of functionalization in various environments, Cu's resistance against degradation strongly depends on the specific environment. Cu is extensively used in seawater, in neutral salt solutions and in organic environment due to its high chemical stability in these media [79]. In air Cu forms a thick oxide layer that passivates the surface [25]. Yet, Cu as well as its oxides readily dissolve in aqueous solutions when in the presence of dissolved oxygen [80] as well as in strong acidic or oxidizing media [79]. Ni, on the other hand, forms a thin and resistant passive layer in air and in numerous acidic and alkaline corrosive environments [24,81,82]. Despite this tendency for passivation, nanoporous Ni has been fabricated from Mn-Ni

precursors by dealloying in acidic media [83–88]. When immersed in alkaline media, Ni exhibits significant functionalization potential as demonstrated by the huge actuation responses observed in nanoporous structures [87, 89, 90], nanohoneycombs [91] and nanowire forests [92]. Furthermore, Ni is widely used as electrode material in batteries such as Ni-metal hydride accumulators [73]. Still, the brittle deformation behavior of nanoporous Ni [87, 88, 90] and Cu [77, 78] demonstrate that preparation of mechanically strong bodies remains a challenge.

1.3 Mechanical properties at small scales

Plasticity

Interface phenomena determine a material's mechanical properties on various length scales. In polycrystalline bulk metal, grain boundaries inhibit dislocation movement that results in a pile-up at the crystal interfaces. The corresponding strengthening effect, σ_h, on the material's strength, σ, becomes more pronounced with decreasing grain size, as described by the Hall-Petch relation via a power-law of the type

$$\sigma_h = kD^n. \tag{1.1}$$

Here, D denotes the average grain size, k is a constant scaling parameter and n represents the power-law exponent that takes a value of 0.5 [93].

A transition from bulk-like to small-scale behavior is observed when the spacing between dislocations in the undeformed microstructure is in the order of the sample dimension. In this size regime, deformation is carried by individual dislocations rather than dislocation networks. For a metal with an initial dislocation density of $10^{12} - 10^{13}\,\mathrm{m}^{-2}$ the transition to small-scale deformation behavior is expected at a sample diameter of around 1 µm and below [94]. Micropillar compression experiments with samples sizes between 0.2 µm and 8 µm find a significant impact of sample size on σ in the form of a "smaller is stronger" relation [95–97]. Here, interfacial strengthening arises from free surfaces rather than grain boundaries. In this size regime a similar power-law relation as in equation 1.1 is observed, where D now indicates the sample diameter and for fcc metals n emerges to values between -0.6 and -1.0, see [98] and references therein. For Au, the size-dependence of the yield strength, σ_y, is shown in region (I) of Figure 1.3. Here, tensile [99, 100] (blue symbols) and compression (red) experiments [97] exhibit similar size-related hardening with $n \approx -0.6$ down to a size of $D \approx 200\,\mathrm{nm}$.

Different models have been proposed for fcc metals in order to identify the underlying mechanisms of the size-dependent strengthening effect. In the following, a brief summary of the two most widespread conceptions is given. The concept known as *dislocation starvation* suggests that, at small sample dimensions, mobile dislocations readily leave the surface rather than multiplying and being pinned by other dislocations [95–97]. As a consequence, the sample becomes depleted of dislocations. Thus, plastic deformation is carried by newly nucleated dislocations, whose formation requires a high stress, rather than by motion or interaction of existing ones. This concept is supported by in situ compression tests on Ni micropillars using transmission electron microscopy (TEM) [101].

A competing interpretation of the size effect at small scales is given by the *single-arm source* model. In this scenario, the sample is not depleted of dislocations but double-pinned Frank-Read sources provide the basis for dislocation multiplication at

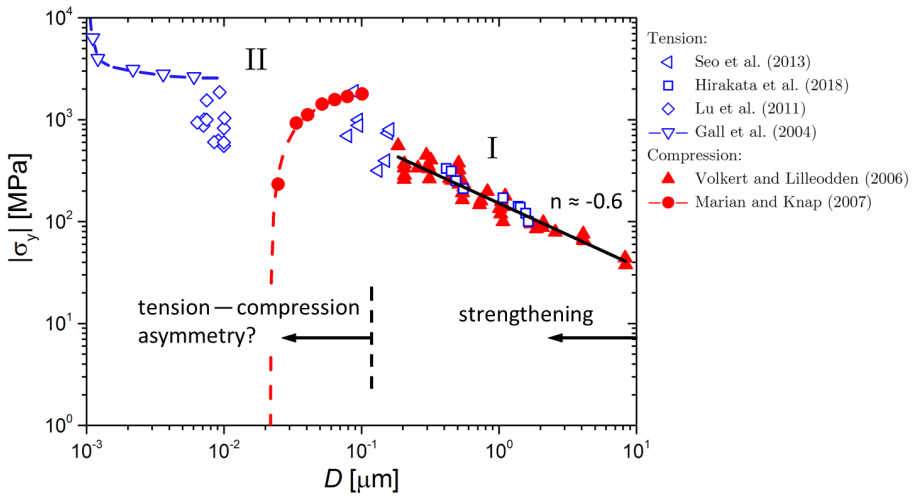

Figure 1.3: Interface-related size effects in small-scale plasticity exemplified on Au pillars and wires loaded in compression (red symbols) and tension (blue), respectively; yield stress, σ_y, plotted versus sample diameter, D. (I) Both, compression and tensile experiments find similar strengthening behavior down to $D \approx 200\,\text{nm}$ [97, 99, 100]. At even smaller length scales (II) experiments [112] and modeling [109] of nanowires loaded in tension observe continuously high and still increasing values for σ_y. Yet, computational modeling suggests a weakening effect in compression at very small scales as a consequence of surface-induced capillary forces [110].

small scales [102–104]. Due to the finite sample volume, the double-ended sources interact upon loading with the free surface leaving two single-armed dislocations behind. Plastic deformation is then sustained by repeated motion of dislocation movement around the pinning points of the single-ended arms. The size-dependence of the yield strength is then ascribed to the stress required to activate the single-armed sources on the dislocation length, which increases with decreasing the sample dimension [102, 105]. TEM investigations on Al [106] and Cu [107] single crystals loaded in tension support the concept of deformation by single-arm dislocation sources, as well.

While the underlying mechanisms are a persisting subject of discussions, the "smaller is stronger" relation has emerged as a widely accepted phenomenon [94]. Indeed, under tensile loading, experiments [100,108] and numerical studies [109] endorse the size-related strengthening correlation down to a few nm in size (blue symbols, region (II), Figure 1.3). However, computational modeling of Au nanopillars in compression suggests an entirely different mechanical behavior at sample sizes below around 100 nm. Instead of continuous hardening, *Marian and Knap* [110] observe considerable weakening with decreasing sample size, see red dots in Figure 1.3. Nonuniform deformation as a consequence of capillary forces [111] is supposed to contribute to this effect [110][1]. Yet, an experimental verification of a surface-induced tension–compression asymmetry in nanoscale plasticity has not been reported at the onset of the present work.

[1]The impact of capillary forces on the mechanical properties is described in more details in Section 2.2

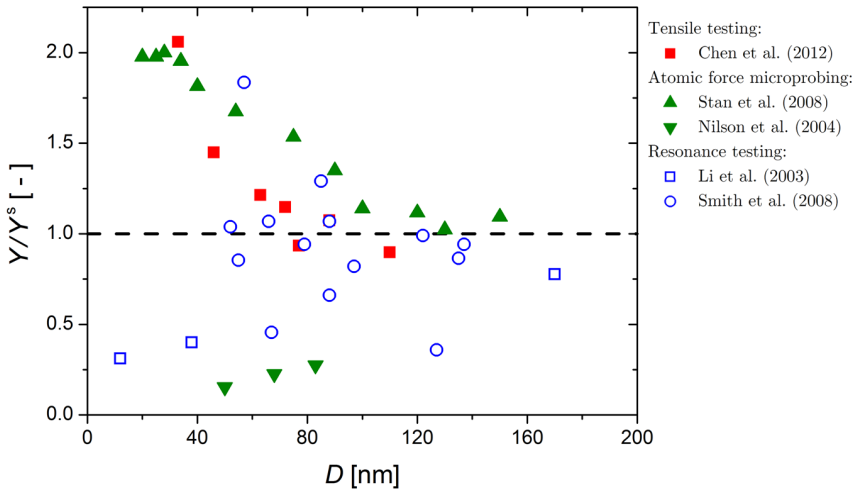

Figure 1.4: Elastic properties at small scales experimentally studied through tensile testing [113], atomic force microprobing [114,117] and resonance frequency testing [116,118]. Young's modulus normalized with respect to the bulk value, Y/Y^s, plotted versus sample diameter, D. Data yields no conclusive support of surface-dominated elastic properties.

Elasticity

The size-dependence of the elastic properties of solids has been a controversial subject of discussion. Experimental studies on nanometer-sized wires, whiskers and cantilevers report contradicting results on extent and even direction of a size effect, as shown in Figure 1.4. Some studies observe size-related stiffening [113–115], others report enhanced compliance [116,117] and even no size-dependence is observed [118], as well. Experimental challenges that emerge from fabrication and testing of individual, nanometer-sized samples are highlighted by a study that finds both, enhanced stiffness and compliance, for the same material [119].

Surface elasticity has been suggested as the source of size-dependency of the elastic deformation behavior [115]. However, the recent *ab initio* investigation by *Elsner et al.* [120] has revealed that contributions of the surface's excess elasticity to the elastic deformation behavior in nanoscale objects is negligible at $D > 10\,\text{nm}$. Even at sample sizes approaching 10 nm experimental uncertainties are currently too large to single out the marginal effect of the surface on the elastic properties [120]. Note that the discussion is so far related to clean metal surfaces only. Surface-related stiffening may still occur by means of adsorbate coverage or electric charging [18].

The impact of nonlinear elastic bulk behavior has also been discussed with respect to the elastic properties [113, 121–123]. At very small scales, the bulk of the material can be subjected to large strains as a result of acting surface stresses. Higher-order elastic parameters may therefore become relevant that promote stiffening or softening, depending on the stress state or the crystallography [121]. However, analogous to the surface elasticity, a significant contribution of this effect to the overall elastic response is merely proposed at sample sizes well below 10 nm [122].

1.4 Deformation behavior of nanoporous gold

Nanoporous metals made by dealloying constitute a unique arrangement of interconnected small-scale elements and a 3D open-pore structure connected to form macroscopic bodies. Studies exploring the mechanical characteristics of these materials have been widely based on nanoporous gold (np Au) [67]. This is due to its outstanding resistance against environmental influences as well as its comparatively easy synthesis procedure.

Early experimental studies on np Au were focused on indentation techniques to examine the material's mechanical response [124–127]. Due to its porous nature, np Au was generally considered to fully densify in the direct vicinity of the indenter tip without lateral deformation [124–127]. The proclaimed lack of constraint around the indenter tip led to the assumption that the measured hardness, H, correlates with the yield strength to $\sigma_y = H$. Advances in the refinement of dealloying protocols enabled production and mechanical testing of np Au with macroscopic dimensions. Under uniaxial compression, *Jin et al.* [61] observed an agreement between indentation and macroscopic testing at a correlation of $\sigma_y = H/3$, which corresponds to the hardness/yield strength relation of massive materials. These findings are supported by recent in situ indentation studies that find extensive deformation zones around the indent with limited densification [128]. Yet, systematic experimental studies exploring the role of lateral deformation during plastic and elastic loading remain to be reported at the onset of this thesis' work.

The mechanical behavior of nanoporous metals has prevalently been discussed with respect to the scaling relations developed by *Gibson and Ashby* [129] for metallic foams. Intriguingly, the model relates mechanical quantities of the foam to the properties of the corresponding massive material, for instance, the yield stress, σ_y, of open-cell foams is expressed as

$$\sigma_y = C_1 \sigma_y^{\mathrm{s}} \varphi^{3/2}. \tag{1.2}$$

Here, $C_1 \approx 0.3$ represents a geometry constant, σ_y^{s} denotes the yield stress of the solid material and φ is the solid volume fraction – or relative density – that is the ratio between the density of the porous and the massive material. Originally, the scaling model was designed for conventional macroscale foams with pore spacings well above 1 µm for which predictions agree very well with experimental findings [130, 131].

For np Au, Figure 1.5 shows a collection of data and model predictions of (a) the yield stress, σ_y, and (b) the Young's modulus, Y. The displayed studies involve molecular dynamics (MD) simulations [122,132], indentation techniques [124,125,127,133,134] and micro-[2] [62,135] and macroscale testing [18,61,68,136,137]. Graph (a) shows that np Au exhibits significantly higher σ_y values than predicted by the Gibson-Ashby relation, if the solid base material is considered as well annealed, massive gold (solid line, $\sigma_y^{\mathrm{s}} = 17.5\,\mathrm{MPa}$ [138]). Yet, since the ligament size ranges between a few tens to a few hundreds of nm, it can be assumed that the strength of individual ligaments – and thus the whole network structure – is severely affected by the size-dependence introduced in Section 1.3. Interestingly, the ligament size of np Au is well in the transition regime between size-dependent strengthening and the suggested tension–compression asymmetry, a chance that will be expanded on later. As a proposition for a more meaningful value of the solid material's strength, σ_y^{s} is chosen to 560 MPa (for a sample size of around 180 nm [97]), as it is the closest available experimental value verging on the suggested tension–compression

[2] Indentation data is plotted as originally reported by the respective authors, i.e. $\sigma_y = H$.

asymmetry transition regime, see Figure 1.3 in Section 1.3. Indeed, with size-depended strengthening accounted for (dashed line), Gibson-Ashby scaling predictions yield decent agreement with the reported yield strength data, especially for micro- and macroscale experiments. The widely observed ligament size dependence of σ_y has also explicitly been accounted for in the modified Gibson-Ashby scaling relation introduced by *Hodge et al.* [127].

Insights into the deformation behavior of the ligament structure of np Au have been the subject of several studies. TEM reveals the generation of dislocations within the individual ligaments [140,141]. The studies propose that during deformation dislocations preferentially glide towards ligament junctions. As a result, a high density of interacting dislocations and microtwins can be found within the deformed ligament nodes. MD simulations find similar dislocation structures in the nodes, yet, the studies also point out the role of dislocation activity at the center of the ligaments as a source of deformation [122,142]. A rather unusual defect feature associated with the crystal structure of the gold ligaments has been observed in a TEM study by *Parida et al.* [143]. During the synthesis of np Au, the grain structure of the precursor alloy is widely retained [61, 143] with only minor dealloying-induced misorientations [144]. Consequently, the ligaments share a common lattice structure as the grain size is in the range of 10 µm to 100 µm and thus around three orders of magnitude larger than the ligament size. Electron micrographs show that ligaments exhibit missing lattice planes of one or more lattice spacing compared to their neighboring element on the other side of the pore [143]. From this, the concept of *pore channel dislocations* has emerged that suggest that ligaments shear along common glide planes with dislocation cores located within the pores [61]. Until recently, ligament bending has been considered the single main deformation mode in np Au [141, 145–147], analogous to the comparatively ordered microstructures of macroporous foams [129]. However, refined numerical modeling by *Jiao and Huber* [148] report a mixed-mode behavior of torsion and bending deformation for randomized np Au network structures.

Investigations of the elastic properties of np Au highlight other interesting aspects of the deformation behavior of nanoporous metals. Similar to the yield strength, the Gibson-Ashby model has been consulted to the prediction and interpretation of ascertained Young's modulus data, Y, see Figure 1.5 (b). For open-porous foams, the scaling of Y with the solid fraction, φ, is predicted as [129]

$$Y = C_2 Y^{\mathrm{s}} \varphi^2, \tag{1.3}$$

with the geometry constant $C_2 \approx 1$ and the Young's modulus of the solid base material, Y^{s}. In case of pure gold, Y^{s} takes a value of 81 GPa [138]. Figure 1.5 (b) shows that trends and values of the experimental data for np Au deviate significantly from the Gibson-Ashby prediction (black, solid line). It can be seen that the model overestimates Y values for $\varphi < 0.35$. This observation is attributed to topological differences between np Au and the model structure underlying the Gibson-Ashby predictions [139]. Within the model conceptions by *Gibson and Ashby* [129], variation in φ merely alters the cell wall thickness. Random field generated structures by *Soyarslan et al.* [139] comprise a morphology that resembles the microstructure of np Au. Topological analysis of these structures show that the scaled genus density[3] systematically decreases with φ, as opposed to the Gibson-Ashby model structures. Most importantly, the study finds a loss of connectivity that

[3]The genus is a topological quantity that describes the number of non-redundant closed connections in a 3D structure. If related to volume and feature size, the *scaled genus density* describes a network's specific connectivity. For details the reader is referred to [149] and references therein.

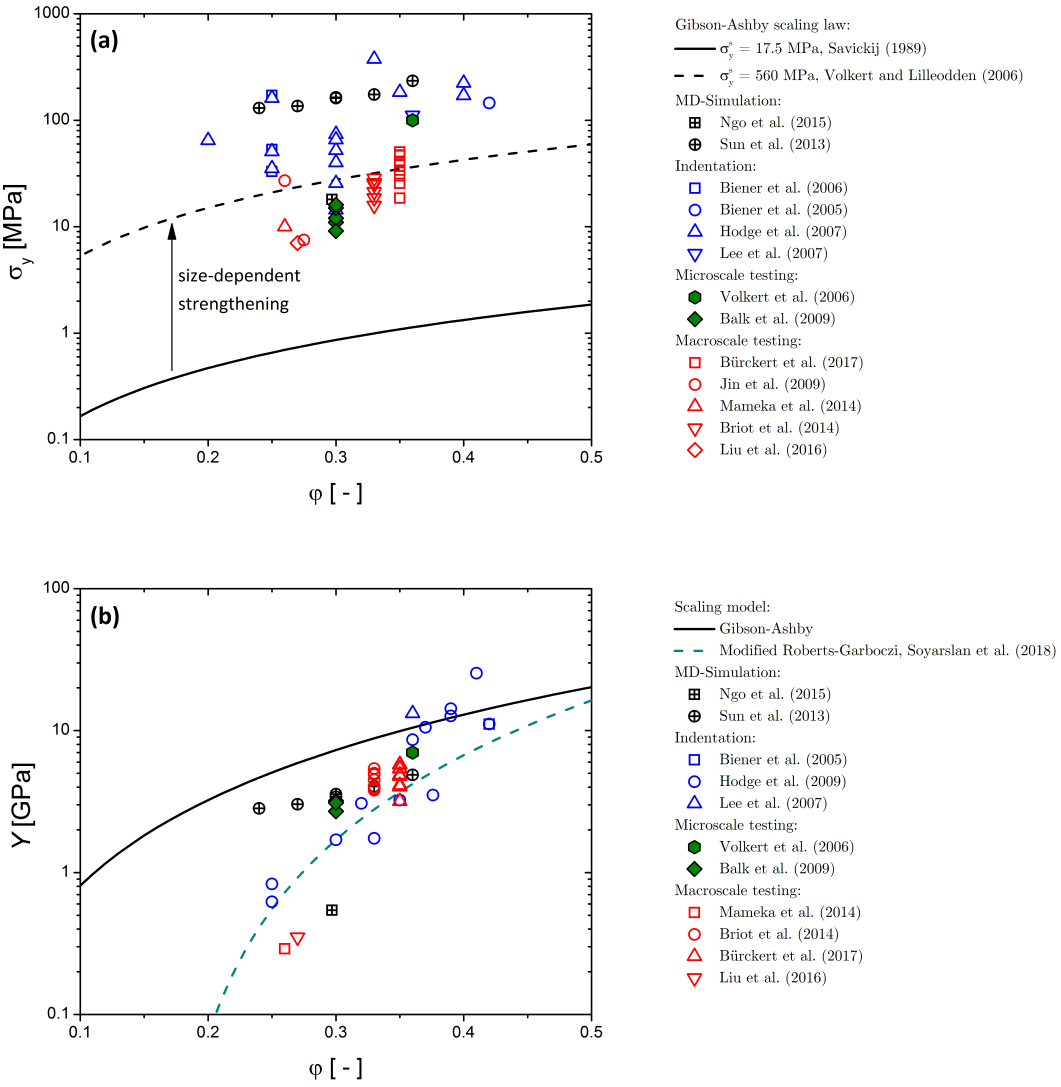

Figure 1.5: Studies and model predictions exploring the mechanical properties of nanoporous gold. Results for various experimental and numerical studies are plotted with respect to the solid volume fraction, φ. (a) Yield stress, σ_y, values significantly exceed Gibson-Ashby predictions for bulk gold (solid line) with $\sigma_y^s = 17.5\,\mathrm{MPa}$ [138]. However, if size-dependent strengthening is considered (dashed line, $\sigma_y^s = 560\,\mathrm{MPa}$ [97]), the model agrees well with the reported data, especially for micro- and macroscale testing. (b) Young's modulus data, Y, find significantly lower values than predicted by Gibson-Ashby scaling for $\varphi < 0.35$. A more suitable agreement is found for the modified Roberts-Garboczi scaling law by *Soyarslan et al.* [139] that accounts for the specific structure of nanoporous gold and its percolation-to-cluster transition at $\varphi \approx 0.16$. Data is collected from References [18, 61, 62, 68, 122, 124, 125, 127, 132–137].

ultimately results in a percolation-to-cluster transition at $\varphi \approx 0.16$ [139]. Both effects are accounted for by a modified Roberts-Garboczi scaling relation (turquoise, dashed line) that agrees well with experimental data.

The study by *Soyarslan et al.* [139] contributes to a recent discussion regarding the role of network connectivity as a source of anomalous compliance variation in nanoporous metals. As described earlier (see Section 1.3), for adsorbate-free metals, surface-related size effects are regarded negligible in the context of elastic properties for sample dimensions above 10 nm. Still, experimental studies on np Au report a significant dependence of the elastic modulus on the ligament size, L [26, 63, 134, 137, 150]. In the adjustment of L, thermal coarsening is employed, a process in which – analogous to the atypical density progression of Y – non-self-similar topology evolution is considered to affect the network's connectivity [63, 137, 151–153]. Yet, tomographic reconstructions of annealed np Au suggest conservation of connectivity during coarsening at large L (> 200 nm) [154–156]. In this context, numerical studies by *Li et al.* [153] point out the decisive impact of solid volume fraction, φ, on the evolution of topology during coarsening. The authors propose that bodies with $\varphi \geq 0.30$ exhibit essentially self-similar structure evolution, while np Au with $\varphi < 0.30$ is subjected to a loss of connectivity [153]. The impact of topology variation on the mechanical properties of network structures is not limited to the elastic characteristics. Rather, plastic deformation behavior is affected by coarsening-related loss of connectivity, as well, for instance in the form of reduced yield strength [123, 157].

Insights into small-scale mechanics

When immersed in electrolyte, modulation of the electrode potential of nanoporous metals allows for a reversible control of the material's surface state. Combined with in situ mechanical testing, the role of the surface on elastic and plastic deformation can be singled out [16–20]. By utilizing this strategy, tensile tests on np Au found a significant impact of adsorbed monolayers of hydroxide ions on the crack propagation and toughness [19]. Moreover, during in situ compressive testing of macroscopic nanoporous bodies electrochemically controlled hydroxide adsorption proves a powerful tool in the manipulation of mechanical properties. Considerable enhancement of the strength [16, 20] and stiffness [18] as well as a reduced creep rate [17] have been reported for np Au, all of which can be repeatedly switched on and off during deformation.

Fabrication and testing of individual samples with dimensions of 100 nm and below is challenging at best. Instead, the stochastic structure and macroscopic sample size of np Au containing up to 10^{15} nanoscale ligaments [123] seem ideal to explore the previously suggested tension–compression asymmetry during plastic deformation. Comparison of uniaxial compression and tension tests might appear as an obvious testing scheme that allows for a straightforward investigation routine. However, while considerable deformability in np Au has been observed in compression testing [61, 63, 68, 69], np Au exhibits brittle failure upon tensile loading [62, 158, 159]. For the latter a weakest-link behavior is suggested [158]. In this concept, collective ligament rupture is proposed that spreads from a single, weakest spot. As a result, the tensile strength is linked to microstructural heterogeneity of the network rather than the deformation mechanisms in the ligaments. Therefore, tensile tests are not beneficial in promoting the understanding of a tension–compression asymmetry.

At the same time, solid network structures exhibit distributions of *local* stress states during deformation. These stresses may deviate in magnitude and even sign from the

average global load. For instance, simulations of random strut networks subjected to uniaxial compression demonstrate that struts aligned with the loading axis are prone to be compressed, while orthogonally oriented ones tend to be stretched [160]. If transferred to np Au, the macroscopic response towards uniaxial compression should inherit a tensile-mediated deformation signature transverse to the loading direction. With the right measurement tools, this intriguing concept facilitates direct insights into the plastic deformation behavior of individual nanoscale ligaments and with that exploration of a possible tension–compression asymmetry, as supported by the results of this work.

1.5 Research objectives and experimental approaches

In the previous sections, it has been highlighted that nanoporous metals are a unique class of materials with great potential as model systems for the exploration of small-scale mechanics. Moreover, the presented application scenarios demonstrate that nanoporous metals appear as promising candidates for functional materials in engineering purposes.

Although nanoscale materials have attracted considerable interest in research and industry for more than three decades, size-related effects on their deformation behavior remain unclear. While the commonly employed concept of a "smaller is stronger" relation appears to be true for specimens subjected to tensile deformation, simulations suggest a breakdown of the strength at sizes below 100 nm during compression. It is argued that the ensuing tension–compression asymmetry can be attributed to the interaction of capillary forces. However, experimental evidence supporting this notion is missing and individual compression tests of nanometer-sized samples prove to be highly problematic. With their combination of small and tailorable ligament size and macroscopic sample dimensions, nanoporous metals appear as optimal candidates to shed light onto this fundamental issue.

It is therefore one aim of this thesis to provide experimental insights into the deformation mechanisms of individual nanoscale objects. For this, an in situ mechanical test setup is developed to measure the elastic and plastic deformation behavior of macroscopic nanoporous samples under uniaxial compressive loading. The analysis is based on the previously introduced concept of local stress state distributions in individual ligaments during deformation of the network structure. By using digital image correlation – an optical full-field measurement technique – compressive- and tensile-mediated deformation contributions may be identified during mechanical testing. In order to single out the role of surface-induced capillary forces, two types of experimental conditions are proposed:

- Variation of the overall surface contribution by thermal tuning of the ligament size.
- Reversible modulation of the capillary forces by electrochemical control of the surface state.

For these studies, mm-sized nanoporous gold samples prepared by dealloying are used due to their high plastic deformability[4] and chemical resilience.

While precious nanoporous metals are well-suited model materials for exploring fundamental aspects of material science, use in industrial application is severely limited due to

[4]Note, even though np Au exhibits significant plasticity in compression, its tensile brittleness leads to the general denotation as *brittle* material. In parts of the scientific community even the notation of *ductility in compression* is rejected. Hence, this work uses the term *deformability* during plastic deformation under compression.

their high price. As detailed above, no nanoporous metal combines affordability with the technologically required high surface area and plastic deformability, so far. Therefore, the second objective of this thesis is the development of a novel nanoporous material solely created from low-priced base metals that meets the following requirements:

- Large and tunable surface area to benefit from surface-related effects.
- High strength and significant plastic deformability during compressive loading.
- Functionalization potential comparable to precious nanoporous metals.

A strategy is explored that aims to develop mm-sized nanoporous bodies made of copper-nickel, a group of alloys also known as *Chinese-* or *German Silver*. Copper-Nickel has been used in coin production for almost two millennia [82, 161], while nowadays its field of application has been extended to modern marine applications due to its excellent corrosion resistance [162, 163]. The concept combines the comparative ease of dealloying and the malleability of Cu with Ni's potential for functionalization. Microstructural analysis techniques, compressive testing and electrochemical surface modulation are used to characterize structural features, mechanical properties and functionalization potential of the material.

1.6 Outline of the thesis

This thesis is structured as follows.

Chapter 2 describes fundamental aspects related to this work. Conventional formation mechanisms during electrochemical dealloying are described in more detail to provide a basis of discussion for the unique microstructure observed in nanoporous copper-nickel. Moreover, the chapter gives a detailed introduction into capillarity at solid surfaces and its susceptibility towards electrochemical modulation. This information is deemed necessary to understand the concept of surface-induced tension–compression asymmetry. Finally, basic concepts of image correlation are presented since all mechanical measurements are analyzed by this technique.

In Chapter 3, experimental details are given to provide insights into the characterization and synthesis procedures. Electrochemical analysis and sample preparation schemes are described as well as mechanical tests and evaluation procedures.

Chapter 4 is dedicated to the exploration of potential tension–compression asymmetry by the action of capillary forces. In the first part of this chapter, results of the microstructural and the mechanical characterization of nanoporous gold are presented. In the second part, these observations are discussed, with a particular focus on the contribution of capillary forces towards the mechanical behavior. Most experimental results and main concepts of this chapter have been published in References [164, 165].

Chapter 5 is focused on the investigation of newly developed nanoporous copper-nickel. In the first part, findings of the detailed microstructural analysis are presented as well as mechanical characterization during compression testing and actuation measurements. The results are discussed in the second part of this chapter with specific emphasis on microstructural the particularities. Experimental observations of nanoporous copper-nickel have partially been published in Reference [166]. The characterization of elemental nanoporous nickel (published in Reference [87]) and nanoporous copper served as a basis of comparison.

Finally, Chapter 6 provides a conclusion of the main findings of this work as well as an outlook on future investigation opportunities.

2 Fundamentals

2.1 Morphology evolution during dealloying

The fundamental formation kinetics are essentially similar among different dealloying techniques [51], regardless whether dissolution of one alloy component is caused by liquid metal, vaporization or corrosion (see Section 1.2). Since this work is focused on electrochemical dealloying, morphology evolution is described with regard to this technique in the following.

Selective dissolution of one component from a massive precursor alloy by means of corrosion requires a difference in corrosion potentials – usually a few hundred millivolts – between the less noble sacrificial constituent and the more noble, stable elements that form the network. The driving force of the electrolytic dissolution process is an applied electrical potential [53]. A single-phase alloy precursor – in the form of either a solid solution or an intermetallic compound – is deemed necessary to produce uniform nanoporous structures [67].

Porosity evolution during dealloying emerges from two kinetic processes: electrochemical dissolution and capillary-driven interface diffusion [167]. The onset of bulk dealloying and with that a significant rise in current occurs when the electrical potential exceeds a composition-depended critical value E_C during a Tafel scan. At potentials below E_C, atoms of the more noble component accumulate and passivate the surface [168]. Above E_C, less noble species are dissolved in a layer-by-layer mode forming growing pits with receding step edges. Instead of remaining as thermodynamically unfavorable adatoms, noble atoms diffuse along the interface to agglomerate into clusters while exposing "new" precursor alloy to the environment, as depicted in Figure 2.1 (a) [53]. As corrosion proceeds inwards, the clustered islands develop into growing mounds enriched of noble elements (Figure 2.1 (b)). First ligaments take on shape as simultaneous growth of pits and mounds causes undercutting of the expanding clusters, as illustrated in Figure 2.1 (c). At these initial stages of dealloying, newly formed ligaments are a few nm in size and still contain a high amount of sacrificial species within the bulk – in the range of a few tens of at.% [169] – as the agglomerated more-noble atoms passivate the ligaments surface [167].

The process that ultimately determines the final morphology and chemical composition of the emerging porous structure is capillary-driven coarsening, as illustrated in Figure 2.2. Following the primary dealloying front, some ligaments increase in size while others are consumed as the more-noble atoms rearrange due to curvature-induced surface diffusion. In the process, clusters of previously screened precursor alloy in the ligament interior are exposed to the surrounding electrolyte. Secondary dealloying further dissolves the less-noble species leading to a significant reduction in residual content [167, 169].

It becomes obvious that the structural evolution during dealloying is a result of a variety of factors that can – to some extent – be controlled accordingly. To name a few, dissolution and interface diffusion rate are determined by temperature [168, 170], pH value and ionic conductivity of the electrolyte [171], alloy composition [172] and

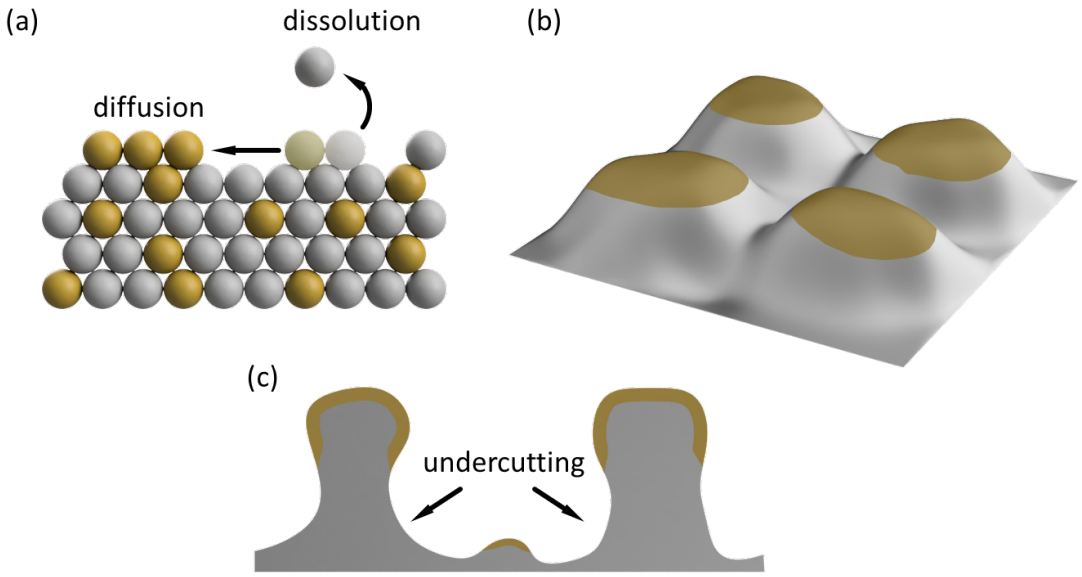

Figure 2.1: Porosity evolution during primary dealloying. (a) Atoms of the less noble species (gray) are dissolved from the alloy while the more noble component (yellow) diffuses along the interface to agglomerate. (b) Formation of mounds enriched of noble elements (yellowish region). (c) Initial evolution of the ligament structure as a result of undercutting of the otherwise passivated mounds.

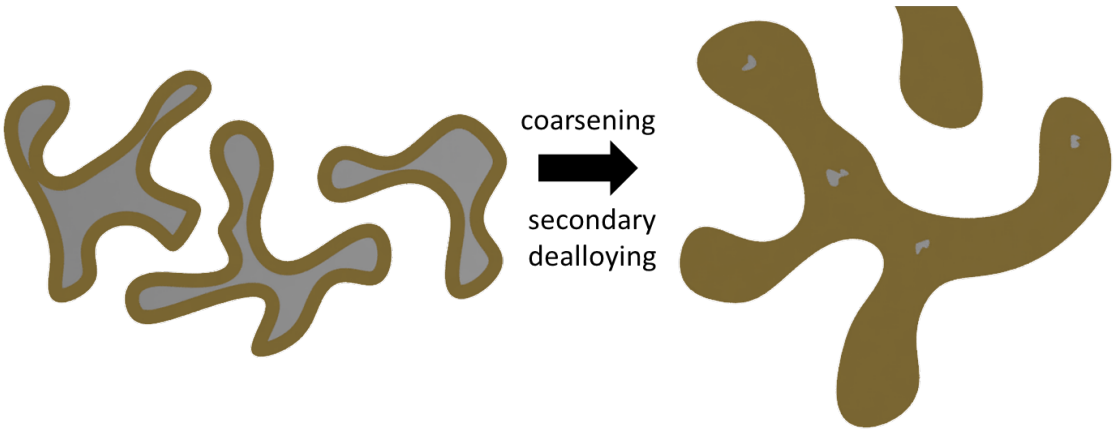

Figure 2.2: Formation of the final ligament structure by concurrent coarsening and secondary dealloying. Atom positions are rearranged as curvature-driven surface diffusion results in a coarsening of the ligament structure. During this process pristine precursor material of the ligament's interior is exposed to the electrolyte and likewise dissolved from the alloy.

applied electrical potential [53,143]. If these kinetic processes can be controlled properly, dealloying can be a versatile technique in the preparation of tailor-made nanostructured materials.

2.2 Capillary forces at solid surfaces

2.2.1 Surface stress and tension of solids – a definition

Surface atoms exhibit a higher energy compared to their underlying bulk. As a consequence, the change in free excess energy, δG, during variation a physical surface area, δA, is the principal thermodynamic quantity in the description of interfaces [173]. Similar to the bulk of a material, extension of a solid's surface area can occur through *elastic* or *plastic* processes, alike. Depending on the mode of surface extension, different variations in δG are found as explained in the following.

During *plastic* surface area formation, atoms are transferred from the bulk into the surface or vice versa, a process that does not alter the atomic structure. Plastic variation of the net area is represented by the *surface tension*, γ, a measure of the excess energy, per area of surface over the bulk energy of a body. In a one-component system, i.e. constant chemical potential μ, constant temperature, T, and constant elastic surface strain, $\mathbf{e}$[1], γ is defined as [22]

$$\gamma = \left(\frac{\delta G}{\delta A}\right)_{\mu,T,\mathbf{e}}. \tag{2.1}$$

The magnitude of the surface tension depends, among others, on the crystallographic orientation of the surface [174]. As a result, solids tend to crystallize in their distinct, faceted shape [175].

In contrast, *elastic* surface area alteration occurs in the form of reversible stretching of a pre-existing surface by $\delta\mathbf{e}$, without addition or removal of matter into or from the surface, respectively. Here, variation of δG is related to the *surface stress*, $\mathbf{s}$, – a second rank tensor that denotes the in-plane stress state – by $\delta G = A\mathbf{s}\delta\mathbf{e}$ [22]. According to Shuttleworth's equation, $\mathbf{s}$ is given in a laboratory frame of reference as [176,177]

$$\mathbf{s}^{\mathrm{L}} = \gamma^{\mathrm{L}}\mathbf{I} + \frac{\delta\gamma^{\mathrm{L}}}{\delta\mathbf{e}}. \tag{2.2}$$

Here, the superscript refers to the coordinate system and $\mathbf{I} = (\delta_{ij})_{i,j\in\{1,2\}}$. The variation of $\mathbf{s}$ with γ is illustrated more clearly by transformation of Equation 2.2 into Lagrangian coordinates: [178]

$$\mathbf{s} = \frac{\delta\gamma}{\delta\mathbf{e}}. \tag{2.3}$$

In this frame of reference $\mathbf{s}$ and γ are measured with respect to the unstrained ($\mathbf{e} = 0$) reference area, A_0. This concise notation will be prevalently used in the course of this work. Lagrangian and laboratory surface area are linked by $A^{\mathrm{L}} = A_0(1+\varepsilon_{\mathrm{plastic}}))$, where $\varepsilon_{\mathrm{plastic}}$ refers to the plastic extension of the surface area [178]. For isotropic surface straining, the scalar surface stress can be simplified to $f = \frac{1}{2}\mathrm{tr}(\mathbf{s}) = \delta\gamma/\delta\epsilon_{\mathrm{elastic}}$, with the

[1] $\mathbf{e}$ is an in-plane strain tensor that designates tangential elastic deformation components at the surface. In normal direction of the surface, relaxation may occur freely.

scalar elastic strain, $\epsilon_{\text{elastic}} = \frac{1}{2}\text{tr}(\mathbf{e})$. While for liquids surface stress and surface tension are identical, values of f and γ can differ in magnitude [179] and even sign[2] [181].

2.2.2 Influence of electrode polarization on capillarity

Metal electrodes in electrolytic environment can exhibit spontaneous or potential-induced polarization of the surface. Numerous studies have demonstrated that *elastic* deformation of solids can be induced through a variation in the applied electrical potential [182–185]. This effect is linked to changes in surface stress, $\mathrm{d}f$, as a result of interfacial charging; denoted by variation in superficial charge density, $\mathrm{d}q$. Both quantities are related by the constant ς, generally referred as surface-stress charge density coefficient to [22, 182]

$$\varsigma = \left(\frac{\mathrm{d}f}{\mathrm{d}q}\right)_{\mu,T,\mathbf{e}}. \tag{2.4}$$

In the vicinity of the potential of zero charge (*pzc*), the surface stress varies linearly with the superficial charge density to [22, 182]

$$\Delta f = f - f_{\text{pzc}} = \varsigma q, \tag{2.5}$$

as illustrated by cantilever-bending experiments of polarized gold in NaF in Figure 2.3. The coupling between surface stress and superficial charging can be exploited for actuation [3, 4] and sensor [6] purposes, provided the system's solid component exhibits a sufficiently high surface area to volume ratio.

A fundamentally different response towards charging of polarizable electrodes is observed for *plastic* surface area formation. For a one-component system, variation in surface tension, $\mathrm{d}\gamma$, during alteration of an applied electrical potential, $\mathrm{d}E$, is described by Lippmann's classical equation as [22, 182, 186, 187]

$$-q = \left(\frac{\mathrm{d}\gamma}{\mathrm{d}E}\right)_{\mu,S,\mathbf{e}}. \tag{2.6}$$

In case of a potential-independent double-layer capacitance $c = \mathrm{d}q/\mathrm{d}E$, capacitive charging at the solid–electrolyte interface can be estimated as [188]

$$\Delta\gamma = \gamma - \gamma_{\text{pzc}} = -\frac{1}{2}\frac{q^2}{c}. \tag{2.7}$$

It can be seen that γ reaches its maximum extent at the potential of zero charge, see Figure 2.3. Accordingly, the superficial charging consistently diminishes a materials resistance against plastic surface formation; for solids and liquids alike [22].

2.3 Surface-induced tension–compression asymmetry?

Simulations of nanoscale elements find asymmetric plastic yielding behavior that is believed to arise from the action of capillary forces, as described in Section 1.3. While the general influence of capillarity on plasticity is not in question, a recent debate ensued on the impact of individual contributions of surface stress, f, and surface tension, γ [20]. Several studies attribute to f a decisive role in the plastic deformation of objects at the lower nanoscale [142, 189–192]. These considerations are based on large bulk stresses,

[2] Note that the value of γ is considered to remain positive in equilibrium states [180].

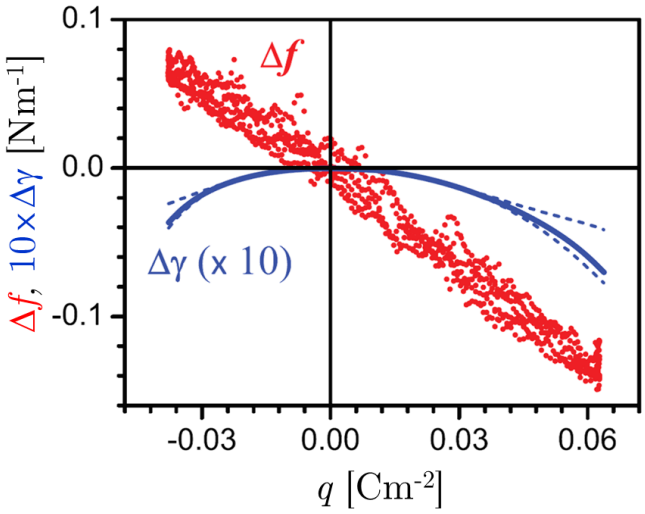

Figure 2.3: Variation of the capillary forces with superficial charge density, q. Experimental data is from cantilever-bending testing of gold during capacitive charging in 7 mM NaF. The data shows linear dependence of the surface stress, f (red), in the vicinity of the potential of zero charge (pzc). In contrast, the surface tension, γ (blue, ten-fold magnification for improved visibility), exhibits an essentially different value evolution with a maximum at the pzc and a parabolic distribution. Reprinted with permission from Reference [22].

σ_C, that are expected to arise for features with very small characteristic radii, r. Imposed stresses are in the order of $\sigma_C \approx f/r$ [193] and can exceed values of a few GPa for nanoscale objects with $f \approx 2\,\mathrm{N/m}$ to $3\,\mathrm{N/m}$ [183]. However, in their study *Mameka et al.* [20] argue that the imposed bulk stress is compensated for by opposite-signed stress in the surface region.

An even more compelling argument that rejects a significant impact of f on plastic yielding is derived from energy-based considerations. Mameka and coworkers illustrate the influence of f on the specific surface energy using the example of a cylindrical nanowire, for which γ ensues as [20]

$$\gamma = \gamma_0 - \frac{3 - 5\nu_E}{4Y} f^2 \alpha. \tag{2.8}$$

With the surface-tension in the unstrained state, γ_0, the elastic Poisson ratio ν_E, the Young's modulus, Y, and the volume-specific surface area $\alpha = A/V$; for a detailed derivation of Equation 2.8 the reader is referred to Reference [20] and its supplementary material. For the example of a Au wire with 111-type surfaces, $\gamma = 1.1\,\mathrm{N/m}$, $f = 3.3\,\mathrm{N/m}$ [194], $Y = 81\,\mathrm{GPa}$ and $\nu_E = 0.42$ [138], even wire dimensions as small as $r = 1\,\mathrm{nm}$ yield a surface stress contribution of merely $0.12\,\mathrm{N/m}$, around one order of magnitude smaller than γ. The influence of f diminishes further with increasing feature sizes. At dimensions of a few tens of nm – which poses the relevant size regime in this work – no significant contribution of f towards plasticity can be expected. In their study, Mameka and coworkers experimentally support these considerations by distinguishing between individual contributions of f and γ on plasticity [20].

Since the impact of f on σ_y is found negligibly small, the surface tension can be identified as the driving capillary force regarding small scale plasticity. During plastic

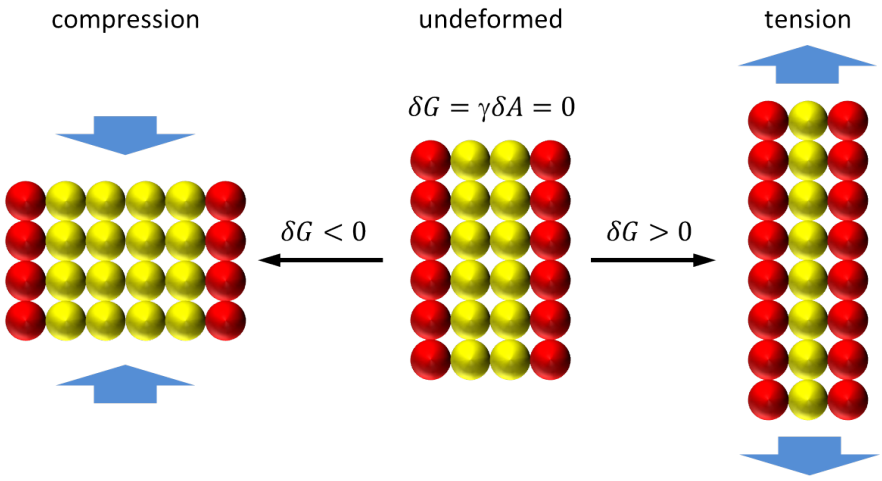

Figure 2.4: Schematic illustration of surface excess energy contribution, $\delta G = \gamma \delta A$, towards plastic deformation of elongated, nanoscale elements. Images depict array of bulk (yellow) and surface atoms (red) with a constant number of atoms in the undeformed state (center) and after plastic deformation in compression (left) and tension (right). Surface tension, γ, causes asymmetric yielding as it promotes compression and impedes tensile deformation.

flow of long objects, plastic changes in surface area entail a variation in surface excess energy $\delta G = \gamma \delta A$ that results in directional strengthening or weakening, as illustrated in Figure 2.4. In other words, the surface tension acts against the formation of new surfaces. This in turn promotes plastic compression ($\delta A < 0$) and impedes tensile deformation ($\delta A > 0$).

Indeed, the impact of surface tension on plasticity has been demonstrated in several studies on creep deformation of µm-sized structures. Zero creep experiments on metal wires at elevated temperatures – pioneered by Udin around 1950 [195, 196] and later extended to multilayers [197] – determine γ by measuring the extra tensile traction, ΔT, required to suppress surface-mediated sample contraction. In these experiments, the surface excess energy contribution exceeds the conventional dissipative forces that resist the deformation. This in turn would lead to shortening of the sample if not compensated for by ΔT. In a steady state, i.e. creep rate of zero, the dissipative forces vanish and for circular wires with the radius, r, the following relation ensues: [195, 196]

$$\Delta T = \frac{\gamma}{r}. \tag{2.9}$$

It can be seen that the zero creep experiments indicate a surface-mediated tension–compression asymmetry of the mechanical behavior at elevated temperature. The action of the capillarity hinders creep deformation in tension but accelerates creep in compression. Similar observations have been reported for materials wetted by electrolyte. Surface polarization has been found to distinctively promote tensile creep deformation [198–200] and crack propagation [201], alike. Both effects can be understood from a reduction in γ as a result of electrode polarization, as described in the previous section.

The impact of capillary forces on the plastic flow behavior may be explored similar to the previously described concepts. Zero creep testing typically uses wires with a diameter of a few tens of µm and very low stresses in the range of merely 0.01 MPa to 0.1 MPa. However, according to Equation 2.9, the stresses required to compensate surface-induced

contraction should increase dramatically for nanoscale objects. For example, in a gold nanowire with a diameter of 10 nm and $\gamma \approx 1.4\,\mathrm{J/m^2}$ a stress of $\Delta T = 240\,\mathrm{MPa}$ is required to compensate contraction. Moreover, plastic variation in surface area requires the same formation energy regardless of whether the deformation originates from creep or plastic yielding. This implies that a 10 nm gold wire exhibits an extra increase in strength of 240 MPa in tension, while the compressive strength is reduced by the same extent. Thus, asymmetric yielding is suggested to result in a directional difference in strength of 480 MPa. A decisive impact on the mechanical behavior of nanomaterials may be expected by this huge contribution.

As described earlier, on a microscopic scale network structures exhibit signatures of both, tensile and compressive deformation contribution, during uniaxial loading. Macroscopically, both deformation modes determine the transverse mechanical coupling behavior. This can be used to determine possible asymmetric plastic flow procured by the surface tension, as it should, theoretically, promote deformation in one orientation – the compression dominated direction – and restrict deformation in the other one – the tensile dominated. A full-field measurement technique that captures the transverse mechanical coupling during deformation is presented in the following Section.

It can be seen from Equation 2.9 that the influence of the surface tension on potential directional strengthening or weakening can be manipulated by different methods: variation of the ligament size, e.g. by thermal annealing, and modification of γ itself, e.g. by controlled polarization. In this work, both concepts will be explored as they offer different characterization opportunities. For instance, ligament size control enables a wide-ranged variation of the surface contribution, while sample polarization enables in situ modulation of γ during mechanical testing.

So far, the impact of capillary forces has only been discussed with respect to the *plastic* flow, neglecting a potential influence of the surface stress on the *elastic* mechanical properties. As described in Section 1.3, for clean metal surfaces the influence of surface stress on the Young's modulus is considered negligible. However, instead of prematurely ruling out a contribution of f – especially since the utilized polarization experiments are partly based on adsorbate covered surface states – the transverse coupling behavior is analyzed in this work during elastic deformation with varying ligament sizes and surface polarization, as well.

2.4 Deformation measurement by image correlation

Digital image correlation (DIC) can be used as a technique to measure surface deformation of solids during mechanical testing. While classical measurement techniques such as strain gauges, extensometers or clip gauges are typically limited to the measurement of a single dimension, DIC affords in situ evaluation of 2D and 3D displacement fields [202]. Among others, full-field characterization offers the investigation of localized strain distribution [203], crack propagation [19] and lateral deformation behavior [204]. These are all aspects that elude conventional testing techniques.

DIC uses gray scale images that are recorded during testing by one (2D) or multiple (3D) digital cameras. Objective of the image correlation is the tracking of individual pixels in subsequent images in order to determine their displacement. The basic concept of DIC will be exemplified on the basis of Figure 2.5 in the following. For an extensive description of DIC Reference [205] is recommended.

In the example in Figure 2.5, an in-plane translational movement of a 5×5 pixel array

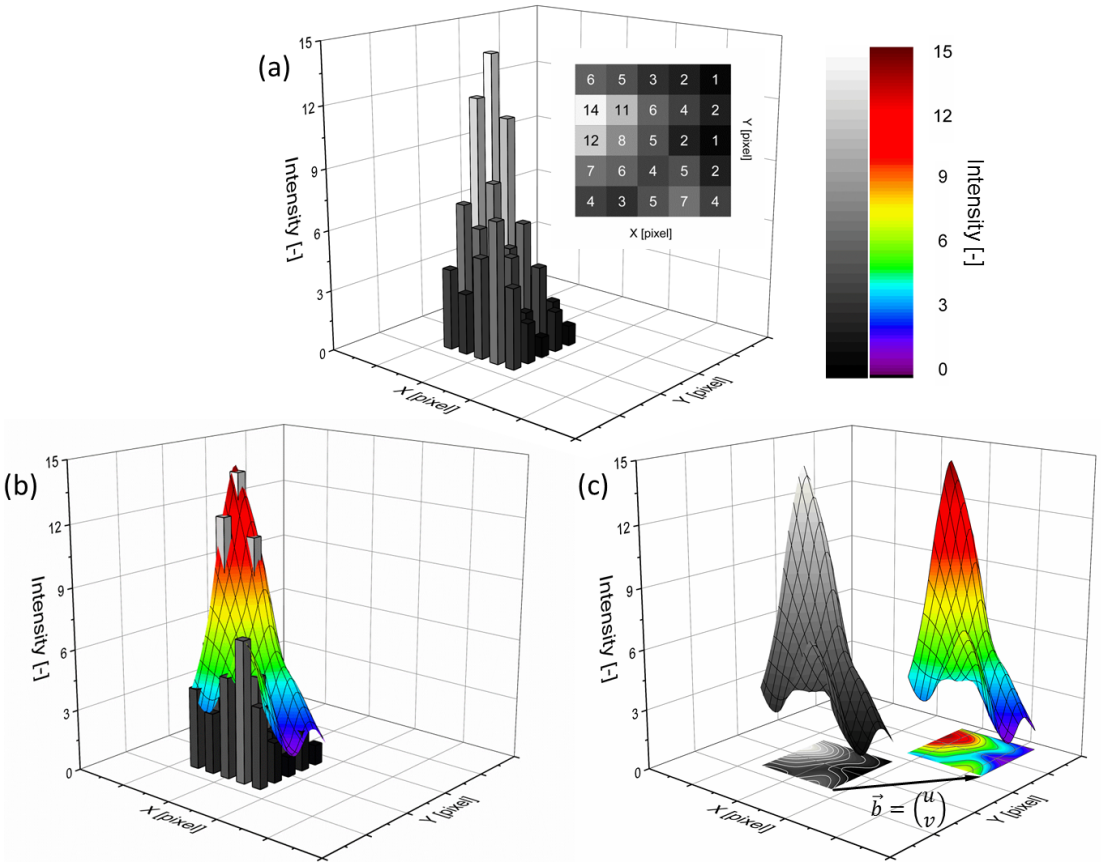

Figure 2.5: General concept of digital image correlation exemplified on a 4 bit subset with a size of 5×5 pixels. (a) Spatial distribution of discrete gray scale values as obtained by digital imaging. Inset shows 2D depiction of the pixel array with corresponding intensity values. (b) Bicubic interpolation (rainbow colored surface) of gray scale values enables matching of the intensity profile in subsequent images. (c) Rigid in-plane motion of the interpolated subset between reference (gray scale coloring) and a consecutive image (rainbow colored scale) by a mean displacement $\vec{b} = (u, v)$. Projection on xy-plane shows interpolated intensity profiles for better comprehensibility.

with an intensity resolution of 4 bit is depicted. Spatial distribution and gray scale values of the individual pixels are given in Figure 2.5 (a). The inset shows a 2D view of the same pixel array with corresponding intensity values. While individual pixels can not be tracked due to the fact that single intensity values are not unique, an array of neighboring pixels – a so called *subset* – may. Next to a sufficiently large subset size, a distinguishable variation of intensity values between neighboring pixels is a prerequisite to the tracking of subsets in subsequent images. In this example, the whole 5×5 pixel array is chosen as the subset.

As digital images consist of pixels with discrete intensity values, it is not possible to track the subsets. In reality pixels are not displaced exactly by an integer multiple of the pixel size between two consecutive images. For this reason, intensity values change with every following image, making it impossible to match a subset to its preceding image. The solution to this dilemma is the interpolation of the intensity values within one subset. This is illustrated in Figure 2.5 (b) by means of a bicubic interpolation approach (rainbow colored surface). The displacement of the resulting 2D intensity profile can be traced in consecutive images through error approximation. From this correlation a mean displacement of the subset center point, $\vec{b} = (u, v)$, is calculated. In case of mere in-plane translational movement all pixels within a subset are displaced by the same vector $\vec{b}$ between reference (gray colored surface) and matched image (rainbow colored surface), as shown in Figure 2.5 (c).

However, if deformation or rotation occurs in consecutive images the subsets are distorted. In this case, the displacement of individual pixels within the subset deviates from $\vec{b}$. Analog to finite element methods, *shape functions* $\xi_i(x_i, y_i)$ and $\eta_i(x_i, y_i)$ are used to transform pixel coordinates in the reference subset, (x_i, y_i), into the new coordinates of the distorted subset (x_i', y_i') as [206]

$$\begin{pmatrix} x_i' \\ y_i' \end{pmatrix} = \begin{pmatrix} x_i \\ y_i \end{pmatrix} + \begin{pmatrix} \xi_i(x_i, y_i) \\ \eta_i(x_i, y_i) \end{pmatrix}. \tag{2.10}$$

An example for a subset subjected to shear deformation and translational movement is given in Figure 2.6. Here, distortion and translation can be described using first order affine coordinate transformation. The position of a point $Q(x_i, y_i)$ in the reference subset (gray scale coloring) can be matched to the distorted subset $Q'(x_i', y_i')$ (rainbow scale coloring) with the mean displacement $\vec{b} = (u, v)$, $\Delta x = x_i - x_0$ and $\Delta y = y_i - y_0$ via [207]

$$\begin{pmatrix} x_i' \\ y_i' \end{pmatrix} = \begin{pmatrix} x_i \\ y_i \end{pmatrix} + \begin{pmatrix} u \\ v \end{pmatrix} + \begin{pmatrix} \frac{\delta u}{\delta x} \frac{\delta u}{\delta y} \\ \frac{\delta v}{\delta x} \frac{\delta v}{\delta y} \end{pmatrix} \begin{pmatrix} \Delta x \\ \Delta y \end{pmatrix}. \tag{2.11}$$

With this set of tools the displacement of every pixel, $\vec{s} = (s_x, s_y)$, within a subset can be calculated. In reality, oversampling is commonly applied by using overlapping subsets to minimize correlation errors, albeit systematic studies investigating this effect have only been reported recently [208]. Most accurate results are achieved when subset center points are set within a *step size* of 20 % to 35 % of the subset size [208].

The strain can be simply computed using finite displacement differences $\varepsilon_{ij} \approx \Delta s_i / \Delta j$. For example, the shear strain ε_{xy} of a pixel at position (n, m) and with a distance, d, between neighboring pixels is calculated as [209]

$$\varepsilon_{xy} = \frac{s_x(n, m+1) - s_x(n, m-1)}{d}. \tag{2.12}$$

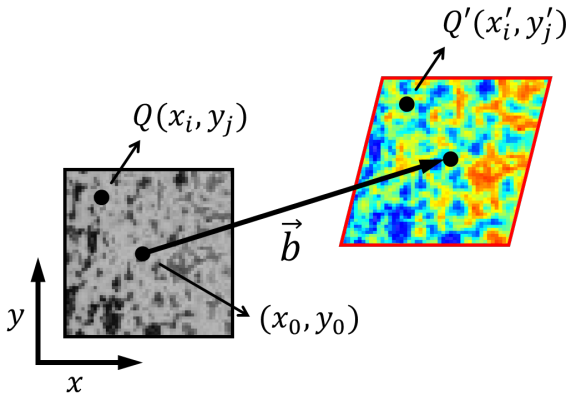

Figure 2.6: Schematic depiction of a subset before (gray scale coloring) and after deformation (rainbow scale coloring). In contrast to rigid in-plane motion, shape functions are required to match off-center pixel displacement during subset distortion or rotation.

While DIC is a powerful measurement technique, its complexity yields a variety of potential error sources. Poor lighting conditions are a common problem during image correlation. These include varying illumination intensity, lack of contrast and specular reflection. Especially the latter proves an often underestimated issue, as specular reflected light depends on the incident angle rather than on the displacement of the samples surface. Diffuse reflection conditions can be accomplished by indirect lighting or use of rough sample surfaces, e.g. base coat paint. Also, out-of-plane motion, Δz, of the recorded object (in 2D) produces errors during calculation of the normal strains ε_{xx} and ε_{yy}. Depending on the distance between object and camera pinhole, z, strain errors due to out-of-plane motion ensue to [205]

$$\varepsilon_{xx} = \varepsilon_{yy} \approx -\frac{\Delta z}{z}; \varepsilon_{xy} \approx 0. \tag{2.13}$$

Strain errors due to out-of-plane displacement can be reduced using telecentric objectives or large working distances between object and camera pinhole. Miscalculation of strains by out-of-plane motion can be entirely circumvented by using 3D DIC with multiple cameras, however, at the cost of increased system complexity [205].

In addition to physical error sources related to the test setup, the imaging and the specimen, algorithms used during image correlation affect the measurement's accuracy, too. Interpolation schemes, shape functions and correlation algorithm all rely on approximations to determine the surface's displacement, thereby – by definition – introducing errors to the analysis [206, 207].

3 Materials and Methods

3.1 Electrochemical techniques

3.1.1 Configuration of cells and electrodes

In this work, electrochemistry not only provided the basis for formation of nanoporosity during sample fabrication, but was also employed to study the effect of surface modulation on the deformation behavior of nanoporous gold (np Au) and the actuation response of nanoporous copper-nickel (np CuNi). The electrochemical experiments used potentiostats in a three-electrode configuration as schematically shown in Figure 3.1. In this electrode setup, the working electrode (WE) designates the site where the desired reactions occur. The electrical potential is controlled with respect to a reference electrode (RE); the resulting current passes between WE and a counter electrode (CE).

To provide stable and reproducible potential control, a general requirement for a RE [210], Ag/AgCl was chosen as reference system for all but alkaline solutions; here, a commercial Hg/HgO electrode was employed. Preparation of np CuNi by electrochemical dealloying and voltammetric sweeps of the elemental precursor constituents (see Section 3.2.1) used a commercially available electrode. Here, a AgCl-coated silver wire is immersed in 3 M KCl reference solution and separated from the surrounding electrolyte by a glass frit. This system allows for stable, pH-independent measurement of the electrical potential with a constant potential offset of +210 mV versus the standard hydrogen electrode (SHE). As ions need to migrate through the separating frit into the reference solution, ion exchange also occurs in opposite direction. For instance, Cl^- ions can migrate from the reference solution into the electrolyte. This effect becomes problematic when WE and CE are susceptible to side reactions with ions from the reference solution. In case of gold, presence of even small amounts of Cl^- ions cause dissolution of Au into $AuCl_4^-$ at dealloying potentials of np Au [211]. For this reason, pseudo Ag/AgCl reference electrodes were employed in all studies involving np Au. In opposition to a conventional RE, pseudo REs are directly immersed into the electrolyte. This avoids contamination of the electrolyte due to the absence of a reference solution. A pseudo RE needs to be calibrated in every environment since its electrical potential is not fixed but depends on the composition of the electrolyte.

Pseudo REs were fabricated by electrolytic coating of Ag wires (99.99 % metal base purity) with AgCl in 1 M HCl. The preparation used a constant potential of 1 V applied versus another silver wire (configured as RE and CE). As the pseudo Ag/AgCl electrode's potential depends on the surrounding electrolyte, all pseudo REs were calibrated against a reversible hydrogen electrode (Gaskatel, Hydroflex) in the respective solution.

The small installation space occupied by the flexible self-made pseudo REs is another important aspect for their usage during electrochemical experiments. While commercial REs are rigid and large in size, Ag/AgCl pseudo REs can be installed in the miniaturized electrochemical cells that are used in electrochemomechanical testing (see Section 3.3.5).

Counter or auxiliary electrodes are selected to be chemically inert under the applied electrochemical reaction conditions. Moreover, in order to balance reactions occurring at

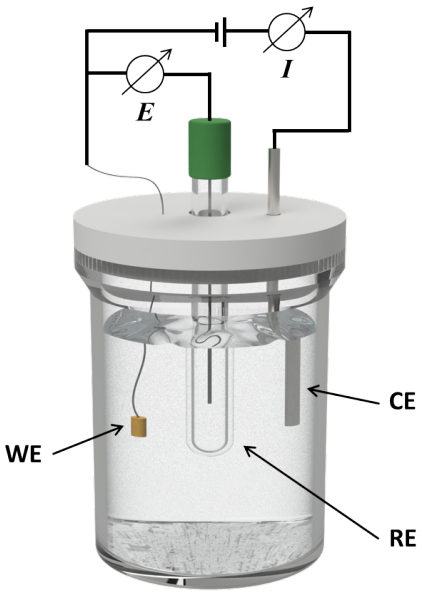

Figure 3.1: Schematic illustration of an electrochemical cell utilized for dealloying in aqueous electrolytes. A three-electrode setup – composed of working (WE), reference (RE) and counter electrode (CE) – allows for a stable, potential controlled corrosion process.

the WE, the CE requires a surface area of similar or greater size than the WE to avoid interference with the measured reaction. Specifics on CEs and electrolytes can be found in the respective section.

All electrochemical experiments were exposed to air and conducted at room temperature. Aqueous solutions were prepared with high purity water ($\geq$ 18.0 MΩ cm). For comparability, electrical potential data is presented with respect to the standard hydrogen electrode (SHE).

3.1.2 Chronoamperometry

Electrochemical experiments were configured by the software NOVA (Metrohm, Version 1.10) and performed using potentiostats of the PGSTAT-series (Metrohm, Models 30, 100, 101, M204 and 302N). In this work, chronoamperometry was employed during materials synthesis as well as for in situ surface modulation of nanoporous metals during mechanical testing, as detailed in Section 3.3.5 of this chapter.

Chronoamperometry produces a series of potential steps between WE and RE for defined time intervals during which the electrical potential, E, is kept constant. The resulting current, I, is monitored continuously during the procedure. An example for a chronoamperometric measurement is given in Figure 3.2. The plot shows a dealloying and polarization routine used in the synthesis of np CuNi. Two potential steps (dashed blue line) are shown and a current (solid red line) that primarily originates from anodic dissolution of Mn^{2+} ions, as detailed in Section 3.2.1.

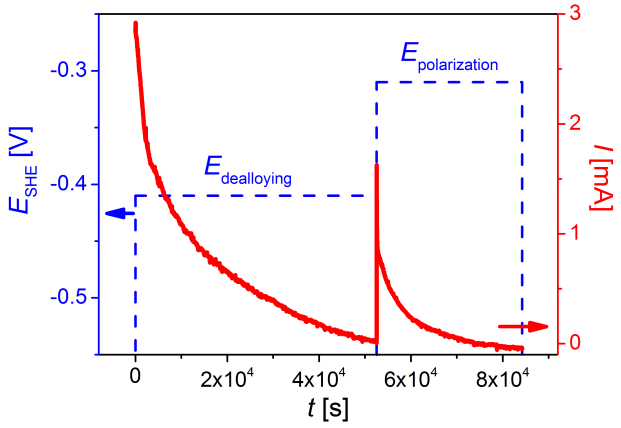

Figure 3.2: Two-step chronoamperometry procedure demonstrated on a dealloying process forming nanoporous copper-nickel. Applied step potentials, E, (dashed blue lines) and corresponding current, I, (solid red line) are plotted vs. time, t. The porous structure evolves at a constant applied electrical potential, $E_{\text{dealloying}}$, through the dissolution of Mn^{2+} ions. An additional polarization step, $E_{\text{polarization}}$, further reduces the residual Mn-concentration of the nanoporous structure.

3.1.3 Voltammetry

Voltammetry involves the imposition of quasi-linear potential variations on the WE with simultaneous recording of the current [210]. A linear potential progression is generated from a series of discrete potential steps and applied with a mean scan rate, $v = dE/dt$, between $1\,\text{mV}\,\text{s}^{-1}$ and $20\,\text{mV}\,\text{s}^{-1}$, depending on the measurement scenario. This "staircase" technique was selected as it enabled slow scan measurements ($v < 10\,\text{mV}\,\text{s}^{-1}$) as opposed to experiments in linear, i.e. continuous, scan mode.

Note, that positive going currents are designated as *anodic* and negative going currents as *cathodic* [210]. In this work, two types of voltammetric measurements have been employed: linear sweep and cyclic voltammetry.

Linear sweep procedures consist of a single anodic potential progression from low, E_{low}, to high potentials, E_{high}. These measurement protocols yield polarization curves that are used to identify dissolution potentials of metals in their respective electrolytic environment [212], as demonstrated in Section 3.2.1.

During cyclic voltammetry (CV), a series of alternating anodic and cathodic potential sweeps is employed on the WE to produce a triangular waveform bounded by preselected E_{low} and E_{high}. A measurement of nanoporous gold imposed to cyclic voltammetry in $1\,\text{M}\ HClO_4$ at a scan rate of $1\,\text{mV}\,\text{s}^{-1}$ is shown in Figure 3.3. Graph (a) demonstrates the generated potential waveform of one cycle (solid line) plotted versus time; dashed lines indicate following potential cycles. The current response as a result of the variation of the electrode potential is recorded in the so-called voltammogram; see Figure 3.3 (b), scan directions are indicated by arrows. In these measurements, every energetically different reaction on the electrode's surface results in a current [213].

For instance, in case of np Au two distinctive regimes can be identified from the voltammogram in Figure 3.3. At low potentials of up to around 1 V versus SHE (I, light region in graph), capacitive charging through the formation of an electrical double layer is the

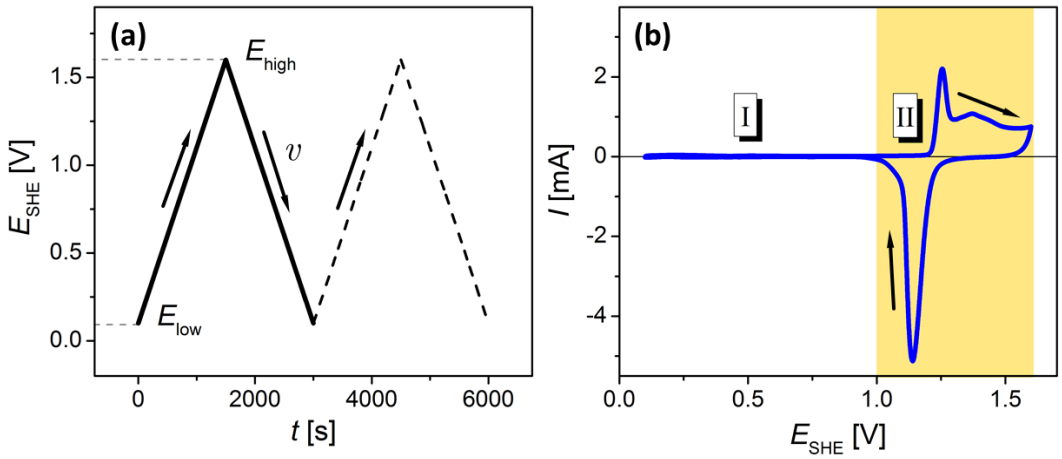

Figure 3.3: Nanoporous gold analyzed by cyclic voltammetry at a scan rate of $v = 1\,\mathrm{mV\,s^{-1}}$ in 1 M $HClO_4$ electrolyte. (a) Triangular waveform of a potential cycle imposed on the working electrode between E_{low} and E_{high} plotted vs. time, t. (b) Resulting cyclic voltammogram with anodic and cathodic scan direction indicated by arrows. Two distinctive current-potential regions appear that are linked to the materials surface state: capacitive double layer charging (I, light region in graph) and chemisorption of oxygen species (II, shaded region).

only reaction that can be observed on the gold surface [214]. At high potentials ($> 1\,\mathrm{V}$), pseudocapacitive processes occur in the form of reversible oxidation (anodic scan) and reduction reactions (cathodic). In the voltammogram, these redox reactions are indicated by the shaded region in Figure 3.3 (II). During anodic oxidation, monolayer adsorption of OH-species on the gold surface occurs along a potential range leading to a current plateau rather than a sharp peak at a discrete potential value. During cathodic scanning, the entire monolayer is removed in a single reduction peak leading to an adsorbate-free, metallic gold surface [215]. The origin of the resulting hysteresis is attributed to gradual changes in the nature of the oxide film during the formation reaction, for further details the reader is referred to Reference [215]. Finally, electrochemical scans may also entail faradaic, i.e. non-recoverable, reaction contributions. In this context, hydrolysis represents a typical example of faradaic currents during CV of np Au in 1 M $HClO_4$: if E is applied beyond the stability range of H_2O, gaseous hydrogen or oxygen form at the electrode surface and are released into the environment. Moreover, faradaic reactions may be triggered by impurities within the electrolyte. For this reason, electrolytes were purged with argon gas prior to voltammetric analysis.

In this work, CV was used to reduce the residual Ag content during np Au fabrication (Section 3.2.3), as well as to quantify the impact of electrochemical polarization on the surface tension at any given potential as described in Section 3.3.3. Finally, actuation measurements of np CuNi used CV to correlate electrochemical reactions to the induced deformations (Section 3.3.6).

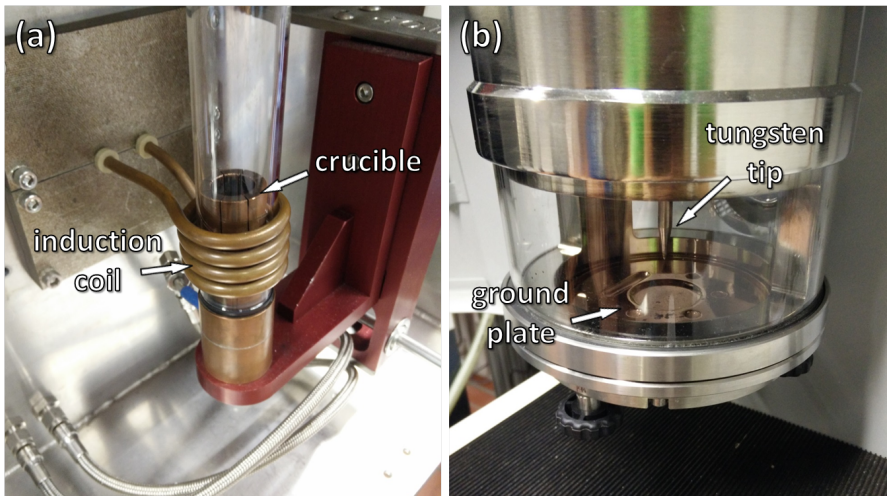

Figure 3.4: Photographs of the melting furnaces used for alloying. (a) Induction furnace used for the preparation of $Cu_{20}Ni_{10}Mn_{70}$ alloy. Both, coil and crucible are cooled during induction heating. (b) Arc melter employed for alloying $Au_{25}Ag_{75}$ precursors. The argon plasma is ignited and maintained between the tungsten tip and the cooled copper ground plate.

3.2 Preparation of bulk nanoporous metal by dealloying

3.2.1 Nanoporous copper-nickel

Developing ductile nanoporous base metals has proven a problem and remains to be solved. However, as long as requirements described in Section 1.2 are met, electrochemical dealloying is a technique that should – in principle – produce non-precious nanoporous metals with macroscopic dimensions and plastic deformation behavior. This work's approach to fabricate nanoporous copper-nickel is presented in the following.

Cu and Ni metal wires (99.98+ % metal-base purity, ChemPur) and electrolytic Mn granulate (99.99 %, ChemPur) provided the basis of the $Cu_{20}Ni_{10}Mn_{70}$ precursor alloy. Prior to alloying, superficial oxides of Mn granulates – a residual from the manufacturer's electrowinning process – were dissolved using 1 M oxalic acid. Alloying of electrolytic Mn requires carefully controlled heating conditions since Mn exhibits a high vapor pressure at its melting point [216]. This necessitates a fast melting procedure with little overheating. Simultaneously, the high sensitivity towards thermal shocks that is displayed by the granulates needs a homogeneous heating process. The aforementioned alloying conditions were met by melting the precursor materials in a cold-crucible induction furnace in argon atmosphere at a pressure of around 0.7 atm, see Figure 3.4 (a).

At elevated temperature, alloys composed of Cu, Ni and Mn are miscible and can be homogenized into a single-phase solid solution [217]. This is a prerequisite for uniform morphology formation, as detailed in Section 1.2. At room temperature, multiple phases are expected in equilibrium for ternary Cu-Ni-Mn alloys. The estimate is based on the binary phase diagrams depicted in Figure 3.5. This is due to the fact that there are no comprehensive ternary phase diagrams available for the Cu-Ni-Mn system at low temperatures. In order obtain a single-phase solid solution, the precursor alloy was annealed in argon gas at 850 °C for around 12 h and subsequently quenched in water. The resulting master alloy was turned into rods with a diameter of around 1.1 ± 0.05 mm

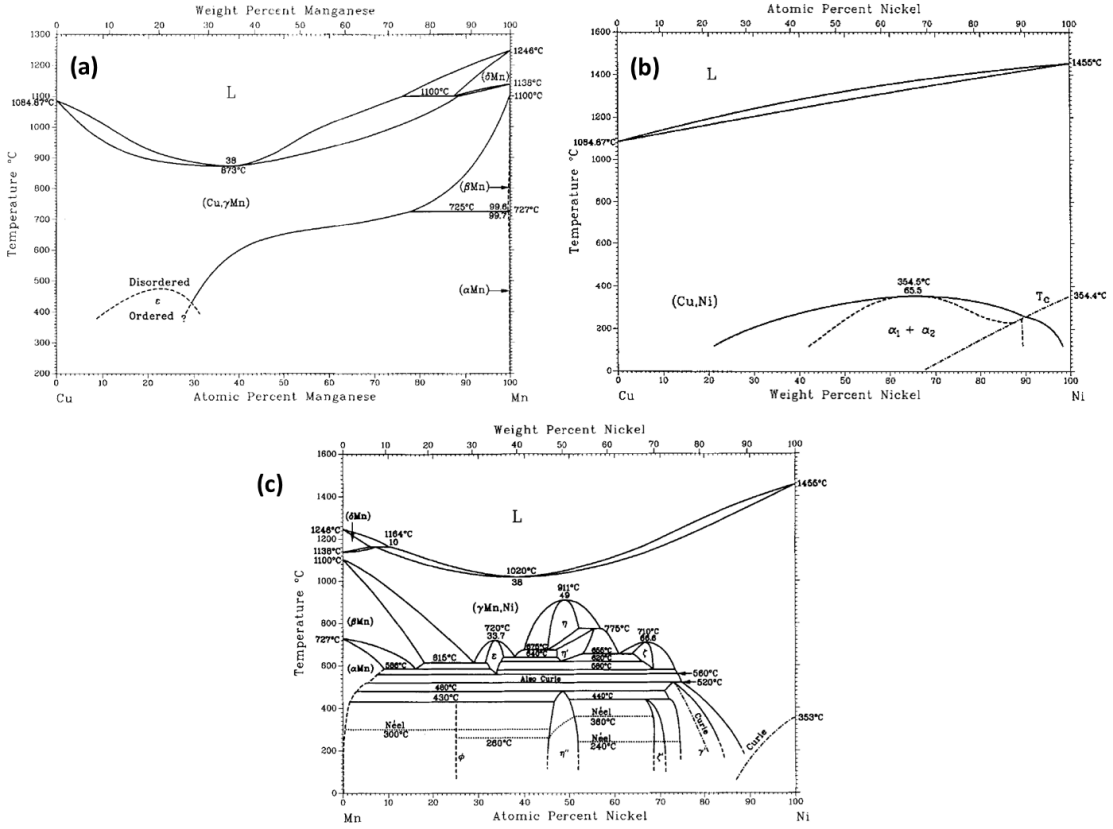

Figure 3.5: Binary phase diagrams of the copper-nickel-manganese (Cu-Ni-Mn) system. The graphs are for: (a) Cu-Mn [219], (b) Cu-Ni [220] and (c) Mn-Ni [221]. The graphs are reprinted with permission.

using a lathe and then cut into cylinders with a length of 1.8 ± 0.1 mm. These dimensions were chosen in accordance with compression testing schemes derived for metallic foams that suggest sample aspect ratios ≥ 1.5 [218].

Sufficiently large differences in corrosion potential between dissolved and remaining species of atoms are a prerequisite for successful dealloying. In this context, a frequently consulted parameter for the estimation of electrochemical activity in aqueous solutions is the standard potential, E_0, [222] which refers to the element's potential in a model electrolyte, i.e. at 25 °C, pH = 0 and a metal ion concentration of 1 M [73]. In case of $Cu_{20}Ni_{10}Mn_{70}$, a large difference in standard potentials is easily met as E_0 of Cu and Ni are significantly more positive than Mn[1]. However, as E_0 describes the pure metal's activity under model conditions, corrosion potentials deviate from E_0 in electrolytes with a pH $\neq 0$ or with complex-forming species such as F^-, Cl^- or NH_3 [73].

Dealloying of the $Cu_{20}Ni_{10}Mn_{70}$ master alloy was carried out in an aqueous electrolyte composed of 10 mM HCl (≥ 99 % purity) and 1 M KCl (≥ 99.5 %). In this solution, hydrochloric acid controls the pH value that is measured as 1.8 (Gaskatel, pHydrunio) and – as a consequence – the Mn^{2+} activity. Addition of potassium chloride ensures a high ionic

[1] E_0 =+340 mM, −257 mM and −1180 mM vs. standard hydrogen for Cu/Cu^{2+}, Ni/Ni^{2+} and Mn/Mn^{2+} redox systems, respectively [73].

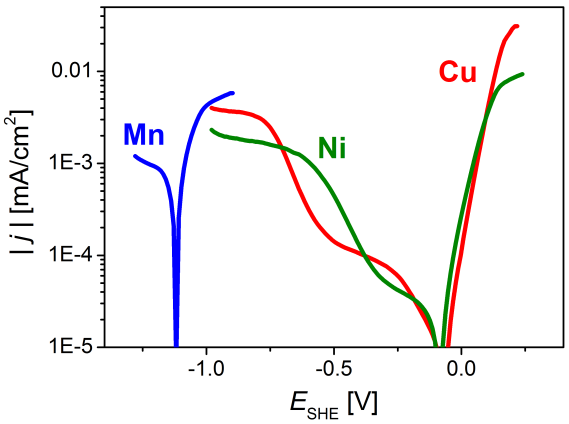

Figure 3.6: Polarization curves of pure metals obtained from linear potential sweeps with a scan rate of $20\,\mathrm{mV\,s^{-1}}$ in 10 mM HCl + 1 M KCl electrolyte. A difference of around 1 V in corrosion potentials is observed between Mn and the more noble Ni and Cu.

conductivity. Polarization curves of pure Cu, Ni and Mn[2] were derived from potential sweeps at a scan rate of $20\,\mathrm{mV\,s^{-1}}$ which are shown in Figure 3.6. In these experiments, carbon cloth served as CE. In contrast to their standard potentials, Cu and Ni exhibit an essentially similar corrosion potential of around $-0.1\,\mathrm{V}$ in the present electrolyte. These potentials designate the upper limit for stable electrochemical dealloying of np CuNi. At a corrosion potential of roughly $-1.1\,\mathrm{V}$, Mn dissolution imposes the lower limit of the dealloying window. The large difference in dissolution potentials – around 1 V – between sacrificial and remaining species easily meets the required electrolyte conditions.

Electrochemical dealloying was conducted in an electrolyte-filled glass cell (Figure 3.1). In this setup, the precursor alloy was clamped and electrically connected with a gold wire (WE), while a graphite rod served as CE. Two-step chronoamperometry was applied at a constant electrical potential of $-410\,\mathrm{mV}$ vs. SHE, which was stopped when the current dropped below $10\,\mu\mathrm{A}$. To further remove residual Mn, the material was subsequently polarized at $-310\,\mathrm{mV}$ until the current diminished to zero (Figure 3.2).

After dealloying, the pore space is filled with aqueous electrolyte. During drying in air this induces a pressure, Δp, at the drying front according to the Laplace equation for a completely wetted material of [223]

$$|\Delta p| = \frac{2\gamma_{\mathrm{LV}}}{r}, \tag{3.1}$$

where γ_{LV} denotes the surface tension between liquid and vapor phase and r refers to radius of the meniscus which is close to the radius of the pore [223]. Equation 3.1 emphasizes that capillary stresses can be considerable during drying of nanoporous metals as Δp takes on a value of a few tens of MPa for materials with a pore size ranging between 10 nm to 30 nm if filled with water ($\gamma_{\mathrm{LV}} = 72\,\mathrm{mJ/m^2}$ [223]).

With the aim of avoiding capillary-force-induced cracks, a drying procedure adopted from Reference [223] was used, as follows. Subsequent to dealloying, the wet nanoporous samples were immersed in ethanol for around 2 h followed by n-pentane for $\geq 12\,\mathrm{h}$ and

[2]For Mn, instead of granulates, a metallic rod with a purity 99.99 % was measured.

finally dried in air. This procedure profits from the considerably lower surface tension of n-pentane – $\gamma_{LV} = 14\,mJ/m^2$ as opposed to $72\,mJ/m^2$ of water – which reduces drying-induced stresses significantly.

Ligament sizes were controlled by annealing a fraction of the samples in purified argon gas (O_2 and H_2O content < 1 ppm) at 400 °C for 20 min, 30 min and 45 min.

3.2.2 Elemental nanoporous copper and nickel

One objective of this work is the synthesis of np CuNi since the alloy – ideally – combines amenities of both main constituents. In this view, fabrication and testing of elemental nanoporous copper (np Cu) and nickel (np Ni) samples appears a suitable basis of comparison in the evaluation of np CuNi. Since the general fabrication scheme of np Cu and np Ni closely resembles preparation of np CuNi, both procedures are described briefly in the following.

Both master alloys – $Cu_{30}Mn_{70}$ and $Ni_{30}Mn_{70}$ for np Cu and np Ni, respectively – were alloyed by induction melting. Moreover, similar heat treatment as in np CuNi was applied to produce a solid solution. Prior to dealloying, precursors were cut into mm-sized cuboids with a similar aspect ratio as np CuNi.

Np Cu was prepared by electrochemical dealloying in 1 M $(NH)_2SO_4$ at a constant electrical potential of −600 mV vs. SHE.

Synthesis of np Ni was based on free corrosion in 0.2 M $(NH)_2SO_4$ at a temperature of 55 °C for 20 h to 38 h.

After dealloying, both materials were dried similar to np CuNi. In this work, structural analysis and mechanical testing is limited to as-prepared np Cu and np Ni samples since annealing either leads to immediate crumbling or, at the very least, significant weakening. Therefore, no meaningful data was obtained from compression tests of annealed np Cu and np Ni.

3.2.3 Nanoporous gold

Synthesizes of np Au used $Au_{25}Ag_{75}$ precursor alloys made from pure Ag and Au wires (both 99.99+ % metal base purity, ChemPur). Alloying was carried out in an arc melting furnace (see Figure 3.4 (b)) under argon atmosphere (0.7 to 0.9 atm). Afterwards, the alloys were encased in evacuated quartz tubes and homogenized at 850 °C for around 5 days. Since Ag and Au are miscible along the whole composition and temperature range [224], no further heat treatment of the precursor alloy was required.

Wires were drawn from the master alloy and cut into cylinders with a length of around 1.9 ± 0.1 mm and a diameter of 1.0 ± 0.1 mm. During the drawing process and after cutting into cylinders, the material was annealed repeatedly to annihilate any effect of work hardening. In 1 M $HClO_4$ solution (≥ 99 % purity) with a pH value measured as 0.4, electrochemical dealloying used a potential of 1250 mV vs. SHE. To remove residual Ag and adsorbed oxygen species [2], subsequent polarization at 1350 mV vs. SHE was applied for 20 min followed by 20 potential cycles (0.1 V to 1.6 V at $5\,mV\,s^{-1}$) ending at 0.8 V. This corresponds to an adsorbate-free surface state. Afterwards, the samples were rinsed in H_2O and dried in air.

One strategy of exploring the impact of capillary forces on the mechanical behavior is controlled variation of the surface area. In this regard, thermal annealing offers a facile routine to prepare samples with different ligament sizes. Therefore, in addition to

as-prepared samples, np Au specimens were annealed in air at 300 °C for 5 min, 10 min and 20 min prior to testing.

3.3 Sample characterization

3.3.1 Imaging, elemental composition and structural analysis

High resolution scanning electron microscopy[3] (SEM) was used to characterize the sample's morphology and elemental composition. From secondary electron images, typically obtained by an in-lens detector, ligament sizes, i.e. the diameter of connecting elements between nodes, were derived by measurement of more than 50 ligaments per sample. All measurements on nanoporous metals used micrographs obtained from the sample's cross sections, since ligament structures from the outer few µm commonly deviate from the internal morphology. Sample cross sections were readily prepared by cleaving the nanoporous samples using a scalpel. Mean chemical compositions at sample center, edge and in between were measured by SEM using energy-dispersive X-ray spectroscopy (EDS). In addition, electron backscatter diffraction (EBSD) was employed to analyze grain size and orientation of the $Cu_{20}Ni_{10}Mn_{70}$ master alloy.

A detailed structural analysis of np CuNi was conducted using scanning transmission electron microscopy (FEI Talos F200X) (TEM)[4]. Electron-transparent slices of polymer-embedded np CuNi with a thickness of 70 nm were cut by using an ultramicrotome (Leica EM UC7). High resolution recording enabled crystal orientation analysis through fast Fourier transformation of the image panels. Local elemental distributions of np CuNi were measured using EDS mapping. Furthermore, TEM was used to determine elemental distributions in the heat treated $Cu_{20}Ni_{10}Mn_{70}$ master alloy. For these samples, electron-transparent slices were obtained by focused ion beam milling.

Phase identification of np CuNi and its precursor alloy was based on X-ray diffraction analysis (Bruker D8 Advance) with a Cu K-α radiation source. The measurement used crushed pieces and sample rotation for the nanoporous samples and the massive master alloy, respectively. Misadjustment in height was corrected for by a Nelson-Riley scheme.

3.3.2 Voltammetric surface area measurement

Electrochemical surface reaction currents are measured as extensive quantities that have to be referred to the surface area, A. For complex geometrical structures, and in particular for small-scale materials, determination of A appears as a non-trivial problem.

Formation of oxygen monolayers on certain metal surfaces, for instance on gold and platinum, can be capitalized to estimate A using voltammetric measurement techniques. This principle is based on the assumption that oxygen is adsorbed in a one-to-one correspondence with the surface atoms [225]. This means that the number of adsorbed oxygen species is equal to the number of surface atoms. By measurement of the charge, Q_O, transferred as a result of oxygen electrosorption the surface area can be estimated as [225]

$$A = \frac{Q_O}{q_{ref}}, \tag{3.2}$$

[3] Zeiss Supra 55 VP, Leo Gemini 1530 and FEI Helios NanoLab G3

[4] TEM investigations were conducted in collaboration with Tobias Krekeler.

where q_{ref} represents the reference charge density that takes a value of $q_{\mathrm{ref}} = 390 \pm 10\,\mu\mathrm{C/m^2}$ for gold surfaces [225].

With the above concept, the surface area of nanoporous gold was determined from cyclic voltammetry. Faradaic reaction contributions were evaluated from slow-scan voltammograms ($50\,\mu\mathrm{V\,s^{-1}}$) and subtracted before evaluation of the transferred electric charge, Q, by current integration, $I\mathrm{d}t$, to

$$Q = \int I\mathrm{d}t. \tag{3.3}$$

The integration constants are obtained through consideration of the known values at the potential of zero charge, E_{pzc}. In this work, E_{pzc} for gold surfaces in perchloric acid was used. Here, Q takes a value of 0 at $E_{\mathrm{pzc}} \approx 0.4\,\mathrm{V}$ vs. SHE [226]. Following the publication of this work's data in Reference [165], recent measurements on np Au in 1 M $HClO_4$, suggest a value of $E_{\mathrm{pzc}} = 0.77 \pm 0.19\,\mathrm{V}$ [20]. However, neither the determination of A nor the estimated variation in γ (see next subsection) are quantitatively affected by this observation. This is due to the essential invariance of Q during potential variation in the capacitive charging regime, as demonstrated in Section 4.1.3 of the next chapter.

3.3.3 Electrochemical modulation of the surface tension

Electrode polarization offers reversible control of the capillary forces, as described in Section 2.2.2. An estimate of the surface tension, γ, of as-dealloyed nanoporous gold was provided by cyclic voltammetry in 1 M $HClO_4$. Using Lippmann's equation (Equation 2.6), γ can be estimated at a given electrode potential, E, as

$$\gamma(E) = \gamma_{\mathrm{pzc}} - \int_{E_{\mathrm{pzc}}}^{E} q(\tilde{E})\mathrm{d}\tilde{E}. \tag{3.4}$$

Here, γ_{pzc} denotes the surface tension at the potential of zero charge ($E_{\mathrm{pzc}} \approx 0.4\,\mathrm{V}$) and q represents the charge density, i.e. the charge per surface area $q = Q/A$. Literature data on gold surfaces yield an average value of $\gamma_{\mathrm{pzc}} \approx 1.4\,\mathrm{J/m^2}$ [194].

3.3.4 Mechanical characterization using digital image correlation

Nanoporous metals exhibit significant plasticity in compression but they fail in a brittle manner during tensile loading. This fact impedes the straightforward exploration of the tension–compression asymmetry. Therefore, the mechanical characterization in this thesis is focused on a detailed directional analysis of elastic and plastic deformation during compressive loading.

Uniaxial compression tests were performed on all types of nanoporous metals – np Au, np Cu, np Ni and np CuNi – using a universal testing machine (Zwick 1474) equipped with a DIC system as shown in Figure 3.7 (a). Full field measurements were conducted at a constant engineering strain rate of $10^{-4}\,\mathrm{s^{-1}}$ with a pre-load of 1 N and at ambient conditions. Moreover, compression experiments on np Au were also performed in electrolytic environment whilst applying an electrical potential. These testing parameters are essentially similar to those of tests in air and particularities of the electrochemical setup are described in Section 3.3.5.

Mechanical behavior was characterized under continuous and load/unload compression up to an engineering strain of around 40 %. Testing protocols were programmed through the machine control software testXpert II (Zwick, Version 3.2). Load/unload protocols

use sequential un- and reload segments while progressively increasing the compressive deformation as depicted in Figure 3.8 (a). Molecular dynamics simulations observe immediate yielding upon compressive loading of np Au [122]. For this reason, only unloading regimes during load/unload tests (highlighted in red) were used to evaluate elastic properties as opposed to conventional evaluation during linear elastic loading.

In case of np Au, the analysis was focused on the transverse mechanical coupling behavior. The material parameter that links deformation in loading direction to the resulting perpendicular dilation is the Poisson ratio, ν. During uniaxial deformation ν can be calculated from true strain increments in loading direction, $\delta\varepsilon_{\parallel}$, and perpendicular to it $\delta\varepsilon_{\perp}$:

$$\nu = -\frac{\delta\varepsilon_{\perp}}{\delta\varepsilon_{\parallel}}. \tag{3.5}$$

With this approach, plastic deformation[5] during continuous compression testing yielded the plastic Poisson ratio, ν_{P}. The elastic Poisson ratio, ν_{E}, was obtained from separate load/unload compression tests as illustrated in Figure 3.8 (b). Note that the strongly deviating values at the reversal point of the loading direction are artifacts that are excluded from the analysis.

Differentiation between *elastic* and *plastic* Poisson ratio may be confusing, as Poisson's ratio of massive materials usually describes the transverse mechanical coupling during *elastic* deformation. As traditional, massive engineering materials typically exhibit volume conservation during plastic deformation – and thus $\nu_{\mathrm{P}} = 0.5$ – introduction of a plastic Poisson ratio may appear trivial. However, in porous solids differentiation between ν_{P} and ν_{E} is essential, since their compressibility is not limited to elastic deformation but also occurs after yielding e.g. in the form of densification.

Specifications of the digital image correlation analysis

A 12 bit VC-Phantom M110 CCD-camera with an image resolution of 1280×800 pixel was used to record the deformation experiments at an image rate ranging from 0.2 to 0.5 Hz. The system was equipped with a 35 mm F/2.0 objective combined with an adjustable zoom lens system with a maximum magnification factor of 12. This objective setup yields a resolution of up to 1 µm while maintaining a large object-to-pinhole distance, $z \approx 38$ cm, as described in Section 2.4. An approximation of the largest possible error due to out-of-plane motion can be made via Equation 2.13. As demonstrated in more detail in the next chapter, plastic Poisson ratios – and with that out-of-plane deformation Δz – exhibit maximum values for annealed np Au at large compressive deformation. For these samples, maximum Δz values are measured as 200 µm. From this, absolute normal strain errors ensue to values of $\varepsilon^{\mathrm{abs}} \leq 0.05\,\%$. If related to the measured normal strains, $\delta\varepsilon_{\parallel}$ and $\delta\varepsilon_{\perp}$, relative errors, $\varepsilon^{\mathrm{rel}} = \varepsilon^{\mathrm{abs}}/\varepsilon$, take values of around 0.1 % and 0.5 %[6] for deformation in loading direction and perpendicular to it, respectively.

Astigmatism was minimized by perpendicular alignment of the objective's optical axis towards the sample surface. Specular reflections were avoided using indirect lighting conditions as shown in Figure 3.9 (a). Semi-transparent paper tissues were illuminated

[5] For conciseness the term *plastic deformation* is used in this work instead of elastic–plastic deformation.

[6] Worst case out-of-plane error estimation for cuboid bodies. For cylindrical sample geometries, the maximum transverse strain error depends on the placement of the virtual strain gage markers with respect to the longitudinal axis. If the strain gage markers approach the sample's edge out-of-plane motion and with that $\varepsilon_{\mathrm{abs}}$ converges to 0.

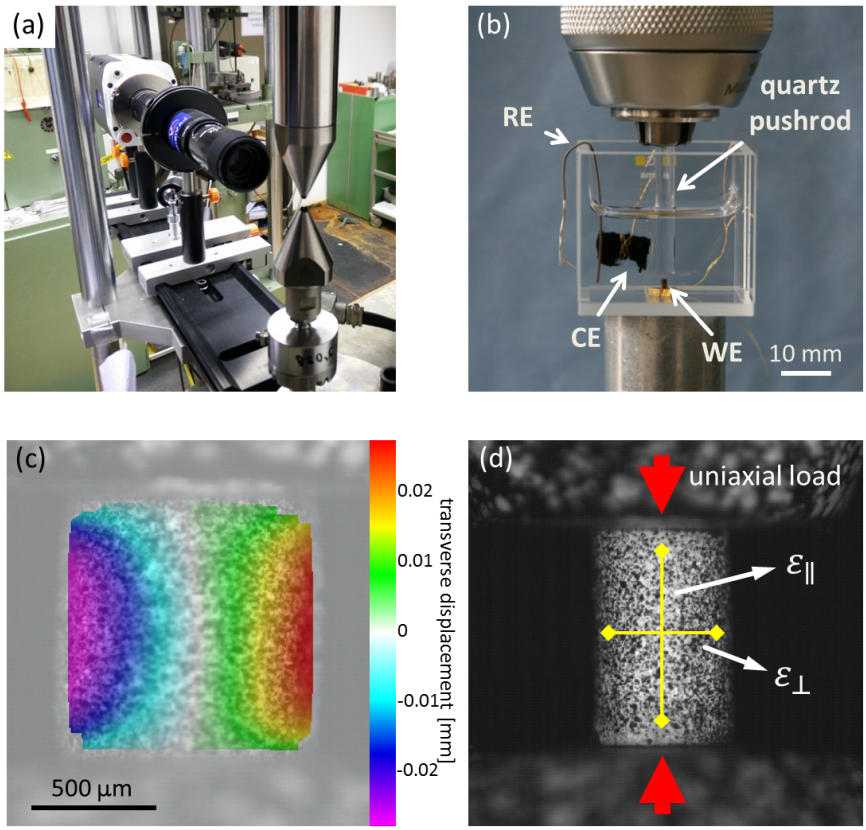

Figure 3.7: Deformation experiments in different environments analyzed by digital image correlation (DIC). (a) Compression test setup in air. Digital camera with objective and steel punches are depicted. (b) Extended setup mounted in a conventional testing rig for electro-chemo-mechanical tests in electrolyte. The glass cuvette with optical windows enables imaging during the deformation. Designation of electrodes: sample (working electrode, WE), counter- (CE) and reference (RE) electrode. (c) Example of a transverse displacement map of annealed nanoporous gold at 20 % compressive engineering strain as calculated by DIC. (d) Depiction of the placement of virtual strain gages (yellow lines) in a gray scale image with a spray-painted speckle pattern. Strains are measured in loading direction, $\varepsilon_{\parallel}$, and perpendicular to it, $\varepsilon_{\perp}$. [164, 165]

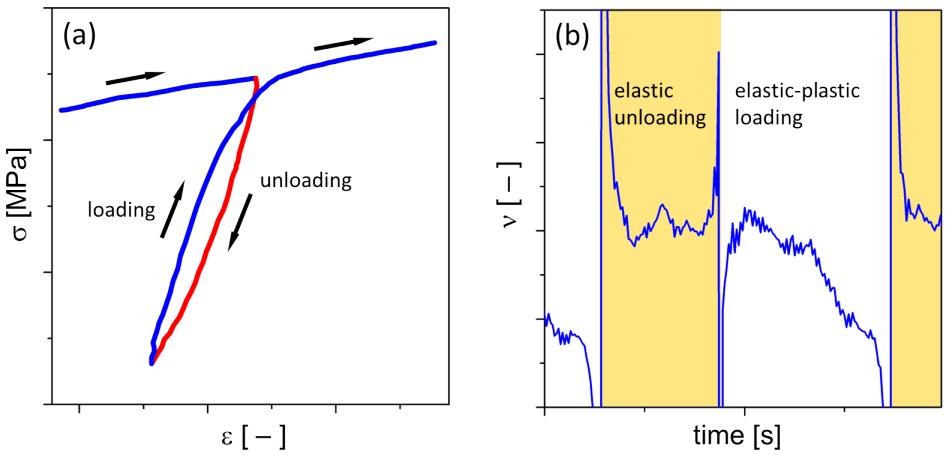

Figure 3.8: Determination of the elastic properties using load/unload segments during compressive deformation. (a) Depiction shows a single stress-strain segment as obtained from cyclic loading of nanoporous gold. The elastic unloading regime is highlighted in red, arrows indicate chronological deformation progress. (b) Time-resolved evolution of the Poisson ratio during cyclic loading. The elastic Poisson ratio, ν_E, is measured in the regime of elastic unloading (yellow shaded area).

to create diffuse lighting around the sample. A reflective screen was placed across from the light source to achieve uniform illumination of the tissues. In the course of this work, primer paint applied to the samples lateral surface has proven to be a good method to avoid specular reflections, too, even when directly illuminated through a ring light as shown in Figure 3.9 (b). This can be attributed to the very rough surface created by the undercoat paint. By using an airbrush system, a black and white speckle pattern was created that dried within a few seconds. With this method, significant improvement of contrast was achieved during imaging that increased accuracy and robustness of the image correlation analysis (see Figure 3.7 (d)). The airbrush system produces speckles with sizes ranging from approximately 18 to 56 µm. Scanning electron microscopy validated that no paint entered the sample interior. For this thesis, some experiments presented in Reference [164] have been repeated on samples with applied speckle patterns to improve the accuracy of the measured results. Still, for in-electrolyte tests application of speckle patterns was forgone to avoid potential influences on the electrochemical analysis.

Image correlation was performed using the software DaVis (LaVision, Versions 8.20 and 8.31). The program uses bilinear interpolation schemes and first order affine shape functions to calculate pixel displacements as explained in Section 2.4. Subset and step size were chosen as 19 – 40 pixels and 6 – 10 pixels, respectively. The individual pixel size ranged from 3 to 5 µm. A detailed report table of the DIC evaluation parameters can be found in Table 3.1.

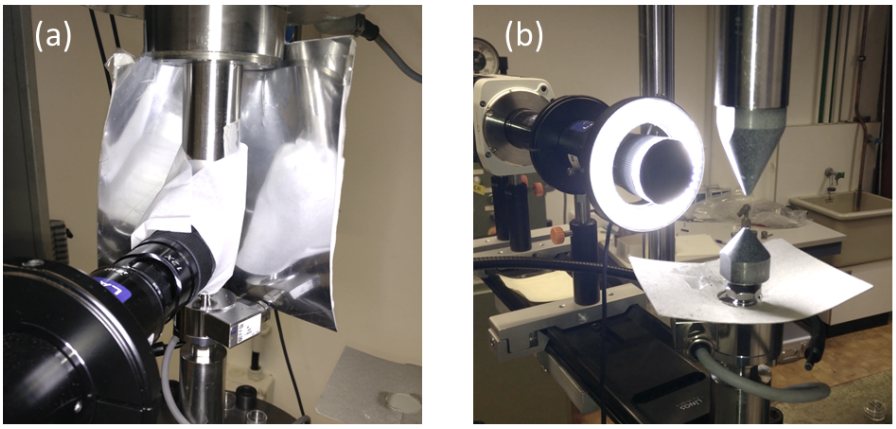

Figure 3.9: Photographs of different lighting conditions used to avoid specular reflections during image recording. (a) Diffuse lighting produced by illumination of semi-transparent paper tissues. (b) Illumination via ring light in combination with spray painted base coat (as shown in Fig. 3.7 (d)).

Table 3.1: Summary of image acquisition and correlation parameters used during the strain evaluation of uniaxial compression tests in air and electrolyte.

Parameter	Value
Image acquisition rate	0.2 – 0.5 Hz
Exposure time	4000 – 8000 µs
Camera resolution	1280 × 800 pixel
Pinhole-to-object distance	38 – 42 cm
Objective resolution	1 µm
Evaluated image section	130000 – 160000 pixels
Pixel-to-µm conversion	3 – 5 µm/pixel
Subset size	19 – 40 pixels
Step size	6 – 10 pixels

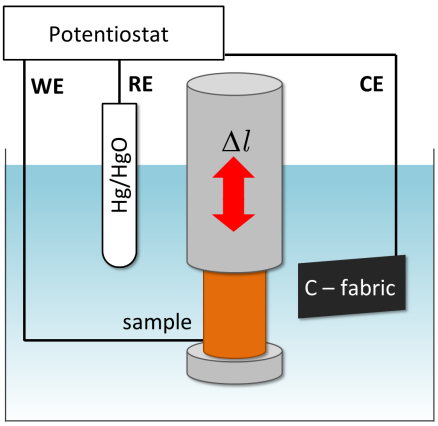

Figure 3.10: Schematic depiction of the measurement setup used to characterize the actuation response of nanoporous base metals in 1 M NaOH electrolyte. A potentiostat controls the applied electrical potential; sample, carbon cloth and Hg/HgO are connected as working (WE), counter (CE) and reference electrode (RE), respectively. Deformation in axial direction, Δl, is measured by a vertical dilatometer.

3.3.5 Compression testing in electrolytic environment

To experimentally verify the concept of a surface-induced tension–compression asymmetry, the previously described testing rig was modified to enable electrochemical measurements during mechanical loading. As shown in Figure 3.7 (b), the conical steel punches used in conventional tests were replaced. On the lower side, a glass cell was glued to a flat punch. On the other side, a quartz pushrod was clamped into a drill chuck. Both, continuous and load/unload compression experiments were conducted in 1 M $HClO_4$ while np Au samples – as-dealloyed and annealed for 5 min at 300 °C – served as the working electrode (WE), carbon tissue as counter electrode (CE) and homemade Ag/AgCl as reference electrode (RE). During continuous compression tests the applied electrical potential was switched in situ, whereas load/unload tests were conducted at different, constant potential values. Measurement of a set of 20 samples provided reproducibility of trends and values of ν_E and ν_P.

3.3.6 Actuation measurement

The functionalization potential of np CuNi was explored by characterization of the actuation response during electrochemical modulation in alkaline solution. Figure 3.10 schematically illustrates the test setup. The electrochemical setup resembles the in situ testing described in the previous section with one exception: owing to the alkaline environment commercial Hg/HgO is chosen as the reference electrode.

As-dealloyed samples of np CuNi, np Cu and np Ni were analyzed in 1 M NaOH by cyclic voltammetry with a scan rate of 1 mV s^{-1}. The onsets of gaseous hydrogen and oxygen evolution imposed upper and lower limits of the investigated potential range, respectively. A vertical dilatometer (Linseis L75) was used to measure the axial sample deformation.

4 Signature of surface-induced tension–compression asymmetry

4.1 Results

4.1.1 Microstructure of nanoporous gold

Microstructural analysis of nanoporous gold (np Au) finds bicontinuous, crack-free networks composed of smooth ligaments as depicted in Figure 4.1. Scanning electron microscopy identified the mean ligament sizes, L, as 38 ± 9 nm for as-dealloyed np Au (a) and 74 ± 18 nm (b), 121 ± 31 nm (c) and 174 ± 40 nm (d) for the samples annealed in air at 300 °C for 5 min, 10 min and 20 min, respectively. Ligament sizes are plotted with respect to the annealing time in graph (f). It can be seen, that thermal annealing proves a suitable technique for controlled tuning of the ligament size and, by extension, the surface area to volume ratio. For the sake of conciseness, ligament sizes of np Au samples are further denoted as 40 nm, 70 nm, 120 nm and 170 nm in the course of this work. While it may appear tempting from images (a-d) to qualitatively suggest that the structure's morphology is maintained during coarsening, the present analysis techniques are not sufficient to draw this conclusion. In this context, direct tomographic measurements on np Au [154, 155] synthesized in a process similar to this work find essentially self-similar coarsening behavior. Yet, self-similarity during coarsening of np Au is still disputed a topic, as detailed in Section 1.4 of the introductory chapter.

An overview micrograph of a representative sample cross section of np Au is given in (e). From the smooth fractured surface – the right notch in (e) originates from the indent of the scalpel blade – it can be seen that cracking occurs in a transgranular manner. Identical cracking behavior is observed by Reference [63] and – in more detail – by *Sun et al.* [19] in their study on fracture mechanisms of np Au.

Through measurements of specimen mass and of outer dimensions, by means of a measurement microscope, sample densities were calculated as $4.9 \pm 0.3\,\mathrm{g/cm^3}$, $5.3 \pm 0.4\,\mathrm{g/cm^3}$, $5.4 \pm 0.1\,\mathrm{g/cm^3}$ and $5.5 \pm 0.1\,\mathrm{g/cm^3}$, for samples with $L = 40$ nm, 70 nm, 120 nm and 170 nm, respectively. Corresponding solid fractions ensue to 0.25 ± 0.2, 0.27 ± 0.3, 0.28 ± 0.1 and 0.28 ± 0.1, respectively. Energy dispersive X-ray spectroscopy finds a residual Ag content of less than 1 at.%.

4.1.2 Deformation behavior during compression in air

In this work, experimental testing under compressive load is the primary investigation technique to explore the mechanical properties of nanoporous metals. Before examining the transverse coupling behavior of np Au, its stress–strain response is inspected in the following.

Figure 4.2 shows representative data for np Au with ligament sizes of around 40 nm, 70 nm, 120 nm and 170 nm. The graph depicts engineering stress, σ_{eng}, plotted versus engineering strain in loading direction, $\varepsilon_{\mathrm{eng}}$. Common for all samples, regardless of the

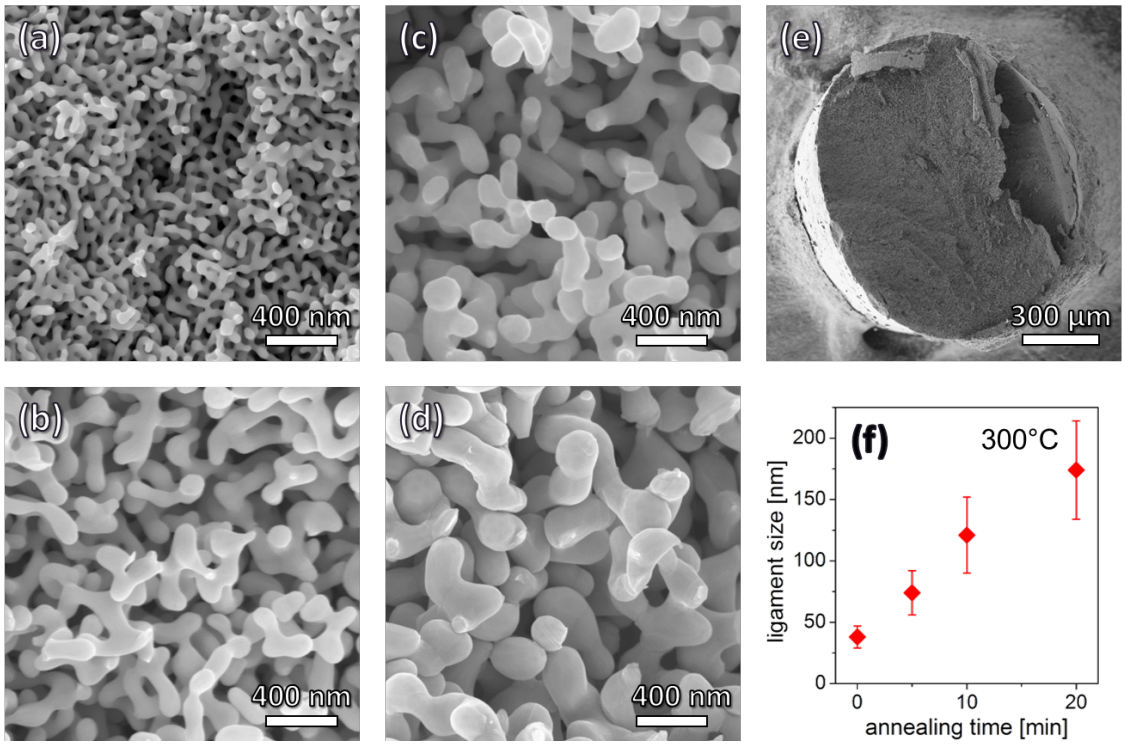

Figure 4.1: Microstructure of nanoporous gold (np Au). Images show scanning electron micrographs of as-prepared (a) and annealed np Au (b-d) with ligament sizes of around 40 nm, 70 nm, 120 nm and 170 nm, respectively. (e) Representative depiction of the cross section of np Au; here for $L = 70$ nm. Samples were intentionally cleaved using a scalpel. (f) Ligament size evolution of np Au annealed at 300 °C plotted versus the annealing time. Error bars represent standard deviations.

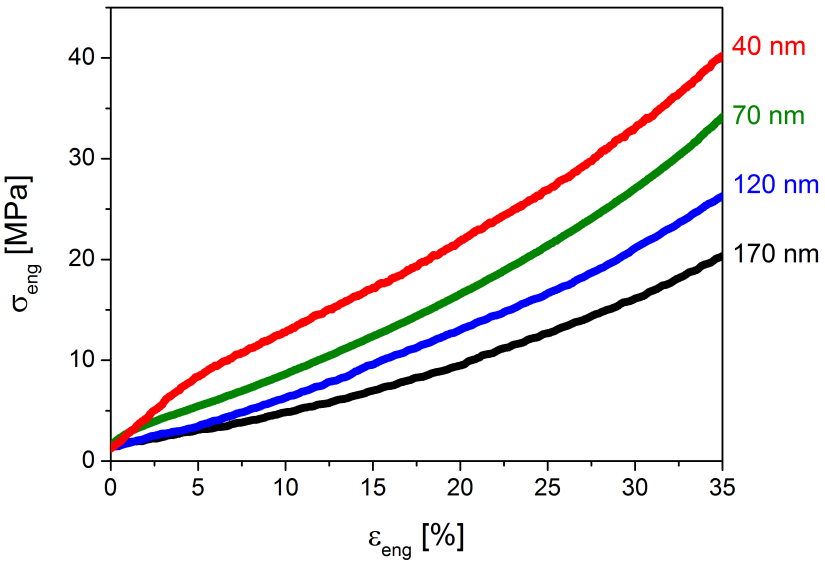

Figure 4.2: Continuous loading compression tests of macroscopic nanoporous gold with varying ligament size; engineering stress, σ_{eng}, plotted versus engineering strain in loading direction, $\varepsilon_{\mathrm{eng}}$. All samples show considerable deformability and significant hardening. Samples with smaller ligament size, L, exhibit higher stresses.

ligament size, is the very high deformability. This is a prerequisite for meaningful investigation of the plastic properties. Also, significant hardening is observed during plastic flow for all samples. During compression, hardening is dominated by densification of the porous bodies. The severe contribution of densification on the overall mechanical response is illustrated by the evolution of Young's modulus data with proceeding compressive deformation in Figure 4.3. Conventional hardening by mere dislocation interaction leaves the Young's modulus essentially unaltered. Here, values can increase by a factor of more than 30 from the onset of deformation to a strain of around 45 %. This can be attributed to the densification of the network structure.

Distinct differences in the mechanical behavior of the variously heat treated samples are found for the strength. With increasing ligament size, a reduction in stress is observed for all samples of Figure 4.2. In addition, for $L = 40\,\mathrm{nm}$ a linear progression is observed at the beginning of deformation that – in massive materials – would be generally attributed to purely elastic deformation. However, in np Au yielding of individual ligaments occurs immediately after loading [122]. Thus, the linear progression of as-dealloyed np Au at initial sample deformation may be viewed as an elastically dominated regime rather than pure elastic compression. Conventional, uniform plastic deformation is considered to occur after transition from linear progression to the above-mentioned hardening-dominated flow behavior.

The measurement scheme of Poisson's ratio has been introduced in Section 3.3.4 in the previous chapter. A requirement for this measurement scheme is a homogeneous strain distribution during mechanical testing, devoid of localized stress concentrations. The validity of the measurements relies on the assumption that the virtual strain gauges are representative of the material's response to the imposed loading. It is therefore significant

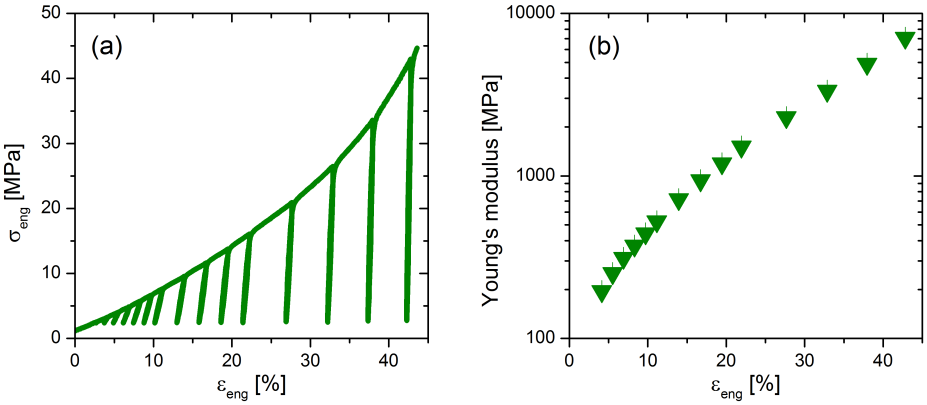

Figure 4.3: Exemplary load–unload compression test of nanoporous gold with a ligament size of 70 nm. (a) Engineering stress, σ_{eng}, plotted vs. engineering strain, $\varepsilon_{\mathrm{eng}}$. (b) Young's modulus vs. $\varepsilon_{\mathrm{eng}}$. Significant hardening and stiffening via densification is observed.

that full-field deformation maps of nanoporous gold find essentially uniform displacement and strain distributions in the loading direction (Figure 4.4 (a, c)) and perpendicular to it (b, d). This observation is found in all investigated ligament sizes and exemplified in Figure 4.4 for np Au with $L = 70\,\mathrm{nm}$. Moreover, homogeneously distributed shearing is found throughout the entire deformation for all investigated np Au samples, as well, see Figure 4.4 (e).

Yet, at high strains ($\geq 20\,\%$) friction at the contact area between steel punch and np Au sample causes slight barreling of the compressed bodies. Signatures of the ensuing bulges can be identified from small gradients in the distribution of the transverse displacement, for instance in Figure 4.4 (b). Since the evaluation of Poisson's ratios relies on the transverse strain measured in the sample center, barreling leads to overestimation of values at high compressive deformation. The overall impact of barreling on the data appears to be small, as no systematic variation in transverse straining is observed from mapped strain distributions (Figure 4.4 (d)).

An evaluation of the transverse mechanical coupling behavior during plastic flow is presented in Figure 4.5. The graph shows data for the plastic Poisson ratio, ν_{P}, of np Au with different L plotted versus $\varepsilon_{\mathrm{eng}}$. Contrary to previous assumptions [124–127], all samples exhibit nonzero ν_{P} values throughout the entire deformation. A trend towards increasing values of ν_{P} with proceeding deformation is observed that coincides with advancing densification. Remarkably, substantially lesser ν_{P} values are measured for np Au with $L = 40\,\mathrm{nm}$ (initially $\nu_{\mathrm{P}} \approx 0.08$) compared to the coarsened samples (≈ 0.17). Note, that at $L \geq 70\,\mathrm{nm}$ no systematic size dependence of ν_{P} values can be identified.

Figure 4.6 shows the elastic Poisson ratio, ν_{E}, as obtained from unloading regimes during cyclic compression testing of np Au. The graph depicts average values for ν_{E} in the individual unloading segments of a single sample. Error bars represent 95 % confidence intervals within each segment. The results are in striking contrast to the measurements obtained for the plastic Poisson ratio, since ν_{E} is found essentially invariant of the ligament size. At early deformation stages, ν_{E} of np Au exhibits a value of 0.20 ± 0.02 that increases, similar to ν_{P}, with proceeding deformation. This is significantly less than what is typically found for conventional metallic foams, for which $\nu_{\mathrm{E}} = 0.31 - 0.34$ [218].

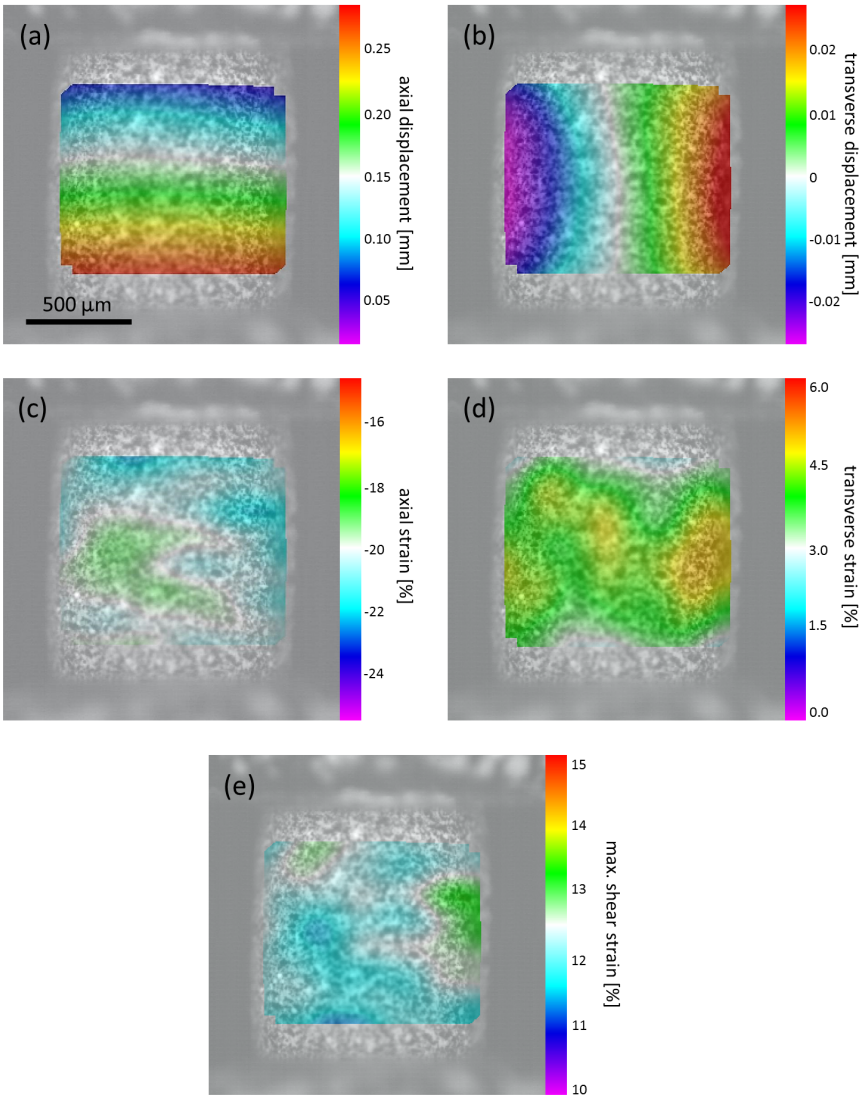

Figure 4.4: Exemplary deformation maps of nanoporous gold with a ligament size of 70 nm obtained during uniaxial compression testing. Images were taken at an average engineering strain in loading direction of 20 %. Essentially homogeneous deformation and strain distribution is observed in axial (a, c) and transverse direction (b, d), as well as for shearing (e). At high strains barreling occurs at the contact area between sample and steel punch. Note, in contrast to macroporous foams no localized deformation occurs.

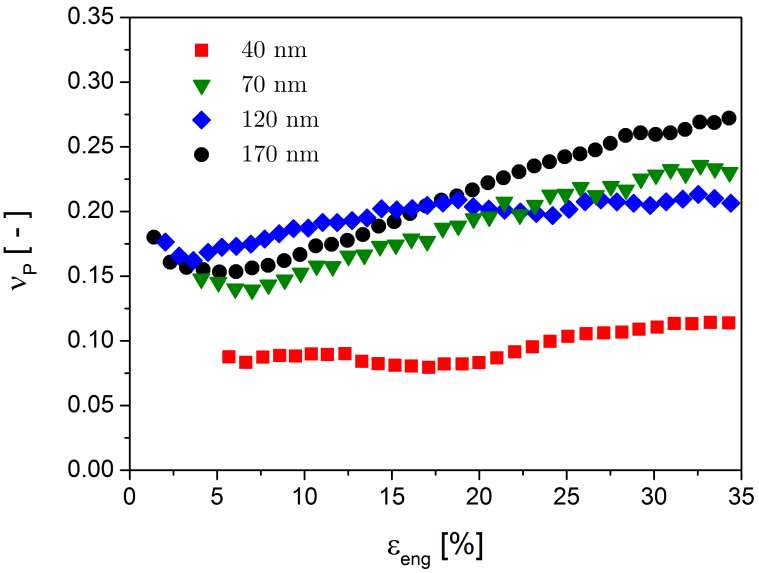

Figure 4.5: Plastic transverse coupling behavior measured during continuous compressive deformation of nanoporous gold (np Au) samples with varying ligament sizes, L. Plastic Poisson ratio values, ν_P, are determined after yielding and plotted versus the engineering strain in loading direction, ε_{eng}. While coarsened np Au exhibits essentially similar ν_P, significantly lower values are measured for samples with $L = 40\,\text{nm}$.

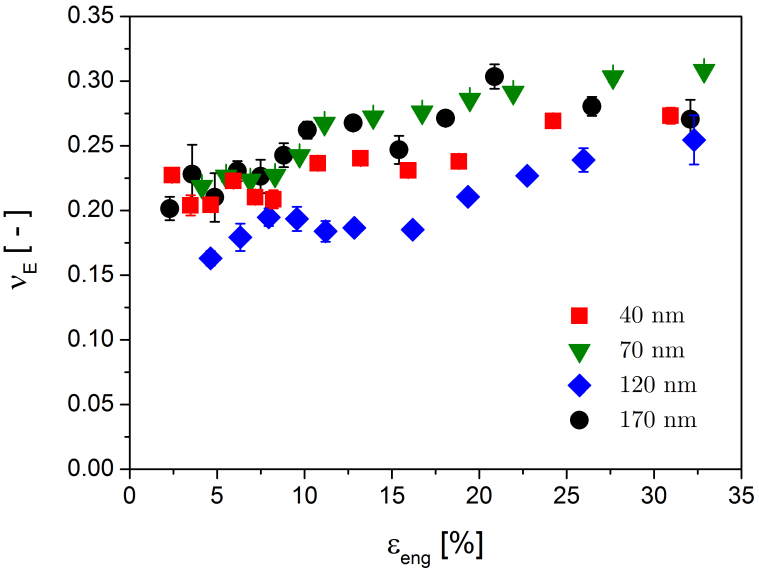

Figure 4.6: Experimental results for the elastic Poisson ratio, ν_E, of nanoporous gold with different ligament sizes, L. Data is obtained from elastic unloading regimes during cyclic compression testing. Values for ν_E are plotted with respect to the engineering strain in loading direction, ε_{eng}; error bars represent 95 % confidence intervals. No systematic distinction between different L is observed.

4.1.3 Electrochemical characterization

The influence of electrode polarization on the surface tension, γ, of np Au in aqueous 1 M $HClO_4$ was quantified by electrochemical analysis. Figure 4.7 shows voltammograms of np Au with $L = 40\,\text{nm}$ at scan rates of $v = 1, 5$ and $10\,\text{mV}\,\text{s}^{-1}$, the arrows indicate the scan direction. For the example in Figure 4.7, a net charge transfer during oxidation of $0.379 \pm 0.015\,\text{C}$ was measured. From Equation 3.2 in Section 3.3.2 the sample's total surface area was calculated as $A = 970 \pm 40\,\text{cm}^2$.

In Figure 4.7 (a), the graph depicts voltammetric scans. Current densities, i.e. current per surface area, $j = I/A$, are in good agreement with literature data for planar gold surfaces [214, 215]. All measurements are devoid of Ag-peaks. This emphasizes that the investigated samples are free of residual silver. The measurements also show a variation of the position of the oxidation–reduction peaks with the applied potential scan rate, v. An increasing peak separation is observed for faster v. This suggests that with increasing v the pseudocapacitive reaction drifts further away from a state of equilibrium.

Panel (b) of Figure 4.7 shows the specific charge density, that is the charge transferred per surface area, $q = Q/A$. Note, Q was calculated from current integration as detailed in Section 3.3.2 of the previous chapter. Transfer of charge is primarily observed in the regime of oxygen electrosorption.

Figure 4.7 (c) displays the estimated variation in surface tension, γ. The data was obtained by integrating Equation 3.4 in Section 3.3.3 separately for positive- and negative going branches of the cyclic voltammograms, as indicated by arrows. During capacitive charging, γ exhibits an approximately quadratic variation around the potential of zero charge, E_{pzc}, see Section 2.2.2. At the scale of the figure, the quadratic variation in γ around E_{pzc} is not resolved. While γ remains approximately constant during capacitive charging, a considerable reduction in γ values is measured during electrosorption of oxygen species. For this reason, electrical potential values of $E = 0.8\,\text{V}$ and $1.5\,\text{V}$ are chosen for in situ mechanical testing which correspond to a clean, adsorbate-free surface state and the formation of a monolayer of oxygen species, respectively.

As a consequence of the distinct hysteresis in the voltammograms of np Au, substantially different values are provided by positive- and negative scans for $\gamma(E)$. Strictly speaking, Equation 2.6 is only valid in a state of equilibrium. Therefore, γ values obtained from positive and negative going branches of the CV are considered to impose upper and lower bounds for the true value of γ.

The values derived from Lippmann's equation for the surface tension at $E = 1.5\,\text{V}$, $\gamma_{1.5\,\text{V}}$, – that is one of the two potentials selected in this work's mechanical tests – are plotted versus the scan rate in Figure 4.8. It can be seen that these values slowly converge. The mean values remain essentially constant at around $0.4\,\text{J}/\text{m}^2$, irrespective of the scan rate. Therefore, $0.4\,\text{J}/\text{m}^2$ is taken as a best guess for the true value of $\gamma_{1.5\,\text{V}}$. Compared to a clean, adsorbate-free surface state ($\gamma_{0.8\,\text{V}} \approx 1.4\,\text{J}/\text{m}^2$), the results indicate that the surface tension is reduced to roughly a third during oxygen electrosorption.

4.1.4 In situ mechanical testing

Elastic response

In-electrolyte experiments used load/unload compression tests at different constant electrical potentials, E, to determine the elastic Poisson ratio of np Au with $L = 40\,\text{nm}$ and 70 nm, see Figure 4.9. Part (a) of the figure shows the stress–strain behavior at

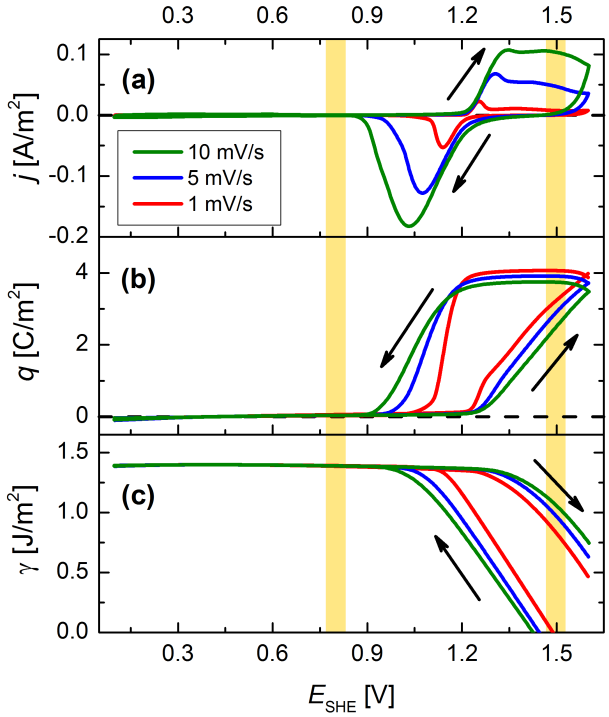

Figure 4.7: Electrochemical characterization of nanoporous gold with a ligament size of 40 nm measured in 1 M $HClO_4$ electrolyte. (a) Cyclic voltammograms at scan rates of 1, 5 and 10 mV s^{-1}; electrode current density, j, plotted versus applied electrical potential, E_{SHE}. Arrows indicate scan direction. (b) Charge density, q, determined from cyclic voltammograms via integration of $j(E)$ after subtraction of the Faraday current. (c) Variation of the surface tension, γ, estimated from Lippmann's equation. Positive and negative going branches of the voltammogram are integrated separately, as indicated by arrows. Potential values selected for in situ mechanical testing are highlighted by yellow bars. [165]

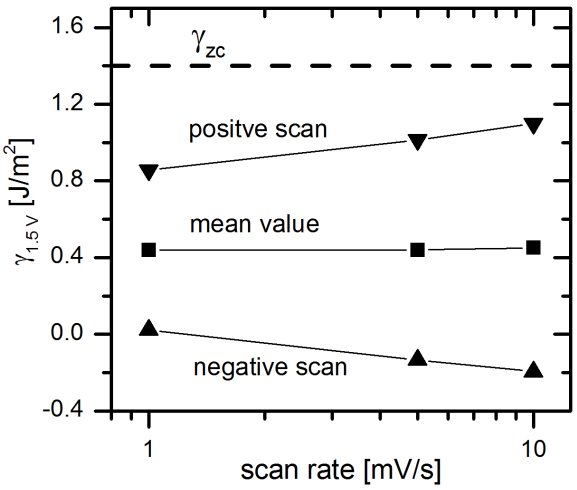

Figure 4.8: Estimated values for the surface tension of nanoporous gold during electrosorption, $\gamma_{1.5\,V}$, at an electrode potential of 1.5 V plotted vs. the potential scan rate. Data is obtained from positive- and negative-going branches of the cyclic voltammograms depicted in Figure 4.7 (c). Mean values appear approximately constant and are found considerably lower than the surface tension at the potential of zero charge, γ_{zc}. [165]

the example of a sample with $L = 40\,\text{nm}$ and $E = 0.8\,\text{V}$. The graph illustrates that despite challenging lighting conditions and without the applied speckle pattern, the measurements in electrolyte are in good agreement with trends and values obtained with conventional compression tests in air.

Values of ν_E are given in Figure 4.9 (b) for samples with adsorbate-free ($E = 0.8\,\text{V}$, full symbols) and oxygen-covered (1.5 V, open symbols) surfaces; error bars represent confidence intervals with 95 % confidence level. The data reveals that E has no significant influence on ν_E. Moreover, initial values of $\nu_E = 0.20 \pm 0.02$ agree well with data obtained for measurements in air, see Figure 4.6. In addition, values of ν_E also appear to be invariant with respect to L. Note, samples with $L = 40\,\text{nm}$ at $E = 1.5\,\text{V}$ failed at low strain. This is due to the electrosorption of oxygen species which significantly decrease the deformability of np Au with small ligament size, see for instance Reference [16].

Electrochemically modulated plastic flow

In situ experiments exploring the plastic flow behavior of np Au used continuous compression tests in electrolyte. During these tests, the applied electrical potential was switched between capacitive charging and oxygen electrosorption regime. Figure 4.10 depicts results for σ_{eng} and ν_P of np Au samples with $L = 40\,\text{nm}$ (a, b) and 70 nm (c, d), all plotted versus ε_{eng}. Stress–strain graphs (top row) show that the material's strength increases substantially when the surface is modified from an adsorbate-free ($E = 0.8\,\text{V}$, light region in graph) to an oxygen covered state ($E = 1.5\,\text{V}$, yellow shaded region). This effect is fully reversible and consistent with earlier studies on np Au [16]. At low potential, the stress–strain behavior of both samples resembles values and trends obtained for np Au in air. This finding can be attributed to the similar surface states of dry np Au and samples

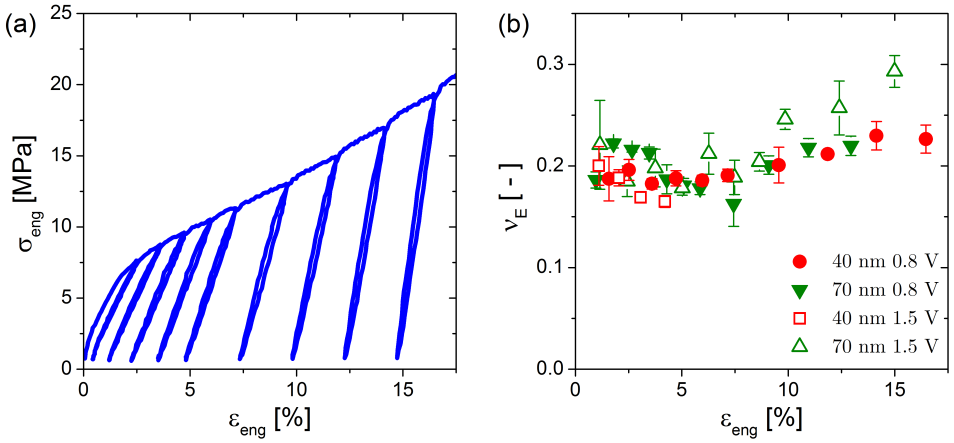

Figure 4.9: In-electrolyte load/unload compression tests of nanoporous gold with a ligament size of $L = 40\,\text{nm}$ and 70 nm. Experiments were conducted at constant electrical potential values of $E = 0.8\,\text{V}$ and $1.5\,\text{V}$ vs. the standard hydrogen electrode in 1 M $HClO_4$. (a) Stress–strain graph of a sample with $L = 40\,\text{nm}$ and $E = 0.8\,\text{V}$. (b) Elastic Poisson ratio, ν_E, as measured from unload segments vs. engineering strain in loading direction, ε_eng. Error bars represent 95 % confidence intervals. [165]

immersed in electrolyte at low potential – a clean Au surface without adsorbates. The influence of wetting on the mechanical properties appears to be negligibly small. This observation is supported by a comparable study on np Au [16].

Measurements of ν_P (bottom row, Figure 4.10) show considerable deflections immediately after potential switching for both ligament sizes. This effect is attributed to elastic strains as a result of potential-induced variation in surface stress (see Section 2.2.2). This results in excursions of the derivatives in Equation 3.5 and cannot be linked to plastic transverse flow. Yet, within intervals of constant potential the data assumes roughly uniform values that do represent the plastic transverse coupling behavior and thus the plastic Poisson ratio ν_P. The most striking finding is that ν_P systematically jumps to higher values during adsorption of oxygen species and back to lower ones during desorption. Similar to the stress–strain behavior, electrochemical modulation of ν_P is fully reversible. A variation in ν_P of roughly 0.05 is observed for $L = 40\,\text{nm}$. This corresponds to more than 40 % of the absolute value.

The experimental data for ν_P is summarized in Figure 4.11. The depicted bars represent successive average values of ν_P during consecutive potential steps that alternate between 0.8 V and 1.5 V. The graph illustrates the reproducibility of the jumps in the plastic transverse coupling response.

4.2 Discussion

4.2.1 Deformation behavior of nanoporous gold – general remarks

Full-field measurements find uniformly distributed strains during compression testing of np Au (Figure 4.4). These findings are in distinct contrast to the localized deformation that is found in macroporous metallic foams. Here, plastic yielding is carried by a collective collapse of cell walls that leads to formation of highly compressed “crush

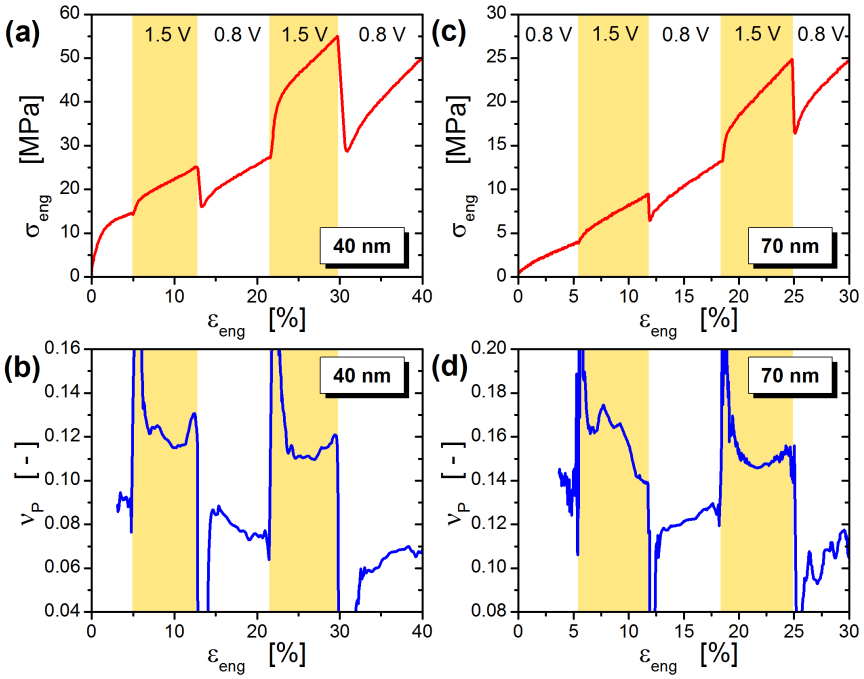

Figure 4.10: In situ compression tests of nanoporous gold with a ligament size of 40 nm (left column) and 70 nm (right column) during modulation of the applied electrical potential, E, in 1 M $HClO_4$. Engineering stress (σ_{eng}, top row) and plastic Poisson ratio (ν_P, bottom row) plotted versus axial engineering strain, ε_{eng}. E was switched between the regime of oxygen electrosorption (1.5 V vs. standard hydrogen electrode, yellow shaded regions in graph) and an adsorbate-free metal surface (0.8 V, light regions). [165]

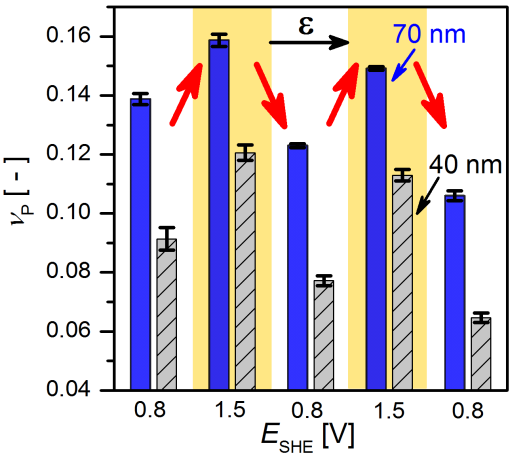

Figure 4.11: Plastic Poisson ratio, ν_P, of nanoporous gold with ligament sizes of 40 nm (gray, striped bars) and 70 nm (blue bars). The data is obtained from continuous loading compression tests in electrolytic environment during step-wise potential modulation. The bars represent average values in regimes of constant electrical potential of $E_{SHE} = 0.8$ V (light region in graph) and 1.5 V (yellow shaded region). The black arrow indicates advancing deformation, ε, while red arrows emphasize trends during potential jumps. Error bars represent 95 % confidence intervals. [165]

bands" [203, 218]. This can be ascribed to microstructural differences, for instance, the aspect ratio of the load-bearing structural elements. Cell geometries of conventional metallic foams typically exhibit very high aspect ratios with a cell wall length to thickness ratio ranging between around 10 and 15 [227]. In these materials, plastic deformation is considered to occur mainly in highly deformed "plastic hinges" localized around the nodes [129]. In contrast, np Au exhibits a distance between nodes of only roughly two to three times the ligament diameter, as estimated from electron micrographs, such as Figure 4.1 (a-d). The low aspect ratios in np Au networks prevent buckling-related failure and, with this, the sudden plastic breakdown of conventional metallic foams [129]. Furthermore, mass agglomeration in nodes of np Au promotes essentially different deformation behavior compared to metallic foams, since every part of the network structure – nodes as well as ligaments – exhibits plastic deformation (see Section 1.4). Also, essentially common glide planes between adjoining ligaments enable little obstructed dislocation motion away from initial centers of stress accumulation that promotes distribution of stresses into the surrounding.

Although no collective structural collapse is observed, it should be emphasized that localized stress concentrations still govern the initial macroscopic mechanical response of np Au. Local yielding of individual ligaments occurs immediately after loading [122] and manifests in the form of a mixed elastic–plastic deformation regime (Figure 4.2). This may be attributed to relatively broad distributions of ligament diameters, shapes and orientation (Figure 4.1 (a-d, f)) that lead to plastic flow of single, weak ligaments while neighboring elements sustain the imposed load. Since the imaging setup cannot resolve these local yielding events, it can be assumed that localized flow is indeed limited to very small volumes, i.e. less than the image correlation's resolution of around 5 µm.

4.2.2 Transverse mechanical coupling response during elastic deformation

In this work, the mechanical characterization of np Au is focused on the transverse response towards uniaxial compressive loading, as parameterized by the elastic and the plastic Poisson ratios, ν_{E} and ν_{P}. As detailed in the Section 1.4 of the introductory chapter, the uniaxial deformation of randomized network structures, such as np Au, entails contributions of both, axial tension and axial compression. In these networks, the deformation state of the individual struts depends on their orientation towards the global principal loading direction. In case of uniaxial compression, struts aligned with the loading axis are preferentially compressed whereas those oriented perpendicular tend to be stretched [160]. Therefore, the macroscopic Poisson ratios yield insights into variations in the local mechanical response of differently oriented ligaments. This enables the exploration of a possible tension–compression asymmetry on the scale of individual ligaments.

During elastic unloading, ν_{E} is found independent of the ligament size (Figure 4.6) and the applied electrical potential (Figure 4.9 (b)). To begin with, the size invariance of ν_{E} will be discussed in the following. As described in Section 1.3 of the introductory chapter, experimental studies of nanoscale objects yield no conclusive support of a size-related effect on the elastic properties. Contradictory results are reported that may simply reflect the experimental difficulties at specimen sizes below 100 nm. However, simulations find that the impact of nonlinear elastic bulk behavior and surface excess elasticity – at least for clean metal surfaces – is negligible at specimen sizes exceeding 10 nm [120–122]. From this it can be readily understood that the elastic Poisson ratio

of np Au samples remains essentially invariant during coarsening as the ligament size is well above the threshold below which size-related effects become relevant.

While the surface excess parameters may be negligible for samples with clean metal surfaces, a study of np Au with experimental conditions similar to this work finds an increase of up to 8 % in Young's modulus by electrosorption of oxygen species [18]. These findings are fully consistent with this work's observation that ν_E is independent of the surface state, because the stiffening acts symmetrically, irrespective of the deformation direction. Symmetric variation of the mechanical behavior leaves the lateral mechanical coupling unchanged.

Let us now turn away from local mechanics of individual ligaments to the macroscopic elastic response of np Au. Experiments find an average value of $\nu_E = 0.20 \pm 0.02$ for samples with a solid fraction, φ, – or relative density – between 0.25 and 0.28. Figure 4.12 summarizes this work's results and compares it to literature data on np Au. Early mechanical studies were focused on microscale specimens (black, open symbols) that were characterized by compression [62, 136], tension [19, 62] and ultrasonic testing [228]. Following the publication of this thesis' data [164], ν_E of macroscopic np Au samples has been investigated by *Bürckert et al.* [68]. Considering the very large deviations between micro- and macroscale testing typically reported for Young's modulus and yield strength data of np Au (see Section 1.4), it is astonishing that ν_E values agree well among the various studies. The importance of this finding is emphasized by *Roschning and Huber* [229], whose numerical study of np Au profits from the small dispersion of ν_E as it is chosen as the principal calibration quantity of their model. In this light, it appears appropriate to discuss the origin of the elastic Poisson ratio in the following.

The elastic Poisson ratio of massive materials is determined by the atomistic nature of its constituents. For instance, a positive correlation of ν_E with the atomic packing density has been recognized [231, 232]. In porous bodies, another key factor arises that can considerably affect the transverse elastic response: the structural morphology [232]. In case of np Au, bulk gold exhibits a comparatively high value of $\nu_E = 0.42$ [138]. It is within reason to assume that in case of severe densification ν_E of np Au will approach this value. However, with decreasing solid fraction structural characteristics gain importance. Two examples that illustrate the structure's role are conventional open-porous foams and auxetic materials.

Commercial foams with open cell walls typically exhibit uniform, but complex microstructural morphologies. Often, these microstructures resemble polyhedral geometries, such as the tetrakaidecahedron (Figure 4.13 (c)). In addition, they are composed of high aspect ratio struts and negligible mass agglomeration in the nodes [233]. Two examples of commercial Al- and Ni-foam are given in Figures 4.13 (a) and (b). In their pioneering work on cellular solids, *Gibson and Ashby* [129] introduce a cubic model structure whose dominant deformation mode is assumed to be bending of the cell walls. In combination with empirically determined scaling constants, the approach has proven outstanding prediction qualities with regard to mechanical behavior of commercial metallic [218, 234] or polymeric foams [235]. This shows that, despite its simplified cell geometry, the model captures the essential deformation mechanisms of these materials. For open-porous foams, *Gibson and Ashby* [129] conclude on constant elastic Poisson ratio values of around 0.33, irrespective of solid fraction and material. This seemingly contradicts the previous statement of $\nu_E = 0.42$ for $\varphi \to 1$. Yet, within the applicability of the Gibson-Ashby model – low-density foams with comparatively regular microstructure – experimental studies support the model predictions [129, 218, 234].

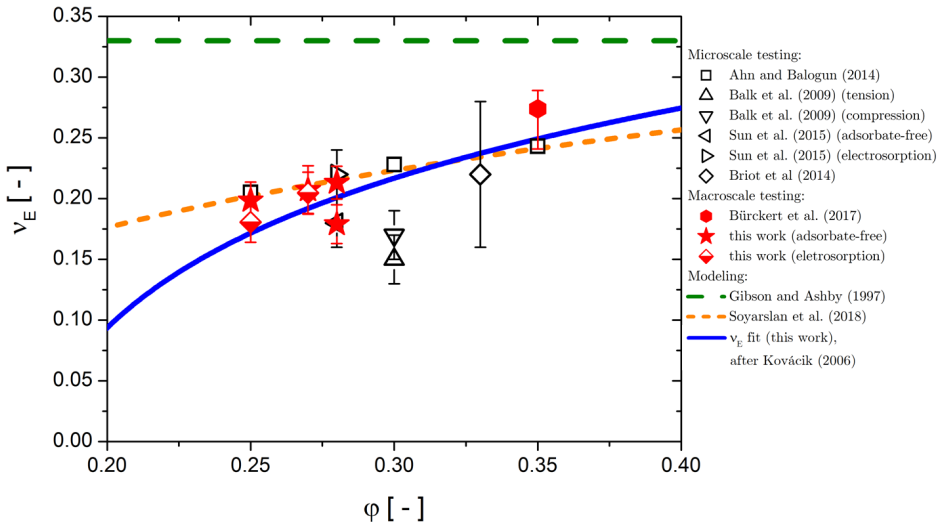

Figure 4.12: Elastic Poisson ratio data, ν_E, of nanoporous gold summarized with respect to the solid fraction, φ. Experimental investigation of microscaled samples (black, open symbols) used compression [62, 136], tensile [19, 62] and ultrasonic testing techniques [228]. Red symbols represent data from compression testing of mm-sized specimen reported in Reference [68] and the results obtained during this work (data published in References [164, 165]). Modeling approaches suggest constant values of $\nu_E = 0.33$ (green, dashed line) [129] and density depended behavior (orange, dashed [139] and blue, solid [230]).

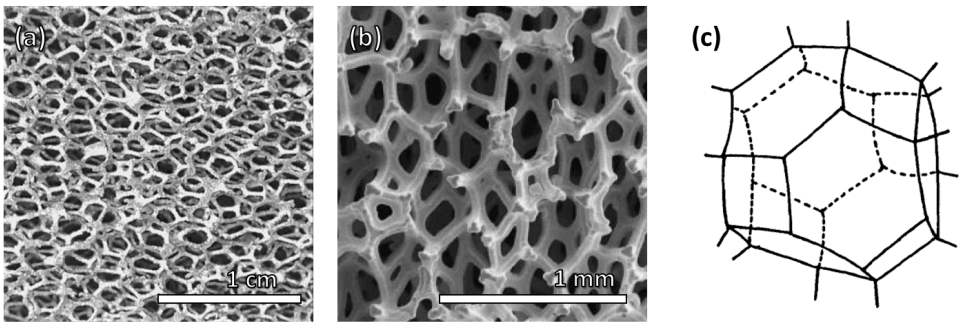

Figure 4.13: Microstructures of commercial open-porous Al- (a) [130] and Ni-foams (b) [234] with trade names ERG and Inco foam, respectively. Note that despite different structural length scales similar polyhedral morphologies can be observed. (c) Schematic of an idealized unit cell of conventional foams with tetrakaidecahedron geometry [236]. Images are reprinted with permission.

Another example highlighting the impact of structural morphology on the transverse elastic behavior of porous materials are auxetic foams. These *re-entrant foams* exhibit negative elastic Poisson ratios, which means they contract laterally upon compressive loading [232, 236]. The origin of this unusual deformation behavior is a specifically designed cell geometry. Rather than protruding outward, cell walls deflect into the interior of the structure during elastic compression [236]. Both examples illustrate that microstructural characteristics can dominate the transverse elastic response by such an extent that the atomistic nature of the material becomes irrelevant.

In case of np Au, the microstructure differs considerably from conventional foams inasmuch as ligaments vary in thickness and are randomly oriented. Numerical studies mimicking the structure of np Au by diamondoid strut arrangements find that increased structural disorder coincides with a decrease in ν_E [229]. Compared to fairly well-ordered commercial foams that provided the basis for the Gibson-Ashby model, the considerably lower ν_E values measured for np Au can be readily understood as a result of higher structural disorder.

The discussion of the mechanical behavior of np Au is often connected to model conceptions developed for metallic foams with a significantly lower density, see for instance Section 1.4. While it may be adequate to the assume density-invariant ν_E values of 0.33 for porous materials with small solid fractions, this assumption fails for material systems that are close to full densification. With a solid fraction ranging between 25 % and 40 % np Au is located between both bounding scenarios. In their numerical study on random field generated structures, that resemble np Au, *Soyarslan et al.* [139] observe a distinct dependence of ν_E with φ. While their empirical fit (orange, dashed line in Figure 4.12) coincides well with experimental data, it should be noted that the fitted curve is not significant in a physical sense. In this context, modeling concepts of sintered metals and ceramics may prove a suitable basis of comparison, since this class of porous solids covers a very large range of solid fractions from around 50 % up to nearly fully dense material. In these material systems, considerable variations of the elastic properties are observed with respect to φ. The modeling is based on the percolation theory, a concept that is used to describe various properties of connected networks, for details see Reference [237]. With this method, Young's modulus, Y, and the shear modulus, G, of porous materials can be modeled by [230]

$$Y = Y_0 \left(\frac{\varphi - \varphi_\mathrm{p}}{1 - \varphi_\mathrm{p}} \right)^{f_\mathrm{Y}}, \tag{4.1}$$

and

$$G = G_0 \left(\frac{\varphi - \varphi_\mathrm{p}}{1 - \varphi_\mathrm{p}} \right)^{f_\mathrm{G}}. \tag{4.2}$$

Here, Y_0 and G_0 designate Young's modulus and the shear modulus of the solid material, respectively. The parameters f_Y and f_G represent characteristic exponents and φ_p denotes the percolation limit. Note, the model is only valid for $\varphi > \varphi_\mathrm{p}$. For isotropic materials, Poisson's ratio can be expressed as [93]

$$\nu_\mathrm{E} = \left(\frac{Y}{2G} \right) - 1. \tag{4.3}$$

Substituting Equation 4.3 with Equations 4.1 and 4.2 yields the elastic Poisson's ratio of isotropic porous solids: [230]

$$\nu_{\mathrm{E}} = (\nu_{\mathrm{E}_0} + 1)\left(\frac{\varphi - \varphi_{\mathrm{p}}}{1 - \varphi_{\mathrm{p}}}\right)^{f} - 1. \tag{4.4}$$

With the elastic Poisson ratio of the solid material, ν_{E_0}, and the characteristic exponent, $f = f_{\mathrm{Y}} - f_{\mathrm{G}}$. In case of np Au, the value of φ_{p} is taken from Reference [139] as 0.159 and $\nu_{\mathrm{E}_0} = 0.42$ [138]. The ν_{E} data displayed in Figure 4.12 was fitted according to Equation 4.4 to estimate the value of the characteristic exponent. A value of $f = 0.086$ was obtained, the ensuing fit curve is displayed by the solid blue line. Incidentally, f of np Au is identical to sintered iron with φ ranging from 0.78 up to full densification, despite entirely different microstructural morphology [230,238]. Since f takes on a positive value in np Au – i.e. $f_{\mathrm{Y}} > f_{\mathrm{G}}$ –, it can be seen that Y is more sensitive to variations in φ than G. This is a nontrivial observation as porous solids may also exhibit constant ν_{E} values, regardless of variations in φ [129,230]. Moreover, with this modeling approach this work provides the opportunity to estimate G from existing Y data.

With the exception of ν_{E} reported by *Balk et al.* [62] the fitted curve agrees well with this work's data and literature values. Note, the lower values reported in the study by *Balk et al.* [62] may be attributed to the applied measurement technique: ν_{E} values were determined from loading rather than elastic unloading regimes. Early yielding results in a mixed elastic-plastic behavior that may reduce the apparent ν, especially given the very small ligament size of $L \approx 20$ to 35 nm where $\nu_{\mathrm{P}} << \nu_{\mathrm{E}}$.

It might be argued that error bars of ν_{E} data with different φ overlap for some studies presented in Figure 4.12. It is therefore significant that the general notion of increasing ν_{E} with φ is also supported by this work's finding that ν_{E} increases with advancing compressive deformation, i.e. densification (Figure 4.6).

4.2.3 Asymmetric yielding at small scales by the action of capillary forces

Preliminary to the discussion of the transverse deformation response during plastic flow, let us recall the central notions regarding the exploration scheme of small-scale tension–compression asymmetry in the following order:

- In elongated objects, plastic flow and surface tension, γ, are linked because deformation creates and removes surface area, A, for plastic elongation and compression, respectively. Thus, the corresponding change in energy ($\gamma\delta A$) promotes compressive shortening but impedes tensile elongation. At small scales, i.e. below an object size of roughly 100 nm, the working hypothesis is that γ causes distinct asymmetric yielding.

- Considering that the feature size of interest is very small, compressive testing of individual nanowires or -columns appears extremely difficult. Yet, exploration of randomized network structures, such as np Au, may circumvent this issue since the axial deformation state of individual struts depends on the orientation towards the principal loading direction [160]. For instance, during uniaxial compression of macroscopic np Au the deformation entails local compression of ligaments aligned with the load axis, as well as tensile-mediated deformation in orthogonally orientated ligaments.

- The value of the plastic Poisson ratio, ν_{P}, diminishes as a response to the interaction of capillary forces during macroscopic compression testing. This is a direct conse-

quence of asymmetric yielding, since the plastic tensile elongation perpendicular to the loading axis is suppressed by γ.

- Since γ determines the extent of tension–compression asymmetry, and by extension feeds into ν_P, control of γ allows for direct modulation of the transverse plastic deformation response.

The impact of γ on the transverse mechanical response during plastic, compressive flow has been explored by two different testing scenarios: in situ modulation of γ and ex situ variation of L. To begin with, the results of the in-electrolyte experiments displayed in Figure 4.7 will be the subject of discussion. The present experiments find a strong sensitivity of ν_P towards the electrode potential, E. When E is switched to more positive values, oxygen species adsorb on the surface and significantly reduce the value of γ. During compression testing, the reduction in γ is accompanied by a substantial increase in ν_P (Figure 4.10). This confirms the link between γ and ν_P.

This work's experimental in situ study was complemented by finite element simulations by Prof. Dr. Norbert Huber. In the following, a brief description of the implementation of the finite element modeling (FEM) will be given, for further details the reader is referred to References [165, 229]. The numerical study used a network structure composed of Timoshenko beam elements that where connected in randomly displaced nodes. The extent of structural disorder was calibrated on the basis of ν_E, as described in the previous section. In order to reproduce the solid fraction of the experiments ($\varphi \approx 0.26$), the ratio of strut radius to length was adjusted to 0.303. This ratio also accounts for the correction of the strengthening effect by nodal mass agglomeration, as proposed in Reference [147]. Each strut is represented by a chain of 20 beam elements that incorporate axial, bending, torsion and shear deformation modes. Uniaxial loading was implemented by a homogeneous displacement of the nodes on the top side of the randomized beam network. On the lateral faces, free displacement of the nodes was permitted. The network's deformation response was embodied in a constitutive law with linear work hardening.

In order to incorporate the extra stress required to compensate for the action of surface tension (see Section 2.3), a pipe/core configuration was chosen. This pipe element imposed an extra tensile stress on the underlying beam, as depicted Figure 4.14 (a). As a result, asymmetric yielding was introduced as seen Figure 4.14 (b) on the example of a single, axially deformed pipe/core element.

The simulations of the randomized networks confirm the anisotropic distribution of local axial strain states with respect to the loading direction (Figure 4.14 (d)) similar to Reference [160]. Moreover, the model reproduces the mechanical stress–strain response of the experiments (Figure 4.14 (e)). Most importantly, the simulations show decisive upward jumps in ν_P when γ is switched from high to low values, analogous to the experiments (Figure 4.14 (f)). Besides the influence of densification, namely the increase in ν_P with proceeding deformation (Figure 4.5), the model captures the essential physics. Therefore, the simulations support the experimental findings that the surface tension induces asymmetric yielding between tensile and compressive deformation.

In contrast to the transverse response, the deformation behavior in loading direction, that is the stress–strain response (Figure 4.10 (a, c)), can not entirely be referred to changes in surface tension. Even though a decrease in γ during electrosorption of oxygen species results in an increase in the compressive flow stress, a reduction in γ does not account for the increase in magnitude of the flow stress jumps with increasing strain. Indeed, the enhanced flow stress of np Au has been attributed to pinning of adsorbates

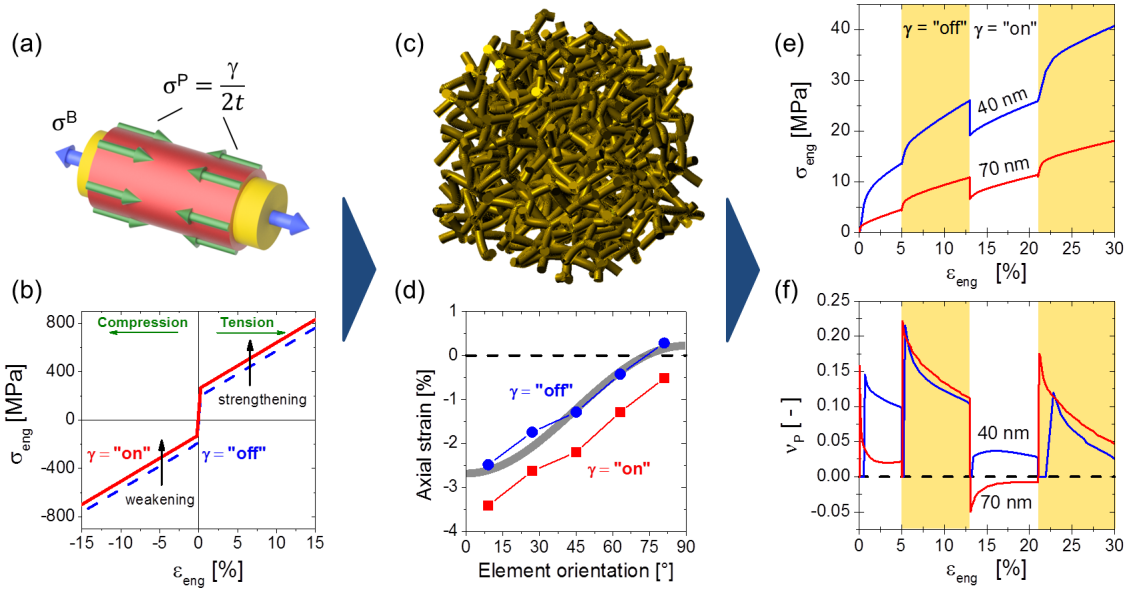

Figure 4.14: Finite element simulations of nanoporous network structures. Randomized beam elements with pipe/core configurations are used to mimic impact of the surface tension, γ, on the mechanical properties of nanoporous gold. (a) Schematic depiction of beam element modeled with two stress components. The pipe stress, σ^{P}, imposes a tensile stress irrespective of sign and magnitude of the bulk stress, σ^{B}. This concept emulates the work done against γ during plastic deformation. (b) Stress–strain behavior of a single beam element subjected to tensile and compressive loading. Results for γ switched "on" (red, solid line) and "off" (blue, dashed) show asymmetric yielding induced by capillary forces, γ promotes strengthening of the beam in tension and weakening in compression. (c) Randomized beam network underlying the numerical investigation. (d) Local strain state distribution for γ switched "on" (red squares) and "off" (blue dots) derived at 25 % macroscopic compression. Mean axial strain of beam elements plotted versus the beam's orientation towards the principal loading direction. Bold line illustrates the projected strain in an isotropic material with a plastic Poisson ratio of $\nu_{\mathrm{P}} = 0.08$. Engineering stress, σ_{eng}, (e) and ν_{P} (f) plotted versus engineering strain in loading direction, $\varepsilon_{\mathrm{eng}}$. During compressive deformation of structures representing ligament sizes of 40 nm (blue lines) and 70 nm (red lines), capillary forces are switched "on" (white regions in graph) and "off" (yellow shaded). [165]

to dislocation endpoints for oxygen covered surface states [16]. Contrary to the influence of surface tension, this effect is of dissipative nature and not connected to stored energy of surfaces. Moreover, this "adsorption locking" acts symmetrically, i.e. for tension and compression alike. Therefore, this effect does not contribute to the variation of ν_{P}. The increasing magnitude of the strengthening effect is then linked to dislocation accumulation and interaction at the pinning points [16]. In the finite element simulation, this feature is emulated by enhanced, symmetric work hardening during electrosorption.

Let us now turn to the compression tests of np Au in air. It is the key observation that samples with $L = 40\,\mathrm{nm}$ exhibit considerably lower ν_{P} values than specimens with larger feature size, i.e. $L = 70\,\mathrm{nm}$, 120 nm and 170 nm (Figure 4.5). A summary of the experimental results and a comparison to literature data with comparable solid fraction is given in Figure 4.15. Note, this work's data represents mean values of ν_{P} as determined for the first 5 % plastic strain. The bold, yellow line in Figure 4.15 serves as a guide to the

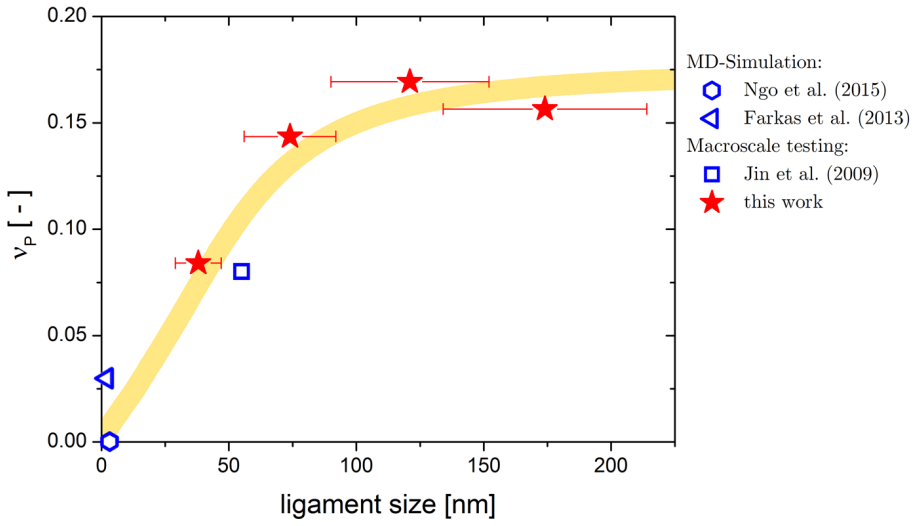

Figure 4.15: Plastic Poisson ratio data of nanoporous gold, ν_P, summarized with respect to the ligament size, L. Molecular dynamic simulations [122, 142] find near zero ν_P values at low L that increase for structures with larger feature size [61, 164]. Data points illustrating this work's findings represent mean values up to 5 % plastic strain; error bars with a confidence level of 95 % lie within data points (vertical axis). Horizontal error bars represent the standard deviation of the ligament size distribution. The bold, yellow curve illustrates a guide to the eye.

eye. The trend of diminishing ν_P values at small L is confirmed by another experimental study [61] and becomes even more significant when – near zero ν_P – values from molecular dynamics studies [122, 142] are included.

While the compression experiments in air approach the issue of local tension–compression asymmetry from a different perspective, the findings are in excellent agreement with in-electrolyte tests. Rather than varying γ itself, the general contribution of capillary forces is controlled by L. The decrease in ν_P can be understood as a result of pronounced surface effects at small characteristic structure size. From near constant ν_P at large L, it can be argued that the contribution of γ towards plastic deformation becomes negligibly small when feature sizes exceed 40 nm to 70 nm. Without external surface modulation, this may be considered a critical limit below which nanoscale objects exhibit significant asymmetric yielding behavior. Interestingly, at a feature size of around 40 nm surface atoms constitute merely 3 % of the total volume, as estimated in Figure 1.1. This highlights the considerable effect of the surfaces on the overall material properties. It should be emphasized that the investigation presented in this work is the first experimental confirmation of asymmetric yielding as a result of interaction of surface tension.

One aspect in the mechanical response of np Au that may seem to oppose the idea of surface-induced weakening in compression is the increase in compressive strength with decreasing L (Figure 4.2). This observation may be readily understood from the general deformation mode of np Au. While axial deformation components have been the focus of this work, their overall contribution to general deformation is small compared to bending and torsion modes [148], both of which exhibit symmetric tensile and compressive

contributions. Thus, size-related strengthening (see Section 1.3) of bend and twisted ligaments outweighs axial weakening in compression.

In addition to its susceptibility to capillary forces, ν_P generally entails similar morphological contributions towards the lateral deformation response as its elastic pendant. Regarding the apparent density dependence of the transverse deformation response during plastic flow, it can be argued that a ν_P value of 0.5, the general value of isotropic, incompressible matter, poses an upper limit for this trend. To the authors knowledge, there are no model conceptions reported for ν_P with regard to φ, or any other structural quantity for that matter, that enable systematic interpretation or prediction of ν_P of interconnected porous solids. The importance of ν_P with regard to full mechanical description of metallic foams and the need for a comprehensive model has also been acknowledged in the recent literature [239].

Investigation of ν_P also touches upon the discussion on the ratio between indentation hardness, H, and macroscopic yield strength, σ_y, of np Au. While fully dense solids exhibit $H/\sigma_y = 3$, materials with diminishing plastic lateral expansion – such as some low-density foams – reveal H/σ_y ratios of around 1 [240]. It is often considered that np Au densifies without lateral expansion during plastic deformation [124–127], for details see Section 1.4 in the introductory chapter. The observations of this work – $\nu_P > 0$ – serve to correct this assumption of the absence of lateral deformation in np Au. In their study on polymeric and metallic foams, *Shaw and Sata* [240] find a correlation between H and ν_P. Following the proposed trends, H/σ_y ratios emerge for np Au to a value of around 2 for samples with $L = 40\,\mathrm{nm}$ to roughly 2.6 for specimens with larger feature size. Still, the overall concept of a fixed relation between hardness and yield strength for pristine np Au is at least problematic. This is best illustrated by the difficulties of defining σ_y and will be addressed in the next chapter in more detail. It has been pointed out that no transition from purely elastic to elastic-plastic deformation occurs but rather immediate local yielding. Therefore, any new definitions of σ_y are to some extent arbitrary – and by extension any ratio with H – since they do not link directly to physical processes.

In the course of this discussion, it has become obvious that the widely recognized "smaller is stronger" relation does not account for the variation in strength of specimens that are loaded in compression. In this context, it appears appropriate to propose a concept that incorporates the tension–compression asymmetry. To start out, Equation 1.1 in Section 1.3 may serve as a basis to describe the size-dependence of the strength, σ_y, without consideration of the capillary forces. The additional traction stress, ΔT, required to compensate for the surface tension is described by Equation 2.9 in Section 2.3. The equation shows, that the surface-induced traction depends on the specimen size, D, by $\Delta T \propto D^{-1}$. Thus, σ_y may be expressed as

$$|\sigma_y| = kD^n + bD^{-1} \tag{4.5}$$

for specimens loaded in tension and

$$|\sigma_y| = kD^n - bD^{-1} \tag{4.6}$$

for specimens loaded in compression. Analog to Equation 1.1, k and b represent constant scaling parameters and n is a power-law exponent. For gold, the values of these parameters can be estimated from Figure 1.3 in Section 1.3 and Equation 2.9 in Section 2.3 as: $n = -0.6$, $k = 9 \cdot 10^3\ \mathrm{MPa\,nm^{0.6}}$ and $b = 5.5 \cdot 10^3\ \mathrm{MPa\,nm}$. Figure 4.16 shows the estimated variation of σ_y of gold with regard to D. It can be seen that the concept

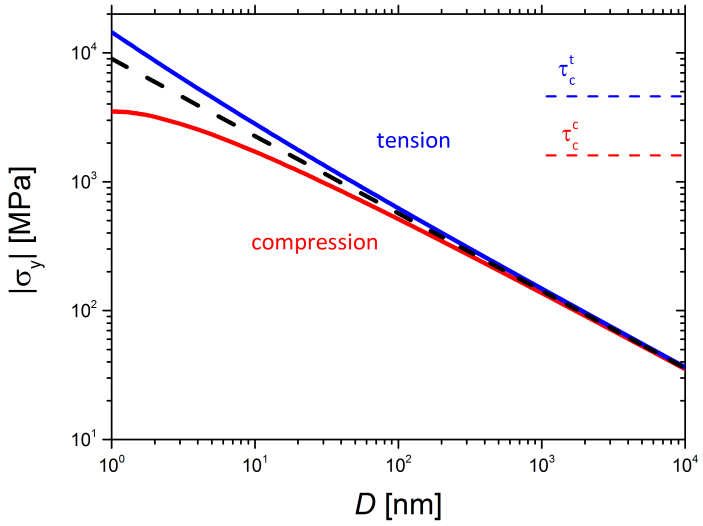

Figure 4.16: Estimated variation of the strength, σ_y, of gold with regard to the specimen size, D. The graph accounts for the surface-induced weakening in compression (red line) as well as for the strengthening effect in tension (blue line). The black dashed line represents mean values for σ_y, i.e. without consideration of asymmetric yielding. The value of the theoretical shear strength in tension, τ_c^t, (dashed blue line) and in compression, τ_c^c, (dashed red line) is adopted from Reference [241].

captures the essential notion of weakening in compression (red line) and strengthening in tension (blue line). Moreover, the observations are in distinct contrast to findings reported by *Marian and Knap* [110]. In their numerical study, the authors propose a breakdown in compressive strength at around 30 nm due to the impact of the surface stress. In opposition, Figure 4.16 finds a monotonous increase of σ_y with decreasing D down to a size of 1 nm. While no breakdown in compressive strength is found here, the onset of a transition from strengthening to weakening can be surmised at low D. It is conceivable that for material systems with higher values of γ or lower values of n, a breakdown in compressive strength may be observed at larger D. It should be noted, that at small specimen sizes σ_y approaches the theoretical shear strength, τ_c. This quantity represents the upper limit of σ_y. Numerical *ab initio* calculations for uniaxial deformation of gold along the [100]-axis suggest τ_c values of 1.6 GPa in compression and 4.2 GPa in tension [241]. These critical limits correspond to specimen sizes of 10 nm and 5 nm for samples loaded in compression and in tension, respectively. It should be kept in mind that the value of τ_c is still a subject of discussion as pointed out by the authors of the study.

5 Macroscopic bodies of a strong and deformable nanoporous base metal

5.1 Results

5.1.1 Structural characterization

Nanoporous copper-nickel

The geometry and the optical appearance of nanoporous copper-nickel (np CuNi) are illustrated in Figure 5.1 (a). The photograph shows a precursor sample machined from a $Cu_{20}Ni_{10}Mn_{70}$ master alloy (left) and a fully dealloyed np CuNi sample (right). The preparation technique yields macroscopic bodies that are, by optical appraisal, free of apparent macroscopic cracks.

Electron backscatter diffraction (EBSD) was used to visualize the grain structure of the precursor alloy. In Figure 5.1 (b), the image uses inverse pole figure coloring to illustrate the microstructure. Grain boundaries are highlighted by black lines. A single-phase face-centered cubic (fcc) crystal structure is found throughout the whole precursor. Within the limit of resolution, no significant lattice distortion is found inside the grains, with the exception of preparation-induced scratches. With an average grain size measured to roughly 500 µm, the grains are comparatively large. The EBSD characterization indicates texture from the shape of the grains which – considering the sample's orientation within the ingot – coincides with the direction of solidification from the walls of the cold crucible into the melt.

The master alloy was investigated in more details by transmission electron microscopy (TEM). Figure 5.2 (a) shows the image section that was investigated with respect to its chemical composition (b-d) by energy dispersive X-ray spectroscopy (EDS). The EDS maps show that Cu, Ni and Mn are homogeneously distributed. Furthermore, TEM was also employed to investigate the crystal structure of the precursor alloy by low magnification diffraction analysis. In image panel (e) of Figure 5.2, the investigated area is indicated by the beam spot (bright region). The corresponding diffraction pattern is given in Figure 5.2 (f). The analysis finds an essentially perfect fcc structure without local lattice distortion at small scales. These observations support the low-resolution EBSD findings. Both techniques thereby confirm that the homogenization and quenching of the master alloy yields a single-phase homogeneous solid solution. As described in Sections 2.1 and 3.2.1, this is considered a prerequisite for the formation of homogeneous nanoporous bodies.

The scanning electron micrographs in Figure 5.3 illustrate the microstructure of np CuNi samples in as-dealloyed condition (a,b) and annealed at 400 °C in argon gas for 45 min (c,d). It can be seen that np CuNi exhibits a homogeneous, bicontinuous network structure that resembles other nanoporous metals made by dealloying [61, 64, 72]. However, the ligaments of np CuNi take on a significantly different shape than in other dealloyed materials, see for instance the micrographs of np Au in Figure 4.1. Polyhedral

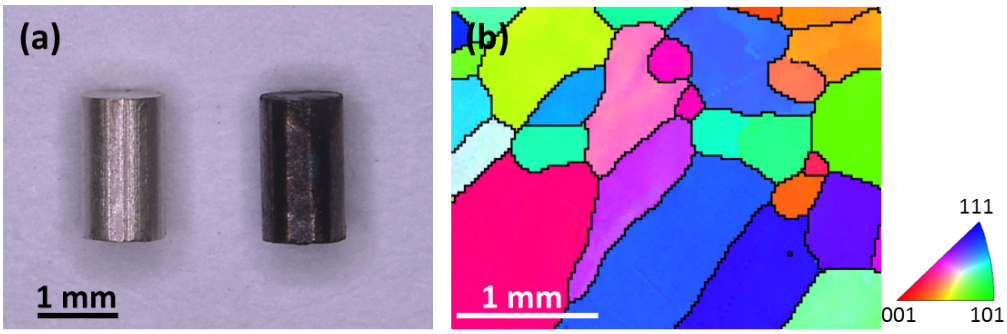

Figure 5.1: Structural analysis of nanoporous copper-nickel (np CuNi) and its precursor alloy. (a) Photographs show a machined $Cu_{20}Ni_{10}Mn_{70}$ precursor (left) and as-dealloyed np CuNi (right). (b) Electron backscatter diffraction map, depicted in conventional inverse pole figure coloring. The image illustrates the grain structure of the master alloy; grain boundaries are highlighted by black lines. Panel (b) published in Reference [166].

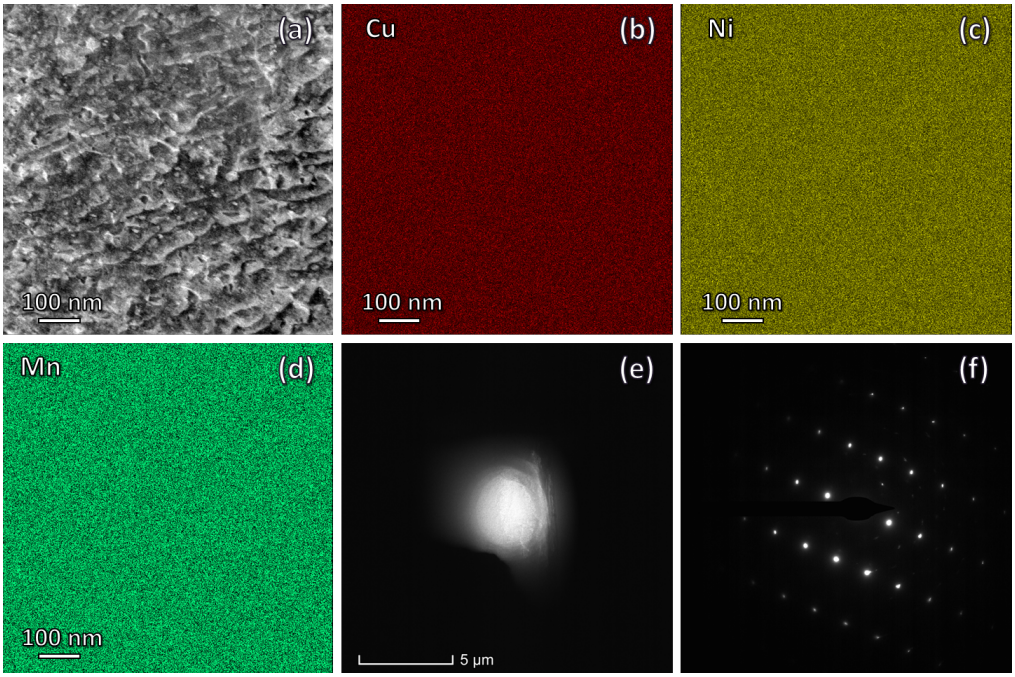

Figure 5.2: Transmission electron microscopy of the $Cu_{20}Ni_{10}Mn_{70}$ precursor alloy. (a-d) Energy dispersive X-ray spectroscopy characterization: microscopy image (a) and elemental distributions maps for Cu (b), Ni (c) and Mn (d). Note, elements are distributed homogeneously. (e, f) Low magnification diffraction analysis of the precursor alloy: (e) beam spot indicating the investigated region of interest. (f) Diffraction pattern of (e). The analysis confirms a perfect fcc lattice structure in the master alloy.

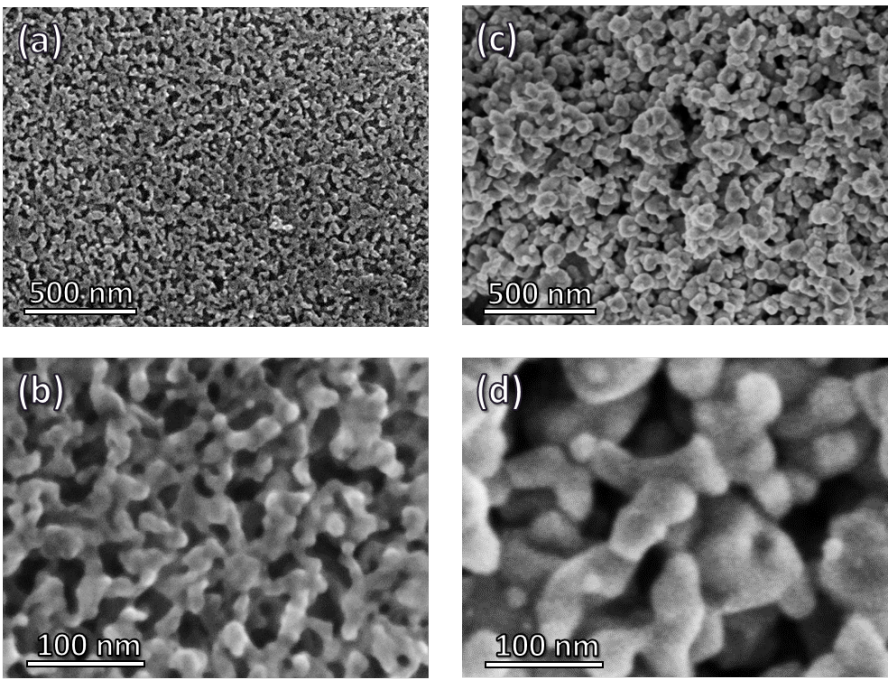

Figure 5.3: Microstructural characterization of as-dealloyed (a, b) and annealed (c, d) nanoporous copper-nickel with a ligament size of 13 ± 4 nm and 40 ± 14 nm, respectively. Images show electron micrographs of cross-sectional areas at low (top row) and high (bottom row) magnification. Note, the differently shaped ligaments compared to nanoporous gold. [166]

shaped ligaments are observed in np CuNi that point towards different mechanisms of formation. This observation will be explored in more detail further on in this section. In contrast to other studies on nanoporous base metals [64, 87], np CuNi appears free of dealloying-induced cracks down to the microscale.

In the as-prepared state, np CuNi exhibits a very small ligament size, L, of 13 ± 4 nm. Analog to nanoporous gold (np Au), L can be controlled by thermal coarsening. Annealing at 400 °C in argon gas for 20 min, 30 min and 45 min leads to feature sizes of $L = 22 \pm 6$ nm, 32 ± 8 nm and 40 ± 14 nm, respectively. As with np Au, the density and solid fraction of the nanoporous samples were determined from the sample volume and the mass. Regardless of thermal annealing conditions, np CuNi exhibits constant density and solid fraction of 2.75 ± 0.11 g/cm^3 and 0.31 ± 0.01, respectively. Compared to other macroscopic nanoporous metals [72,87,143], np CuNi exhibits hardly any shrinkage during dealloying and – even more significantly – during thermal annealing.

EDS analysis by scanning electron microscopy was used to identify the elemental composition of np CuNi. By measurement of eight samples – each with at least three differently located areas of interest (see Section 3.3.1) – the elemental composition of Cu, Ni and Mn was identified as 60 ± 6 at.%, 32 ± 4 at.% and 8 ± 2 at.%, respectively. Note, no systematic variations in the chemical composition are observed between the different measurement spots, i.e. at the sample center, edge and in between.

In order to investigate the ligament structure of np CuNi in more detail, TEM imaging was consulted. Figure 5.4 shows exemplary results. White squares within the central overview image refer to different regions of interest (a-d) that have been examined with

respect to their crystallographic orientation. Fast Fourier transforms (FFT) of the micrograph are displayed adjacent to the respective image sections. The FFT contain information on local structure, similar to conventional diffraction patterns. It can be seen that peak positions vary between image sections. This corresponds to different local crystallographic orientations. These findings therefore suggest that the ligaments of np CuNi are made of nanocrystallites with a grain size that agrees with the ligament size. In this respect, np CuNi differs considerably from np Au, where grains are orders of magnitude larger than the ligament size [61].

Grain boundaries may provide attractive sites for pinch-off and loss of connectivity during coarsening. However, Figure 5.3 qualitatively suggests that np CuNi seems to retain its morphology during coarsening, in the sense that no abnormal loss of connections is observed.

Figure 5.5 displays local element distributions in as-dealloyed np CuNi, as measured by EDS during TEM analysis. Intensities refer to the maximum concentration measured for the respective element. The average elemental contributions agree well with EDS data measured by scanning electron microscopy. The most striking finding can be identified from an overlay of Cu (red) and Ni (green) distributions as depicted in (d). The image clearly shows inhomogeneous elemental distribution with separated clusters of Ni and Cu-rich regions whose dimensions coincide with the ligament size, i.e. the grain size. These observations are particularly noteworthy since elements in the master alloy are evenly distributed, as shown in Figure 5.2 (a-d).

Moreover, Figure 5.5 (e) shows that residual Mn (red) is exclusively concentrated within the Ni-rich (green) regions. The mixed yellow color also suggest that Mn is evenly distributed among the Ni clusters.

X-ray diffraction was used to identify the crystallographic structure of the master alloy (Figure 5.6 (a)) as well as as-dealloyed (b) and annealed (c) np CuNi. Identification of phases was based on reference patterns by References [242, 243]. The analysis finds a single-phase solid solution with fcc symmetry (red diamonds) in the homogenized $Cu_{20}Ni_{10}Mn_{70}$ master alloy, which further supports the EBSD and TEM findings. As shown in Figure 5.6 (b), the diffraction pattern of as-dealloyed np CuNi likewise reveals fcc crystal orientation. Furthermore, the signature of a second phase is observed that can be ascribed to Cu_2O (blue dots). Similar phases are found in annealed np CuNi (Figure 5.6 (c)). It can be seen that the phase fraction of Cu_2O diminishes during annealing as indicated by the loss of intensity compared to metallic fcc.

The lattice parameters were estimated from fcc peak positions as 374.9 ± 0.4 pm, 360.9 ± 0.2 pm and 360.3 ± 0.3 pm for the precursor alloy, as-dealloyed and annealed np CuNi, respectively.

Elemental nanoporous copper and nickel

As a comparison to np CuNi, the microstructures of macroscopic samples of elemental nanoporous copper (np Cu) and elemental nanoporous nickel (np Ni) have been investigated by electron microscopy, as illustrated by images (a, b) and (c, d) of Figure 5.7, respectively. Images (a) and (b) show that np Cu exhibits a homogeneous network structure with smooth ligaments that appears very similar to np Au. With a ligament size measured as $L = 30 \pm 6$ nm, the microstructure of np Cu is significantly coarser than as-dealloyed np CuNi. Most notably, the large cracks observed in the micrographs are not a result of intentional sample cleaving but rather proprietary to the dealloyed structure,

Figure 5.4: Structural analysis of as-dealloyed nanoporous copper-nickel by transmission electron microscopy. White squares within the central overview image refer to different regions of interest (a-d) that have been investigated in more detail. Adjacent to their respective image sections, the fast Fourier transforms show that local crystal orientations vary between ligaments. Note, this nanocrystalline microstructure differs significantly from other nanoporous metals in which ligaments typically exhibit common lattice orientations within a larger scaled grain structure.

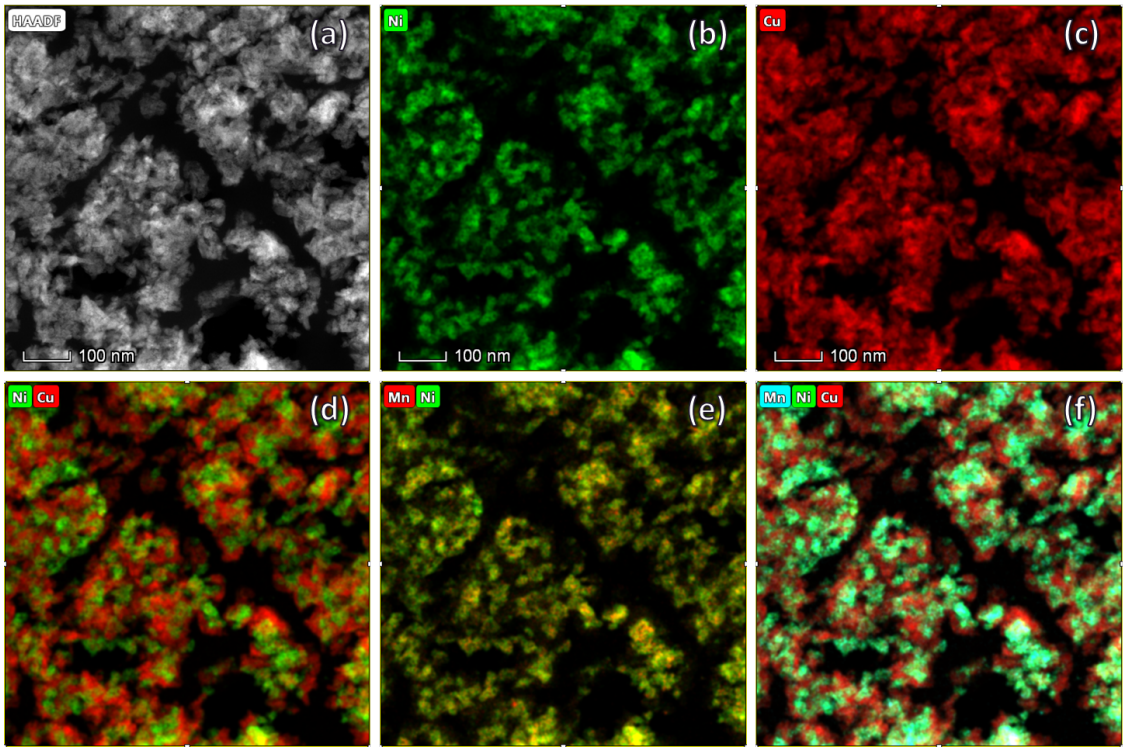

Figure 5.5: Energy dispersive X-ray spectroscopy characterization of nanoporous as-dealloyed copper-nickel by transmission electron microscopy. (a) Dark-field image of the selected area. Elemental distribution maps are for: Ni (b), Cu (c), Cu (red) and Ni (green) (d), Mn (red) and Ni (green) (e) and Mn (turquoise), Ni (green) and Cu (red) (f). The intensity is scaled to the respective maximum concentration. Significant clustering of Cu and Ni is observed (d). Residual Mn is found exclusively in Ni-rich clusters (e, f).

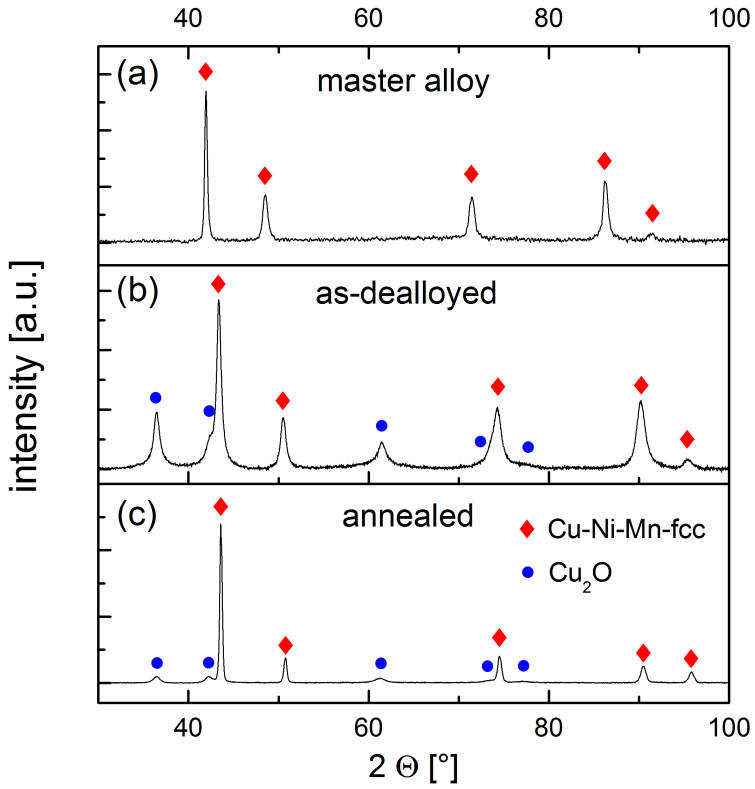

Figure 5.6: X-ray diffraction analysis of nanoporous copper-nickel (np CuNi) and its precursor alloy. Linearly scaled intensity profiles with subtracted background noise are plotted vs. 2-theta. The graph shows diffraction patterns for: (a) the precursor alloy, (b) as-dealloyed np CuNi and (c) np CuNi annealed for 45 min at 400 °C in purified argon gas. Symbols refer to the corresponding phases: face-centered cubic metallic Cu-Ni-Mn (red diamonds) and Cu_2O (blue dots). Reference patterns are based on References [242, 243].

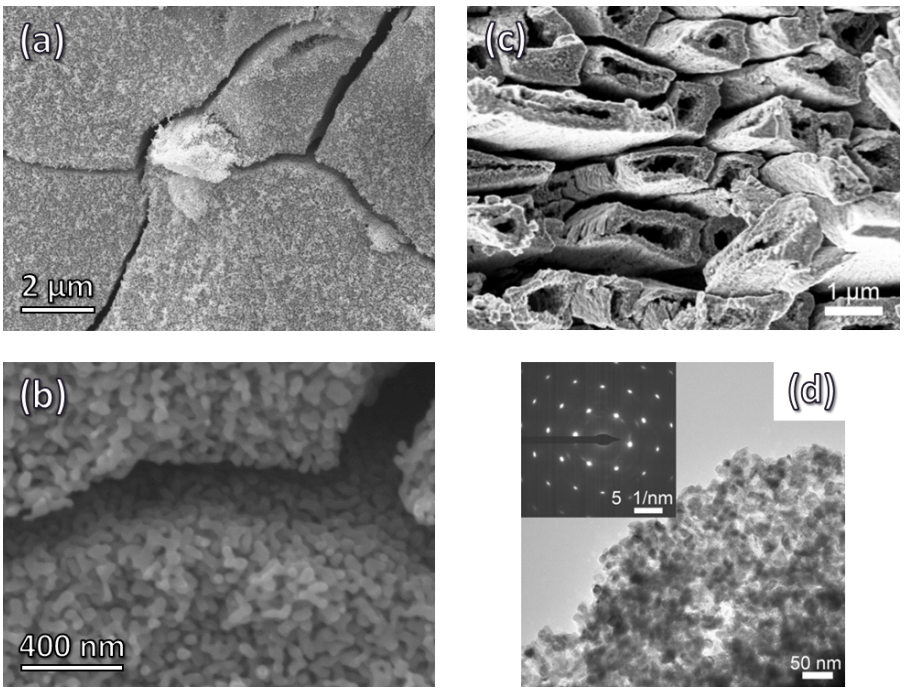

Figure 5.7: Microstructure of elemental nanoporous copper (np Cu, (a, b)) and nanoporous nickel (np Ni, (c, d)); images are taken from the sample's interior. Np-Cu exhibits a homogeneous network structure with large cracks and smooth ligaments with an average diameter of $L = 30 \pm 6\,\mathrm{nm}$. (c) Low magnification micrographs of np Ni show a tubular microstructure with distinct gaps between them. (d) At small scales, transmission electron images find a nanoporous structure with a ligament size of around $10 \pm 3\,\mathrm{nm}$ and common crystal orientation (see inset in (d)). Images (c) and (d) are published in Reference [87].

as observed from surface micrographs and optical inspection. Density and solid fraction of as-prepared np Cu are determined as $2.73 \pm 0.16\,\mathrm{g/cm^3}$ and 0.31 ± 0.02, respectively.

While np Cu exhibits a microstructure similar to np Au, low magnification micrographs of np Ni (Figure 5.7 (c)) show a tubular structure. The dealloying-induced channels are aligned with the corrosion front that is orientated normal to the outer sample surface. Distinct gaps can be observed around the channels that severely reduce the toughness of the material and lead to brittle failure. At smaller scales, TEM imaging finds a nanoporous structure with L of around $10 \pm 3\,\mathrm{nm}$, as depicted in Figure 5.7 part (d). A common crystallographic orientation within the ligament structure is observed by TEM diffraction analysis, see inset in Figure 5.7 (d). Lattice parameters have been identified by X-ray diffraction as 369.8 pm and 352.4 pm for the $Ni_{30}Mn_{70}$ precursor alloy and as-dealloyed np Ni, respectively. This corresponds to a volume reduction of around 15.6 % which is substantial. Thus, the tubular microstructure of np Ni may be understood as result of large shrinkage-induced stresses that are relieved by ordered cracking. Indeed, similar crack patterns are found in shrinkage related processes, such as cooling of basalt columns or mud crack formation during drying [244, 245].

In the as-dealloyed state, np Ni exhibits a density of around $2.90 \pm 0.10\,\mathrm{g/cm^3}$ which corresponds to a solid volume fraction of around 0.33 ± 0.01.

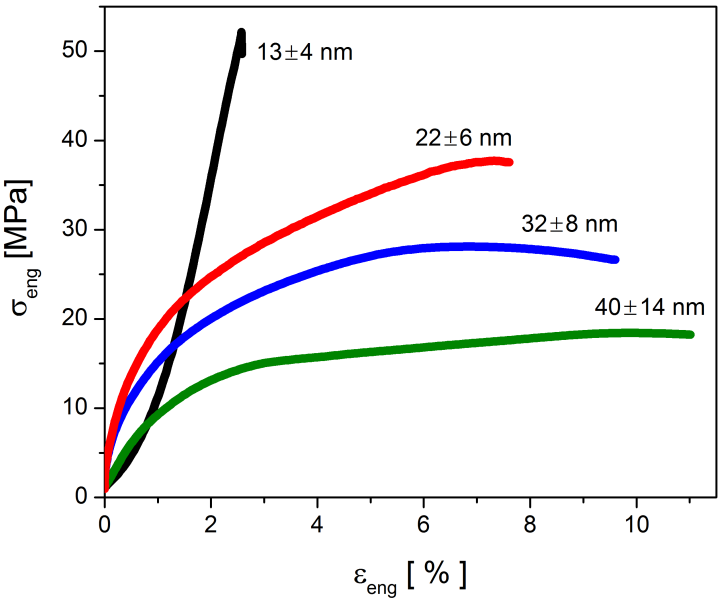

Figure 5.8: Uniaxial compression tests of nanoporous copper-nickel (np CuNi) with different ligament sizes, L; engineering stress, σ_{eng}, plotted vs. engineering strain, $\varepsilon_{\mathrm{eng}}$. Brittle deformation behavior is observed for as-dealloyed np CuNi (black line), whereas annealed structures (colored lines) exhibit significant deformability in compression. [166]

5.1.2 Uniaxial compression of macroscopic samples

Nanoporous copper-nickel

Results of uniaxial compression tests on np CuNi are shown in Figure 5.8. In the plot of engineering stress, σ_{eng} versus engineering strain, $\varepsilon_{\mathrm{eng}}$, graphs are depicted for as-dealloyed np CuNi (black line) and samples annealed for 20 min, 30 min and 45 min at 400 °C with corresponding ligament sizes (colored lines). The experiments show that upon compression as-dealloyed np CuNi exhibits brittle deformation behavior similar to other studies on nanoporous base metals [64, 75, 77, 78, 87, 88, 90]. Still, np CuNi exhibits a fracture stress of more than 50 MPa. This exceeds the strength values reported for other nanoporous metals, such as those in References [61, 62, 68, 75, 78].

In the case of annealed np CuNi, considerable deformability is observed during compression testing. The effect becomes more pronounced with increasing L. To the author's knowledge, this work provides the first proof of significant plasticity ever reported for a nanoporous base metal with feature sizes relevant for surface-induced functionalization.

Figure 5.9 shows strain maps obtained by digital image correlation for annealed np CuNi. Samples with ligament sizes $L = 22$ nm, 32 nm and 40 nm are depicted at an average compressive engineering strain in loading direction of 4.4 %, which is well in the regime of plastic flow. Color maps display distributions of axial strain (top row) and the maximum two-dimensional shear strain (bottom row). Strain concentrations are observed in the axial strain maps (a-c), i.e. in deformation in loading direction. It can be seen that the strain concentrations exhibit significantly higher deformation than the

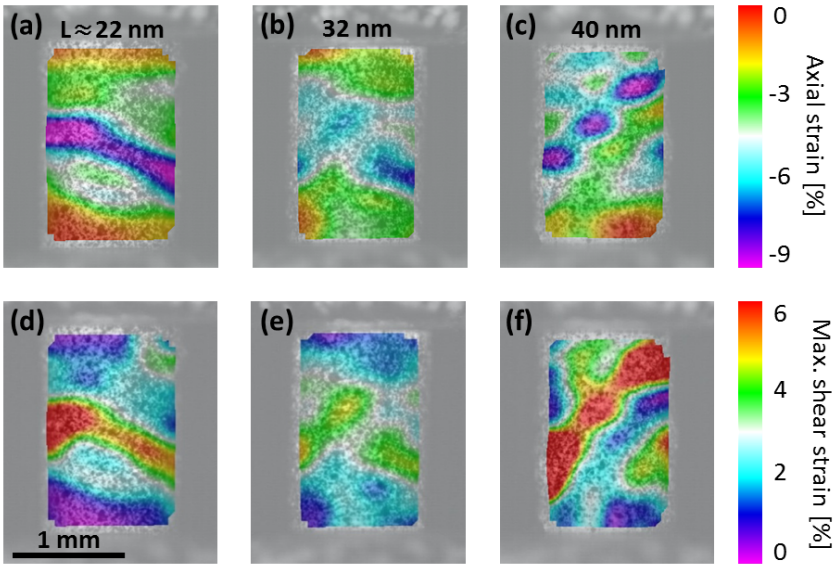

Figure 5.9: Strain distributions in annealed nanoporous copper-nickel (np CuNi) with different ligament sizes, L, under compressive loading. Deformation state captured at an average axial engineering strain of 4.4 %. Axial (top row) and maximum shear strain maps (bottom row) depicted for np CuNi with $L = 22\,\text{nm}$, 32 nm and 40 nm reveal distinct localized deformation behavior. [166]

surrounding material. Magnitude of the measured maximum shear values (d-f) suggest that shearing contributes significantly towards the deformation of np CuNi. Also, the maximum shear is inhomogeneously distributed and concentrated in the same regions as the axial deformation. The ultimate failure is observed along the shear deformation bands.

Elemental nanoporous copper and nickel

Figure 5.10 shows exemplary compressive stress-strain curves of elemental np Cu (red) and np Ni (green). It can be seen, that both materials exhibit brittle deformation behavior similar to as-dealloyed np CuNi and other studies on np Cu [77,78] and np Ni [88,90]. Yet, the fracture stresses of np Cu and np Ni are considerably lower than in np CuNi. A detailed collection of strength data for np Cu, np Ni and np CuNi is presented further on in this chapter. Moreover, in contrast to np CuNi, elemental np Cu and np Ni samples show brittle deformation regardless of any annealing procedure.

5.1.3 Actuation behavior

Nanoporous copper-nickel

Figure 5.11 illustrates the actuation behavior of as-dealloyed np CuNi. As described in Section 3.3.6, the samples were measured in alkaline environment while imposed to cyclic voltammetry. The current density (blue line) shows that np CuNi exhibits a significantly more complex reaction signature than nanoporous gold. Studies of planar Cu [246] and Ni

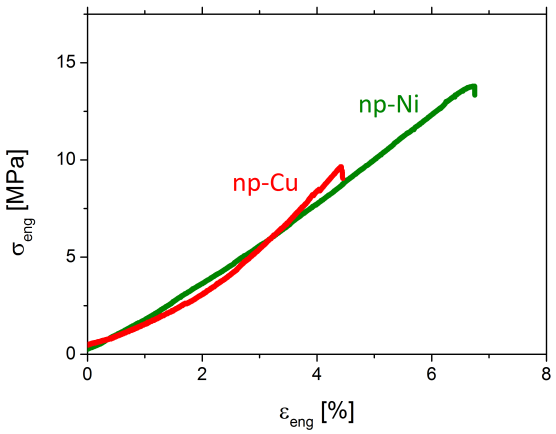

Figure 5.10: Exemplary compression tests of elemental nanoporous copper and nanoporous nickel with a solid fraction of 0.33. Both materials exhibit brittle deformation behavior independent of any coarsening treatment.

electrodes [247] suggest that the electrochemical response of np CuNi can be understood as a result of superimposed reactions at the individual Cu and Ni-rich phases. Note that the current response in this graph is referred to the sample mass rather than to the surface area. This is due to the complex reactions that occur in many base metals which renders conventional assessment approaches of the surface area – such as the method applied for np Au in this work – useless [225]. The red line depicts the actuation strain. Arrows indicate scan directions for both quantities.

The experiments find a variation in strain of around 0.9 %. A monotonous decrease of the strain is observed during positive potential scanning. The actuation response is large compared to pure np Au that typically exhibits maximum electrochemical actuation strains up to around 0.1 % [2,6]. Yet, when alloyed with other elements – such as platinum – the actuation response of np Au can extent up 1.3 % [3, 4]. Moreover, studies on nanoporous palladium find huge actuation strains of up to around 4 % as a result of hydrogen absorption into the metallic lattice [71].

Elemental nanoporous copper and nickel

The actuation response of elemental np Cu differs significantly from np CuNi. When subjected to the same electrochemical conditions as np CuNi in Figure 5.11, no noticeable actuation strain is measured.

Quite the opposite behavior is found for elemental np Ni. In alkaline solution large actuation strains of up to 1.6 % are measured, as depicted in Figure 5.12. A similar trend for monotonous contraction (red line) during positive scanning as in np CuNi is observed. Still, for np Ni, pronounced variation in strain is found at high potentials. The current density response (blue line) indicates full surface coverage with β-Ni(OH)$_2$ without remaining α-Ni(OH)$_2$ [247]. A detailed analysis of the electrochemical reactions of np Ni in alkaline solutions – and their impact on the actuation response – will be given in Section 5.2.3 further on in this chapter.

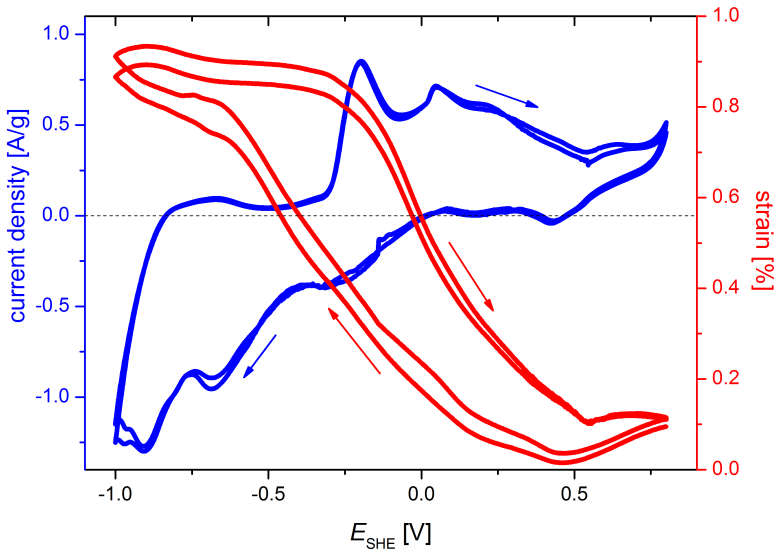

Figure 5.11: Actuation response of as-dealloyed nanoporous copper-nickel during potential cycling in 1 M NaOH electrolyte. Current density (blue line) and actuation strain (red line) are plotted vs. the applied electrical potential, E_{SHE}. Data shows two successive scans with a scan rate of $1\,\mathrm{mV\,s^{-1}}$. The arrows indicate scan directions.

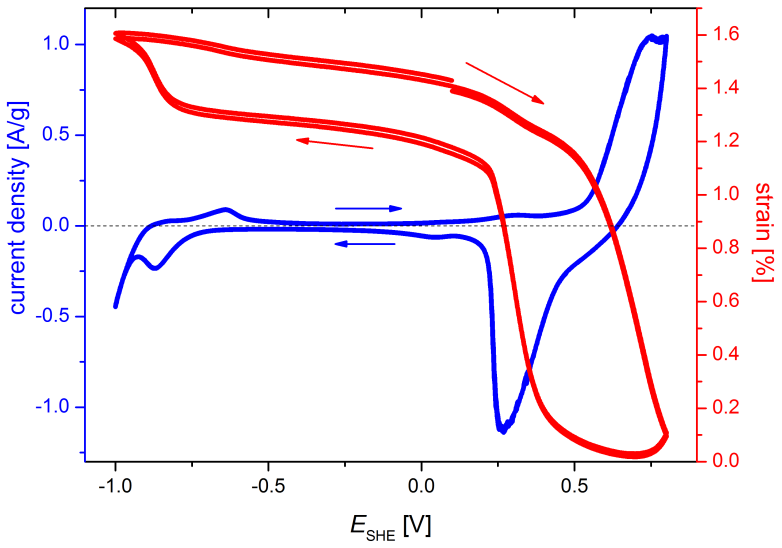

Figure 5.12: Actuation response of elemental nanoporous nickel during potential cycling in 1 M NaOH electrolyte. Current density (blue line) and actuation strain (red line) are plotted vs. the applied electrical potential, E_{SHE}. A maximum actuation amplitude of around 1.6 % is measured. Data shows two successive scans with a scan rate of $1\,\mathrm{mV\,s^{-1}}$. The arrows indicate scan directions. Data published in Reference [87].

5.2 Discussion

5.2.1 Structural evolution during dealloying

The structural characterization of np CuNi has revealed several interesting aspects that have not been observed in other dealloyed nanoporous base metals, so far:

- The synthesis scheme produced macroscopic bodies devoid of macro- and microscopic cracks alike.
- Ligaments are composed of nanocrystallites with a grain size that agrees with the ligament diameter.
- Inhomogeneous elemental distribution is observed on the scale of the grain size with separate Cu and Mn-rich Ni clusters.
- The dealloyed bodies appear to exhibit a single metallic face-centered cubic lattice structure.

Let us start the discussion on the origin of the nanoporous composite formation right before dealloying of the $Cu_{20}Ni_{10}Mn_{70}$ master alloy. Investigations of the precursor alloy find an undistorted single-phase metallic fcc structure composed of very large grains. This emphasizes that nanocrystallinity forms during the dealloying process. Along with nanocrystal formation, local elemental separation can also be considered to occur during dealloying. This is due to the observation that all constituents are evenly distributed in the master alloy. X-ray diffraction analysis measures a significant amount of oxides in np CuNi. Yet, Pourbaix diagrams of Cu [248] and Ni [249], see Figure 5.13, suggest that during electrochemical dealloying no formation of Cu- or Ni-oxides may occur. In this respect, it can be assumed that the oxides are native layers that form after the dealloying, when exposed to air. Thus, the microstructure formation during dealloying can be considered free of any influences that might accompany the formation of oxygen species.

After dealloying, Mn is homogeneously distributed in the Ni clusters with a roughly constant Ni to Mn ratio of 4 : 1, as determined by EDS. At this composition, binary phase diagrams suggest a single-phase intermetallic Ni_3Mn structure with a wide solubility range of Mn (15 at.% to 29 at.%) [221]. X-ray diffraction analysis finds a single metallic fcc crystal structure. This gives rise to the assumption that metallic Cu and intermetallic Ni_3Mn share a coherent fcc lattice structure. Indeed, with lattice parameters, a, of around 360.9 ± 0.2 pm and 360.3 ± 0.3 pm for as-dealloyed and annealed np CuNi, respectively, the measured values range between the larger sized Cu ($a = 361.5$ pm [242]) and the smaller lattice structure of Ni_3Mn ($a = 358.9$ pm [250]). It should be emphasized that no signatures of a metallic Ni phase are found. The very small a of 352.4 pm [242] should ether lead to strong distortions of a potentially coherent lattice or to the formation of a second fcc structure. Neither of these scenarios is observed. Note, a of Ni_3Mn is reported for a pure and well-annealed ordered material. Yet, small quantities of Cu are soluble in Ni_3Mn – up to around 9 % [251] – which are found to entirely inhibit long-range ordering in Ni_3Mn [251,252]. The absence of long-range order in Ni_3Mn is supported by the X-ray diffraction analysis which finds no order-related diffraction signatures. It can be assumed that a of disordered Ni_3Mn is larger than the literature value since disordering increases the lattice constant by up to 1 % [253][1].

[1] In Cu_3Au, the reference system for the cP4 crystal structure of Ni_3Mn, disordering leads to an increase

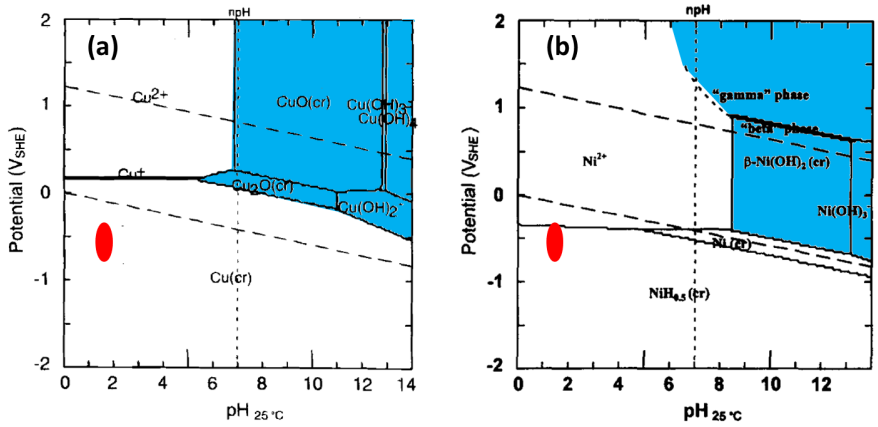

Figure 5.13: Pourbaix diagrams of (a) copper [248] and (b) nickel [249] in H_2O at 25 °C and a concentration of dissolved species of 10^{-6} mol kg^{-1}. Blue shaded regions indicate regimes of oxide and hydroxide formation. Dealloying conditions of nanoporous copper-nickel are highlighted in red. Note, no formation of oxides is expected to occur during electrochemical dealloying. Graphs modified and reprinted with permission.

The formation of coherent Cu and Ni_3Mn phases during dealloying accounts for all of the above observations. In the following, a concept is derived that interprets the formation mechanisms during electrochemical dealloying of np CuNi. A schematic illustration of the proposed mechanism is displayed in Figure 5.14. At the onset of dealloying, Cu, Ni and Mn atoms are statistically distributed within a single-phased solid solution (a). During the corrosion process, Mn-ions are removed from the surface until local concentrations reach composition ranges required to form Ni_3Mn nucleation centers along the corrosion front (b). Surface diffusion leads to redistribution and agglomeration of atoms, as described in Section 2.1. In this process, Ni and – to some extent Mn – preferentially alloy into the intermetallic Ni_3Mn nuclei due to the strongly negative enthalpy of solution. As previously noted, limited solubility of Cu in any intermetallic NiMn phase including Ni_3Mn is found in the Cu-Ni-Mn system [251, 254]. Moreover, simple cohesion energy estimates based on Miedema's model [255] lead to similar conclusions, since alloying of Mn into Ni is energetically more favorable than in to Cu [255].

At this stage, ligaments form that consist of numerous Ni_3Mn nuclei within a Mn-depleted Cu-Ni-Mn solid solution. As dealloying proceeds, Ni and Mn atoms are depleted from the solid solution into growing coherent Ni_3Mn precipitates. Eventually, only Cu remains in the erstwhile solid solution, as coherent Ni_3Mn precipitates reach their final volume fraction, as depicted by Figure 5.14 (c, left side). Finally, during the concurrent redistribution processes, Cu and Ni_3Mn precipitates consolidate within the ligament into separate grains with different chemical composition but coherent lattice structure (c, right side). Transmission electron imaging finds a distribution of crystal orientations between ligaments. This suggest that coherency may be limited to individual ligaments only.

Crack formation has been observed during preparation of elemental np Cu and np Ni (Figure 5.7). In both material systems, the evolution of cracks has been attributed to lattice shrinkage during dealloying [64,87]. It is argued that, due to a mismatch in lattice

in a of around 0.2 % [253].

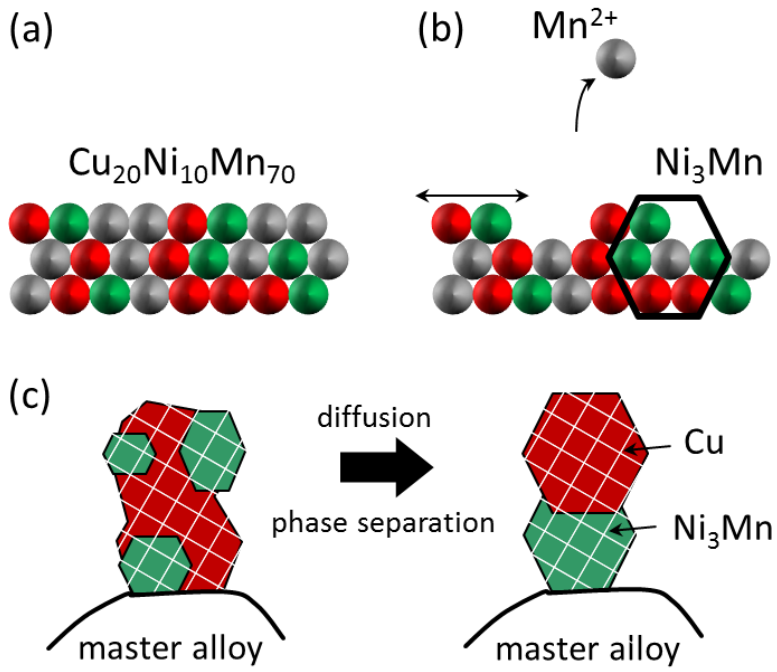

Figure 5.14: Schematic illustration of the proposed formation mechanism of the nanocrystalline composite microstructure of nanoporous copper-nickel. (a) Prior to dealloying, elements are homogeneously distributed in the $Cu_{20}Ni_{10}Mn_{70}$ master alloy. (b) Onset of dealloying: Mn^{2+} ions (grey) are dissolved into the electrolyte, unfavorable Cu (red) and Ni adatoms (green) diffuse along the surface. Ni_3Mn nucleation sites form during local variation of the elemental composition. (c) Within a single ligament Ni and Mn atoms are depleted from the solid solution as Ni_3Mn grows into coherent precipitates, as indicated by the white grid (left side). While only Cu remains in the erstwhile solid solution, concurrent redistribution of Cu and Ni_3Mn forms separated grains. During this process a coherent lattice structure is maintained (right side).

parameters at the corrosion front, shrinkage-induced stresses arise during preparation and are relieved by cracking. As discussed above, np CuNi exhibits similar lattice shrinkage during dealloying as elemental np Cu (around 4 %). Yet, no cracks are found in the microstructure. This observation may be attributed to different formation mechanisms during sample preparation. Ligament shapes and TEM diffraction analysis suggest that np Cu and np Ni retain their precursor grain structure during dealloying, similar to np Au. In np CuNi, however, formation of nanocrystals can readily relieve the shrinkage-induced stresses since the crystallites constitute a new and less distorted crystal lattice as opposed to the imposed precursor grain structure in np Cu and np Ni.

5.2.2 Deformation behavior of nanoporous copper-nickel

In order to assess the mechanical performance of np CuNi, a compilation of strength values is given in Figure 5.15. Next to this work's mechanical results on elemental np Cu and np Ni[2], the graph contains literature data of macroporous copper [256–258] and nickel foams [259, 260] and additional studies on np Cu [75, 77, 78]. As described in the discussion on np Au, defining a meaningful yield stress, σ_y, of nanoporous metals – especially for those with significant plasticity – is not trivial. In Figure 5.15, σ_y of nanoporous metals was taken as the fracture stress for entirely brittle materials such as np Cu , np Ni, as-dealloyed np CuNi and References [77, 78]. In case of the single indentation study [75], σ_y was estimated by a hardness, H, to yield strength ratio of $\sigma_y = H/3$. For annealed np CuNi, typical methods of determining σ_y fail, since the stress–strain response (Figure 5.8) shows no linear elastic regime as well as no peak stress that merges into a constant plateau region. For this reason, σ_y of annealed np CuNi is taken as the stress value at an axial engineering strain of 2 %, that is close to the fracture strain of as-dealloyed np CuNi. The same evaluation scheme has been applied to macroporous foams with stress–strain responses similar to annealed np CuNi such as those reported in Reference [256].

Figure 5.15 shows than np CuNi is strong compared to the compiled data. The basis of the exceptional mechanical performance of np CuNi is the absence of dealloying-induced cracks. Moreover, the very small ligament size may also contribute to the high strength in the form of a "smaller is stronger" relation, as discussed in the previous chapter on np Au. The trend is confirmed by the decrease in strength during coarsening, as indicated by the blue arrow.

Moreover, due to the high ratio of surface area to volume of np CuNi, the nature of the surface may affect the mechanical behavior. X-ray diffraction confirms significant contributions of native oxides that form after dealloying. As can be seen from Figure 1.1 in the introductory chapter, the total volume fraction of the oxide layer can be substantial, especially in as-dealloyed np CuNi. In this respect, a layer of hard oxides around the metallic ligament core may substantially strengthen the network structure similar to reinforced composite materials. It becomes apparent that this strengthening mechanism considerably exceeds the contributions which are typically associated with oxide layer formation – such as "adsorption locking" which has been discussed for np Au – however, at the expense of plasticity as discussed further on in this section.

Solid solution strengthening may be another conceivable effect that contributes to the high strength of np CuNi compared to elemental np Cu and np Ni[3]. In their study on

[2]Unpublished data for np Ni by Dr. Chuan Cheng and the present author.

[3]Note, np Ni samples with $\varphi > 0.3$ need to be considered as alloyed materials since significant amounts

np Au alloyed with minor amounts of Pt, *Ye and Jin* [69] demonstrated that even small amounts of alloying elements can result in a significant increase in strength of nanoporous metals. Similar strengthening behavior may be expected from alloying of minor amounts of Cu in the Ni-rich phase and vice versa.

The nanocrystalline microstructure is arguably the most decisive feature that distinguishes the mechanical response of np CuNi from other nanoporous metals. It can be expected, that dislocation motion can be severely hindered by the additional grain boundaries [261]. It has also been pointed out in Section 1.4, that ligaments of nanoporous metals such as np Au are considered to share common glide planes within considerably larger grains. In these materials, dislocations can move between adjacent ligaments in the form of pore channel dislocations [143]. However, in np CuNi different crystal orientations between neighboring ligaments will severely obstruct the formation of this type of dislocation, thus motion of dislocations might be limited to the ligament interior. In this respect, the deformation behavior of np CuNi may be dominantly carried by sliding of grain boundaries rather than conventional dislocation motion [261]. This has been proposed as a principle deformation mechanism in massive nanocrystalline materials with a grain size below 50 nm [262].

While the origin of brittle deformation in np Cu and np Ni can be clearly attributed to crack formation, plasticity of np CuNi is reduced – and even inexistent for as-dealloyed samples – compared to np Au, despite the crack-free microstructure of np CuNi. One reason for this may again be the nanocrystalline nature of np CuNi. In the discussion on the deformation behavior of np Au (Section 4.2.1) it was argued that local stress concentrations can be dissipated by the formation of pore channel dislocations. Referring to this argument, it can be assumed that obstruction of long-range dislocation motion favors inhomogeneous stress distributions and thereby provides crack formation sites. Another origin of the pronounced brittleness in np CuNi may be related to surface oxidation. In contrast to monolayer adsorbates of np Au, native surface oxides of Cu and Ni extent to 3.3 nm [25] and 1.1 nm [24] in thickness, respectively. In this context, the small ligament size of as-dealloyed np CuNi ($L = 13 \pm 4$ nm) may turn out to be problematic since the share of brittle oxides to the overall volume becomes considerable, especially in Cu-rich nanocrystals (Figure 1.1 (b)). From this line of argument, the increase in plasticity with L can be readily understood as the ratio of brittle surface oxides to ductile metal core decreases with increasing L, as demonstrated by X-ray diffraction analysis of as-dealloyed and annealed np CuNi (Figure 5.6). In this context, future compression experiments on np CuNi under electrical potential control in electrolyte, similar to those conducted on np Au, may provide insights regarding the impact of surface oxides on plasticity and strength.

Plastically deformed np CuNi reveals localized deformation zones that are in distinct contrast to strain distributions observed during compression of np Au (see Figure 4.4). In fact, the axial deformation behavior of np CuNi resembles the "crush bands" that appear during compression of macroporous foams [129, 203]. As described earlier, the formation of crush bands is carried by the collective collapse of adjacent cell walls. This results in a characteristic stress drop, followed by an extended plateau regime of nearly constant stress. Yet, compression tests of annealed np CuNi (Figure 5.8) find no signs of stress maxima at early loading stages. On the contrary, they show continuous hardening during plastic deformation – similar to np Au. Moreover, inhomogeneous maximum shear strain maps suggest that strain concentrations during plastic deformation of annealed np CuNi

of residual Mn remain within the structure during synthesis.

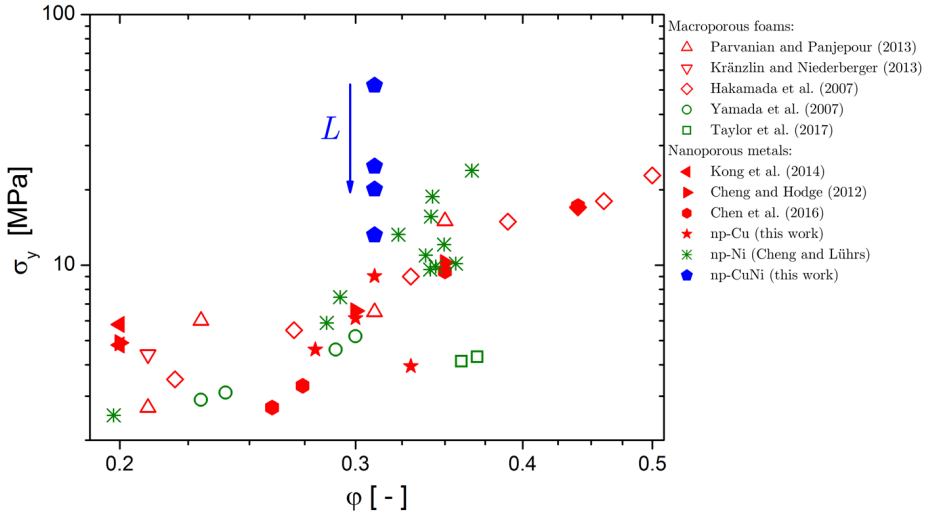

Figure 5.15: Compressive strength data of nanoporous metals (filled symbols) and macroporous foams (open symbols) plotted with respect to the solid fraction. The colors of the data points refer to the sample's elemental composition: copper [75, 77, 78, 256–258], nickel [259, 260] and copper-nickel are depicted in red, green and blue, respectively. It can be seen that nanoporous copper-nickel is significantly stronger than porous materials composed of elemental copper or nickel with comparable solid fraction. The blue arrow indicates the reduction in strength as a consequence of coarsening.

can be attributed to shearing, which ultimately leads to failure.

The inhomogeneous shearing during compression of np CuNi resembles observations reported for massive nanocrystalline metals, where distinct shear bands are formed immediately after yielding at grain sizes below a few hundred nm [262, 263]. Next to microstructural parameters and elemental composition, inhomogeneous shearing is considered a result of the lack of work hardening. This is a consequence of the constant dislocation density in nanocrystalline metals [263] – in these materials dislocations are assumed to annihilate at grain boundaries in a rate similar to their formation [262]. Although np CuNi exhibits noticeable strain hardening in compression – in contrast to bulk nanocrystalline materials – hardening is not limited to dislocation interaction but also entails contributions of densification. Hence, similar underlying mechanisms for shear band formation can not be ruled out.

5.2.3 Functionalization potential

Considerable functionalization potential has been demonstrated for np CuNi by the large actuation response during potential cycling (Figure 5.11). While no potential-induced length change is measured for np Cu, experiments on np Ni find significant actuation strains during cyclic voltammetry (Figure 5.12). This suggest that the reversible electrochemical elongation of np CuNi in alkaline solution can be attributed to length changes of the Ni-rich regions. In agreement with References [87, 92], three additive processes emerge:

- Ab- and desorption of hydrogen into the Ni-lattice at low electrical potential

($-1.0\,\mathrm{V} < E_{\mathrm{SHE}} < -0.6\,\mathrm{V}$) causes volume expansion and contraction, respectively.

- Capacitive double-layer charging induces surface strain that varies linearly with the applied electrical potential ($-0.6\,\mathrm{V} < E_{\mathrm{SHE}} < 0.05\,\mathrm{V}$) [1].
- The reversible redox reaction β-$\mathrm{Ni(OH)_2} + \mathrm{OH^-} \longleftrightarrow \beta$-$\mathrm{NiOOH} + \mathrm{H_2O} + \mathrm{e^-}$ that occurs at high potentials ($0.05\,\mathrm{V} < E_{\mathrm{SHE}} < 0.8\,\mathrm{V}$) induces a surface strain as a result of a lattice mismatch between β-$\mathrm{Ni(OH)_2}$ and β-NiOOH.

Especially the last process differs from length changes observed during oxidation of noble metals, such as Pd [71], Pt [1] and Au-Pt [3]. In these materials, surface oxidation causes expansion of the underlying bulk. In contrast, the described redox reaction leads to shrinkage of the Ni lattice [92]. This effect adds to the continuous contraction caused by the first two mechanisms during positive potential scanning.

While the continuous contraction is observed for both, np CuNi as well as np Ni, the curve progression of np Ni suggests a stronger variation of the actuation strain at high potentials. In np Ni, the three proposed actuation mechanisms can be clearly distinguished from the voltammogram and the strain response (Figure 5.12). In contrast, the voltammogram and the actuation strain of np CuNi suggest no clear distinction between the capacitive charging and the reversible redox reaction of the Ni-rich regions (Figure 5.11). In alloys, the electrochemical gradient between the different species can alter the onset and reactivity of electrochemical reactions [264, 265]. It is conceivable that in a three-species system, such as np CuNi, this effect may be responsible for the deviation of the actuation response of np CuNi from elemental np Ni.

Naturally, actuation strains of np CuNi are smaller compared to pure np Ni due to the reduced fraction of contributing elements, yet actuators are by definition mechanically loaded devices and as such profit from increased strength and plasticity. A similar argument holds for the conceivable use of np CuNi as mechanical sensor material. In this scenario, the sensor relies on the same electro-chemo-mechanical coupling principles as the presented actuator. A selection of functionalization opportunities of np CuNi is given in the outlook section of the next chapter.

6 Conclusion

6.1 Insights into nanoscale mechanics by macroscopic testing

At small scales, the literature reports distinct strengthening behavior in the form of a "smaller is stronger" relation. Yet, at specimen sizes below around 100 nm numerical studies and theoretical considerations predict a reduction in compressive strength. It is argued that this tension–compression asymmetry is a result of the action of capillary forces – namely the *surface tension*, γ – at the surface of the material. Experimental proof supporting this notion has been missing so far, since experimental investigation of the compression behavior of single nanowires or -columns is challenging.

This thesis picks up on the above-mentioned contradiction by experimental investigation of nanoporous gold (np Au), a well-established model material for the exploration of surface-induced variations of the mechanical behavior. The material is fabricated in macroscopic dimensions by electrochemical dealloying. Macroscale testing of np Au samples appears as a suitable technique to explore asymmetries during plastic flow. This is so because uniaxial deformation of randomly orientated networks – such as np Au – contains signatures of both, tensile- and compressive-mediated contributions. These can be identified from the transverse plastic response of the nanoporous network structure.

In this work, elastic and plastic Poisson ratios, ν_{E} and ν_{P}, respectively, of mm-sized np Au samples are determined through full-field analysis of compression tests in air and in electrolytic environment. Surface contributions are systematically varied by thermal tuning of the ligament size and electrochemical modulation. The experiments find ν_{E} values independent of the applied electrical potential and the overall surface contribution. It is argued that variations in surface excess elasticity do not influence the material's elastic transverse response on a macroscopic level. Compared to other mechanical characteristics of np Au, the measurements of ν_{E} reveal considerable robustness of this material parameter towards different characterization techniques. Values and trends of ν_{E} are discussed with respect to other porous systems and it is emphasized that conventional foam models do not apply to nanoporous metals. The measurement of ν_{P} finds distinct non-zero values. In contrast to the elastic transverse deformation, ν_{P} exhibits significant susceptibility towards both, electrochemical modulation and surface area variation alike. A distinct increase in ν_{P} values with decreasing contribution of γ is observed, an effect that is fully reversible for electrochemically modulated surface states. These observations prove that γ promotes weakening in compression and strengthening in tension and confirm the decisive contribution of the surface to small-scale plasticity. Thus, this work provides the first experimental proof of asymmetric yielding at small scales through the interaction of capillary forces.

6.2 Synthesis and mechanical behavior of a novel nanoporous base metal

Numerous application scenarios have been proposed for nanoporous metals. Yet, for technological relevance three key properties are required: significant functionalization potential, mechanical robustness and low preparation costs. While many studies prove substantial material performance in individual fields, no nanoporous metal combines all three aspects, so far.

In this work, a novel synthesizes scheme is developed to prepare mm-sized nanoporous copper-nickel (np CuNi) by dealloying in aqueous media. Single-phased $Cu_{20}Ni_{10}Mn_{70}$ master alloys are prepared and electrochemically dealloyed in 1 M KCl + 10 mM HCl solution. The microstructural characterization finds crack-free nanoporous networks. In distinct contrast to other nanoporous metals, these are composed of nanocrystalline ligaments with an average size of 13 nm. Moreover, an inhomogeneous elemental distribution suggests a two-phase nanocomposite structure. A concept is derived that accounts for the unique microstructural observations. It is argued that elemental segregation occurs during dealloying into intermetallic Ni_3Mn and pure metallic Cu nanocrystals.

Uniaxial compression tests show that np CuNi is strong compared to other nano- and macroporous materials with similar constituents and solid fraction. Most importantly, annealed np CuNi exhibits significant plasticity during compression testing, a unique deformation response for nanoporous base metals with substantial surface area to volume ratio. The underlying deformation mechanisms are discussed with respect to ligament size, composition, grain structure and oxide formation.

Finally, dilatometer analysis was employed to identify the actuation response of np CuNi during potential cycling in alkaline solution. The measurement finds considerable actuation strains of around 0.9 %. These experiments provide a proof of principle which suggests that np CuNi exhibits significant surface functionalization potential.

In summary, this thesis introduces the first synthesis concept that accounts for the required material properties that are listed in the first paragraph. Specifically, the preparation from low-cost base metals yields macroscopic np CuNi, a nanocrystalline porous network structure that proves considerable mechanical stability and functionalization opportunities.

6.3 Outlook

Experiments presented in this work found a reduction in ν_P with decreasing values of the ligament size, L. Trends that suggest diminishing ν_P values at very small L are based on molecular dynamics simulations using embedded atom potentials. It has been argued that this simulation approach might not capture the essential physics at surfaces [120]. Experimental investigation of ν_P at this small length scale proves problematic as np Au, in its elemental form, exhibits a lower feature size limit of a few tens of nm. However, ligament sizes of np Au can decrease to values as low as 6 nm when alloyed with Pt [3,69]. This material system offers mechanical investigation opportunities at very small scales and may help to clarify the predicted diminishing value of ν_P.

The development of np CuNi provides the basis for the exploration of a variety of technological opportunities. A small selection will be proposed in the following.

Nanoporous metals covered with electrically conductive polymer layers promise significant improvement in the actuation response, especially with regard to the actuation

rate [266, 267]. While np CuNi might merely serve as an electrically conductive scaffold in this scenario – since the functionality is provided by the polymeric layer – its good mechanical properties, low density, high surface area to volume ratio and low-cost precursor materials makes np CuNi a superior choice compared to noble nanoporous metals.

Nanoporous alloys of copper-nickel exhibit interesting magnetic properties. This has recently been demonstrated on thin films of np CuNi that were fabricated by templating [268]. The study finds a variation in the Kerr signal at different electrical potentials [268] which suggests that the magnetization of np CuNi can be modified by electrochemistry. Indeed, preliminary tests on this work's macroscopic np CuNi samples observe reversible modulation of the magnetization by electrochemical cycling as demonstrated in Figure 6.1. In these measurements, only the Ni-rich regions are considered to contribute to this effect as pure Cu is diamagnetic [73]. A similar finding has been pointed out in the discussion of the actuation response of np CuNi. Here, functionality is also solely provided by the Ni containing phase. Therefore, future works may focus on the homogeneous distribution of Ni on the surface of np CuNi. In this context, different coating techniques might be suitable such as chemical or electrochemical plating as well as atomic layer deposition. Another conceivable approach may be transformation of the nanoporous Cu-Ni_3Mn composite into a single-phase Cu-Ni solid solution. After dealloying, Mn may be further depleted electrochemically from the Ni_3Mn phase by careful control of the dissolution rate to reduce imposed shrinkage stresses to a minimum. Eventually, this post-treatment may turn Ni_3Mn into metallic Ni. Alloying of metallic Cu and Ni phases into a solid solution may then be initiated by annealing.

Rather than using np CuNi directly, fully dense nanocrystalline composites may be obtained by compaction of the porous body. Numerous studies have demonstrated a variety of methods to prepared metallic nanocrystalline composites, such as gas phase condensation [269] or severe mechanical deformation [270]. While these methods produce nanocomposites with grain size down to around 10 nm [270], they are laborious and limited to very small geometries. Electrolytic co-deposition of immiscible constituents is a more resourceful method but appears to be limited to grain sizes of around 30 nm to 50 nm [271]. In this respect, np CuNi may be a useful composite system as large amounts may be fabricated at a grain size of around 13 nm.

Finally, the developed preparation scheme may not be limited to copper-nickel but might be extended to other base metal systems. Single-phased binary solutions with a high concentration of sacrificial Mn can be fabricated by alloying with Fe [272], Co [273] and V [274]. Another requirement is met as polarization experiments in 1 M KCl + 10 mM HCl electrolyte confirm a sufficiently large difference in corrosion potential of more than 0.8 V between Mn and the proposed alloying candidates, as demonstrated in Figure 6.2. Furthermore, phase diagrams of Fe, Ni and Mn [221, 272, 275] as well as cohesion energy considerations [255] suggest that formation of nanoporous nanocomposites composed of Fe and Ni_3Mn may form analogous to np CuNi during dealloying of ternary Fe-Ni-Mn solid solutions.

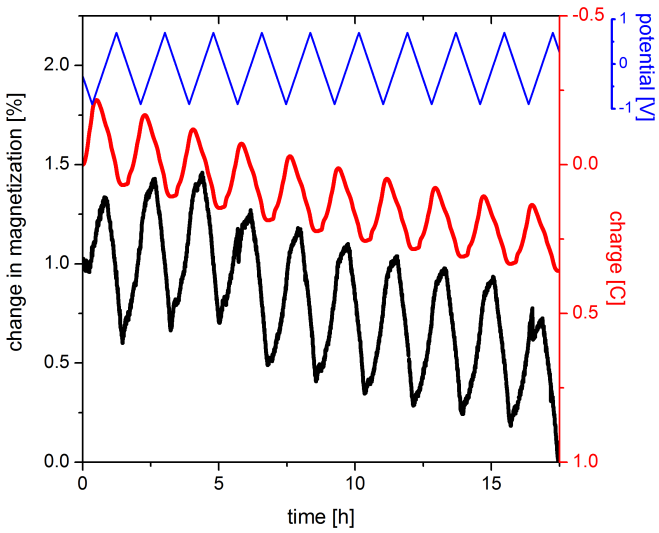

Figure 6.1: Magnetic characterization of annealed nanoporous copper-nickel by SQUID magnetometry during potential cycling in 0.1 M NaOH electrolyte. Change in magnetization (black line), charge (red) and applied electrical potential (blue) are plotted vs. the time. Unpublished data by Markus Gößler, Prof. Dr. Roland Würschum and the present author.

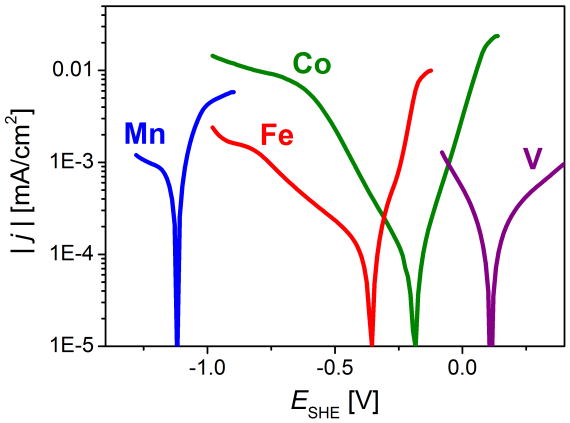

Figure 6.2: Polarization curves of pure metals obtained from linear potential sweeps with a scan rate of 20 mV s^{-1} in 10 mM HCl + 1 M KCl electrolyte. A significant difference in corrosion potentials is observed between Mn and Fe, Co and V.

Bibliography

[1] J. Weissmüller, R. N. Viswanath, D. Kramer, P. Zimmer, R. Würschum, and H. Gleiter. Charge-induced reversible strain in a metal. *Science*, 300(5617):312–315, 2003.

[2] H.-J. Jin, S. Parida, D. Kramer, and J. Weissmüller. Sign-inverted surface stress-charge response in nanoporous gold. *Surf. Sci.*, 602(23):3588–3594, 2008.

[3] H.-J. Jin, X.-L. Wang, S. Parida, K. Wang, M. Seo, and J. Weissmüller. Nanoporous Au-Pt Alloys As Large Strain Electrochemical Actuators. *Nano Lett.*, 10(1):187–194, 2010.

[4] H.-J. Jin and J. Weissmüller. Bulk Nanoporous Metal for Actuation. *Adv. Eng. Mater.*, 12(8):714–723, 2010.

[5] E. Detsi, Z. G. Chen, W. P. Vellinga, P. R. Onck, and J. T. M. De Hosson. Actuating and Sensing Properties of Nanoporous Gold. *J. Nanosci. Nanotechnol.*, 12(6):4951–4955, 2012.

[6] C. Stenner, L.-H. Shao, N. Mameka, and J. Weissmüller. Piezoelectric Gold: Strong Charge-Load Response in a Metal-Based Hybrid Nanomaterial. *Adv. Funct. Mater.*, 26(28):5174–5181, 2016.

[7] J. Zhang, P. Liu, H. Ma, and Y. Ding. Nanostructured Porous Gold for Methanol Electro-Oxidation. *J. Phys. Chem. C*, 111(28):10382–10388, 2007.

[8] A. Wittstock, V. Zielasek, J. Biener, C. M. Friend, and M. Baumer. Nanoporous Gold Catalysts for Selective Gas-Phase Oxidative Coupling of Methanol at Low Temperature. *Science*, 327(5963):319–322, 2010.

[9] T. Jin, M. Yan, Menggenbateer, T. Minato, M. Bao, and Y. Yamamoto. Nanoporous copper metal catalyst in click chemistry: Nanoporosity-dependent activity without supports and bases. *Adv. Synth. Catal.*, 353(17):3095–3100, 2011.

[10] E. Seker, W.-C. Shih, and K. J. Stine. Nanoporous metals by alloy corrosion: Bioanalytical and biomedical applications. *MRS Bull.*, 43(01):49–56, 2018.

[11] H. Oppermann and L. Dietrich. Nanoporous gold bumps for low temperature bonding. *Microelectron. Reliab.*, 52(2):356–360, 2012.

[12] K. Mohan, N. Shahane, R. Liu, V. Smet, and A. Antoniou. A Review of Nanoporous Metals in Interconnects. *JOM*, 70(10):2192–2204, 2018.

[13] Y. Xue, J. Markmann, H. Duan, J. Weissmüller, and P. Huber. Switchable imbibition in nanoporous gold. *Nat. Commun.*, 5:4237, 2014.

[14] J. Rösler and D. Mukherji. Design of nanoporous superalloy membranes for functional applications. *Adv. Eng. Mater.*, 5(12):916–918, 2003.

[15] X. Lang, A. Hirata, T. Fujita, and M. Chen. Nanoporous metal/oxide hybrid electrodes for electrochemical supercapacitors. *Nat. Nanotechnol.*, 6(4):232–236, 2011.

[16] H.-J. Jin and J. Weissmüller. A Material with Electrically Tunable Strength and Flow Stress. *Science*, 332(6034):1179–1182, 2011.

[17] X.-L. Ye and H.-J. Jin. Electrochemical control of creep in nanoporous gold. *Appl. Phys. Lett.*, 103(20):201912, 2013.

[18] N. Mameka, J. Markmann, H.-J. Jin, and J. Weissmüller. Electrical stiffness modulation - Confirming the impact of surface excess elasticity on the mechanics of nanomaterials. *Acta Mater.*, 76:272–280, 2014.

[19] S. Sun, X. Chen, N. Badwe, and K. Sieradzki. Potential-dependent dynamic fracture of nanoporous gold. *Nat. Mater.*, 14(9):894–898, 2015.

[20] N. Mameka, J. Markmann, and J. Weissmüller. On the impact of capillarity for strength at the nanoscale. *Nat. Commun.*, 8(1):1976, 2017.

[21] G. Ertl. *Reactions at solid surfaces*. Wiley, Hoboken, NJ, 2009.

[22] J. Weissmüller. *Electrocapillarity of Solids and its Impact on Heterogeneous Catalysis*, chapter 5, pages 163–220. John Wiley & Sons, 2014.

[23] J. Biener, A. Wittstock, T. Baumann, J. Weissmüller, M. Bäumer, and A. Hamza. Surface Chemistry in Nanoscale Materials. *Materials*, 2(4):2404–2428, 2009.

[24] E. S. Lambers, C. N. Dykstal, J. M. Seo, J. E. Rowe, and P. H. Holloway. Roomtemerature oxidation of Ni(110) at low and atmospheric oxygen pressures. *Oxid. Met.*, 45(3-4):301–321, 1996.

[25] P. Keil, D. Lützenkirchen-Hecht, and R. Frahm. Investigation of room temperature oxidation of Cu in air by Yoneda-XAFS. *AIP Conf. Proc.*, 882:490–492, 2007.

[26] A. Mathur and J. Erlebacher. Size dependence of effective Young's modulus of nanoporous gold. *Appl. Phys. Lett.*, 90(6):061910, 2007.

[27] D. A. Walker, E. K. Leitsch, R. J. Nap, I. Szleifer, and B. A. Grzybowski. Geometric curvature controls the chemical patchiness and self-assembly of nanoparticles. *Nat. Nanotechnol.*, 8(9):676–681, 2013.

[28] Z. Wang, S. Ning, P. Liu, Y. Ding, A. Hirata, T. Fujita, and M. Chen. Tuning Surface Structure of 3D Nanoporous Gold by Surfactant-Free Electrochemical Potential Cycling. *Adv. Mater.*, 29(41):1–7, 2017.

[29] J. Biener, A. Wittstock, L. A. Zepeda-Ruiz, M. M. Biener, V. Zielasek, D. Kramer, R. N. Viswanath, J. Weissmüller, M. Bäumer, and A. V. Hamza. Surface-chemistry-driven actuation in nanoporous gold. *Nat. Mater.*, 8(1):47–51, 2009.

[30] N. T. Panagiotopoulos, A. Moreira Jorge, I. Rebai, K. Georgarakis, W. J. Botta, and A. R. Yavari. Nanoporous titanium obtained from a spinodally decomposed Ti alloy. *Microporous Mesoporous Mater.*, 222:23–26, 2015.

[31] M. Kreuzeder, M.-D. Abad, M.-M. Primorac, P. Hosemann, V. Maier, and D. Kiener. Fabrication and thermo-mechanical behavior of ultra-fine porous copper. *J. Mater. Sci.*, 50:634–643, 2015.

[32] J. Rösler, O. Näth, S. Jäger, F. Schmitz, and D. Mukherji. Fabrication of nanoporous Ni-based superalloy membranes. *Acta Mater.*, 53(5):1397–1406, 2005.

[33] O. Näth, A. Stephen, J. Rösler, and F. Vollertsen. Structuring of nanoporous nickel-based superalloy membranes via laser etching. *J. Mater. Process. Technol.*, 209(10):4739–4743, 2009.

[34] C. L. Liao, C. W. Chu, K. Z. Fung, and I. C. Leu. Fabrication of nanoporous metal electrode by two-step replication technique. *J. Alloys Compd.*, 441(1-2):1–6, 2007.

[35] K. Shin, K. A. Leach, J. T. Goldbach, D. H. Kim, J. Y. Jho, M. Tuominen, C. J. Hawker, and T. P. Russell. A Simple Route to Metal Nanodots and Nanoporous Metal Films. *Nano Lett.*, 2(9):933–936, 2002.

[36] O. D. Velev and E. W. Kaler. Structured porous materials via colloidal crystal templating: from inorganic oxides to metals. *Adv. Mater.*, 12(7):531–534, 2000.

[37] P. Jiang, J. Cizeron, J. F. Bertone, and V. L. Colvin. Preparation of Macroporous Metal Films from Colloidal Crystals. *J. Am. Chem. Soc.*, 121(34):7957–7958, 1999.

[38] Y. Ding, A. Mathur, M. Chen, and J. Erlebacher. Epitaxial Casting of Nanotubular Mesoporous Platinum. *Angew. Chemie Int. Ed.*, 44(26):4002–4006, 2005.

[39] S. Tang, S. Vongehr, Y. Wang, J. Cui, X. Wang, and X. Meng. Versatile synthesis of high surface area multi-metallic nanosponges allowing control over nanostructure and alloying for catalysis and sers detection. *J. Mater. Chem. A*, 2(10):3648–3660, 2014.

[40] K. Sai Krishna, C. S. S. Sandeep, R. Philip, and M. Eswaramoorthy. Mixing Does the Magic: A Rapid Synthesis of High Surface Area Noble Metal Nanosponges Showing Broadband Nonlinear Optical Response. *ACS Nano*, 4(5):2681–2688, 2010.

[41] C. Zhu, S. Guo, and S. Dong. Rapid, general synthesis of pdpt bimetallic alloy nanosponges and their enhanced catalytic performance for ethanol/methanol electrooxidation in an alkaline medium. *Chem. - A Eur. J.*, 19(3):1104–1111, 2013.

[42] B. C. Tappan, M. H. Huynh, M. A. Hiskey, D. E. Chavez, E. P. Luther, J. T. Mang, and S. F. Son. Ultralow-Density Nanostructured Metal Foams: Combustion Synthesis, Morphology, and Composition. *J. Am. Chem. Soc.*, 128(20):6589–6594, 2006.

[43] B. C. Tappan, S. A. Steiner, and E. P. Luther. Nanoporöse Metallschäume. *Angew. Chemie*, 122(27):4648–4669, 2010.

[44] Z. Hua, Y. Deng, K. Li, and S. Yang. Low-density nanoporous iron foams synthesized by sol-gel autocombustion. *Nanoscale Res. Lett.*, 7(1):129, 2012.

[45] W. Yang, X.-G. Zheng, S.-G. Wang, and H.-J. Jin. Nanoporous Aluminum by Galvanic Replacement: Dealloying and Inward-Growth Plating. *J. Electrochem. Soc.*, 165(9):C492–C496, 2018.

[46] C. Wang and Q. Chen. Reduction-Induced Decomposition: Spontaneous Formation of Monolithic Nanoporous Metals of Tunable Structural Hierarchy and Porosity. *Chem. Mater.*, 30(11):3894–3900, 2018.

[47] K. Sieradzki, J. S. Kim, A. T. Cole, and R. C. Newman. The relationship between dealloying and transgranular stress-corrosion cracking of cu-zn and cu-al alloys. *Journal of The Electrochemical Society*, 134(7):1635–1639, 1987.

[48] Z. Lu, C. Li, J. Han, F. Zhang, P. Liu, H. Wang, Z. Wang, C. Cheng, L. Chen, A. Hirata, T. Fujita, J. Erlebacher, and M. Chen. Three-dimensional bicontinuous nanoporous materials by vapor phase dealloying. *Nat. Commun.*, 9(1):1–7, 2018.

[49] T. Wada, K. Yubuta, A. Inoue, and H. Kato. Dealloying by metallic melt. *Mater. Lett.*, 65(7):1076–1078, 2011.

[50] T. Wada, A. D. Setyawan, Ku. Yubuta, and H. Kato. Nano- to submicro-porous β-Ti alloy prepared from dealloying in a metallic melt. *Scr. Mater.*, 65(6):532–535, 2011.

[51] I. McCue, A. Karma, and J. Erlebacher. Pattern formation during electrochemical and liquid metal dealloying. *MRS Bull.*, 43(1):27–34, 2018.

[52] R. Li and K. Sieradzki. Ductile-brittle transition in random porous Au. *Phys. Rev. Lett.*, 68(8):1168–1171, 1992.

[53] J. Erlebacher, M. J. Aziz, A. Karma, N. Dimitrov, and K. Sieradzki. Evolution of nanoporosity in dealloying. *Nature*, 410(6827):450–453, 2001.

[54] N. A. Senior and R. C. Newman. Synthesis of tough nanoporous metals by controlled electrolytic dealloying. *Nanotechnology*, 17(9):2311–2316, 2006.

[55] J. Weissmüller and K. Sieradzki. Dealloyed nanoporous materials with interface-controlled behavior. *MRS Bull.*, 43(01):14–19, 2018.

[56] T. Wada and H. Kato. Three-dimensional open-cell macroporous iron, chromium and ferritic stainless steel. *Scr. Mater.*, 68(9):723–726, 2013.

[57] J. W. Kim, M. Tsuda, T. Wada, K. Yubuta, S. G. Kim, and H. Kato. Optimizing niobium dealloying with metallic melt to fabricate porous structure for electrolytic capacitors. *Acta Mater.*, 84:497–505, 2015.

[58] I. V. Okulov, A. V. Okulov, I. V. Soldatov, B. Luthringer, R. Willumeit-Römer, T. Wada, H. Kato, J. Weissmüller, and J. Markmann. Open porous dealloying-based biomaterials as a novel biomaterial platform. *Mater. Sci. Eng. C.*, 88:95–103, 2018.

[59] Z. Dan, F. Qin, Y. Sugawara, I. Muto, and N. Hara. Fabrication of nanoporous copper by dealloying amorphous binary Ti–Cu alloys in hydrofluoric acid solutions. *Intermetallics*, 29:14–20, 2012.

[60] Y. Jin, R. Li, and T. Zhang. Formation of nanoporous silver by dealloying Ca–Ag metallic glasses in water. *Intermetallics*, 67:166–170, 2015.

[61] H.-J. Jin, L. Kurmanaeva, J. Schmauch, H. Rösner, Y. Ivanisenko, and J. Weissmüller. Deforming nanoporous metal: Role of lattice coherency. *Acta Mater.*, 57(9):2665–2672, 2009.

[62] T. J. Balk, C. Eberl, Y. Sun, K. J. Hemker, and D. S. Gianola. Tensile and compressive microspecimen testing of bulk nanoporous gold. *JOM*, 61(12):26–31, 2009.

[63] N. Mameka, K. Wang, J. Markmann, E. T. Lilleodden, and J. Weissmüller. Nanoporous Gold—Testing Macro-scale Samples to Probe Small-scale Mechanical Behavior. *Mater. Res. Lett.*, 4(1):27–36, 2016.

[64] J. R. Hayes, A. M. Hodge, J. Biener, A. V. Hamza, and K. Sieradzki. Monolithic nanoporous copper by dealloying Mn-Cu. *J. Mater. Res.*, 21(10):2611–2616, 2006.

[65] Y. Sun, K. P. Kucera, S. A. Burger, and T. J. Balk. Microstructure, stability and thermomechanical behavior of crack-free thin films of nanoporous gold. *Scr. Mater.*, 58(11):1018–1021, 2008.

[66] R. Zeis, T. Lei, K. Sieradzki, J. Snyder, and J. Erlebacher. Catalytic reduction of oxygen and hydrogen peroxide by nanoporous gold. *J. Catal.*, 253(1):132–138, 2008.

[67] J. Weissmüller, R. C. Newman, H.-J. Jin, A. M. Hodge, and J. W. Kysar. Nanoporous Metals by Alloy Corrosion: Formation and Mechanical Properties. *MRS Bull.*, 34(08):577–586, 2009.

[68] M. Bürckert, N. J. Briot, and T. J. Balk. Uniaxial compression testing of bulk nanoporous gold. *Philos. Mag.*, 6435:1–22, 2017.

[69] X.-L. Ye and H.-J. Jin. Corrosion-Induced Strengthening: Development of High-Strength Nanoporous Metals. *Adv. Eng. Mater.*, 18(6):1050–1058, 2016.

[70] H.-J. Jin, D. Kramer, Y. Ivanisenko, and J. Weissmüller. Macroscopically Strong Nanoporous Pt Prepared by Dealloying. *Adv. Eng. Mater.*, 9(10):849–854, 2007.

[71] S. Shi, J. Markmann, and J. Weissmüller. Actuation by hydrogen electrosorption in hierarchical nanoporous palladium. *Philos. Mag.*, 97(19):1571–1587, 2017.

[72] S. Shi, J. Markmann, and J. Weissmüller. Synthesis of uniform bulk nanoporous palladium with tunable structure. *Electrochim. Acta*, 285:60–69, 2018.

[73] A. F. Holleman, N. Wiberg, E. Wiberg, and G. Fischer. *Lehrbuch der Anorganischen Chemie*. Walter de Gruyter, Berlin • New York, 2007.

[74] B. Tang, M. Zhou, R. Zhou, P. F. Bai, and G. F. Zhou. Well-Ordered Nanoporous Copper Fabricated by Dealloying Cu-Mn and its Characterizations. *Key Eng. Mater.*, 693:662–668, 2016.

[75] I. C. Cheng and A. M. Hodge. Morphology, Oxidation, and Mechanical Behavior of Nanoporous Cu Foams. *Adv. Eng. Mater.*, 14(4):219–226, 2012.

[76] T. Egle, C. Barroo, N. Janvelyan, A. C. Baumgaertel, A. J. Akey, M. M. Biener, C. M. Friend, D. C. Bell, and J. Biener. Multiscale Morphology of Nanoporous Copper Made from Intermetallic Phases. *ACS Appl. Mater. Interfaces*, 9(30):25615–25622, aug 2017.

[77] Q. Kong, L. Lian, Y. Liu, and J. Zhang. Fabrication and compression properties of bulk hierarchical nanoporous copper with fine ligament. *Mater. Lett.*, 127:59–62, 2014.

[78] F. Chen, X. Chen, L. Zou, Y. Yao, Y. Lin, Q. Shen, E. J. Lavernia, and L. Zhang. Fabrication and mechanical behavior of bulk nanoporous Cu via chemical dealloying of Cu-Al alloys. *Mater. Sci. Eng. A*, 660:241–250, 2016.

[79] A. I. Heim. Corrosion Resistance of Copper and Copper Alloys. *Ind. Eng. Chem.*, 49(8):63A–66A, 1957.

[80] D. J. G. Ives and A. E. Rawson. Copper Corrosion. *J. Electrochem. Soc.*, 109(6):447–451, 1962.

[81] D. E. Davies and W. Barker. Influence of pH on Corrosion and Passivation of Nickel. *Corrosion*, 20(2):47t–53t, 1964.

[82] S. J. Rosenberg. Nickel and its alloys. Technical report, National Bureau of Standards Monograph 106, Washington, 1968.

[83] M. Hakamada and M. Mabuchi. Preparation of nanoporous Ni and Ni-Cu by dealloying of rolled Ni-Mn and Ni-Cu-Mn alloys. *J. Alloys Compd.*, 485(1-2):583–587, 2009.

[84] M. Hakamada, M. Takahashi, T. Furukawa, and M. Mabuchi. Coercivity of nanoporous Ni produced by dealloying. *Appl. Phys. Lett.*, 94(2009):15–17, 2009.

[85] Z. Dan, F. Qin, Y. Sugawara, I. Muto, and N. Hara. Bimodal nanoporous nickel prepared by dealloying Ni38Mn62 alloys. *Intermetallics*, 31:157–164, 2012.

[86] M. Hakamada and M. Mabuchi. Nanoporous nickel fabricated by dealloying of rolled Ni-Mn sheet. *Procedia Eng.*, 81:2159–2164, 2014.

[87] C. Cheng, L. Lührs, T. Krekeler, M. Ritter, and J. Weissmüller. Semiordered Hierarchical Metallic Network for Fast and Large Charge-Induced Strain. *Nano Lett.*, 17(8):4774–4780, 2017.

[88] H. J. Qiu, J. L. Kang, P. Liu, A. Hirata, T. Fujita, and M. Chen. Fabrication of large-scale nanoporous nickel with a tunable pore size for energy storage. *J. Power Sources*, 247:896–905, 2014.

[89] M. Hakamada, S. Matsumura, and M. Mabuchi. Electrochemical actuation of nanoporous Ni in NaOH solution. *Mater. Lett.*, 70:132–134, 2012.

[90] Q. Bai, Y. Wang, J. Zhang, Y. Ding, Z. Peng, and Z. Zhang. Hierarchically nanoporous nickel-based actuators with giant reversible strain and ultrahigh work density. *J. Mater. Chem. C*, 4(1):45–52, 2016.

[91] C. Cheng and A. H. W. Ngan. Reversible electrochemical actuation of metallic nanohoneycombs induced by pseudocapacitive redox processes. *ACS Nano*, 9(4):3984–3995, 2015.

[92] C. Cheng, J. Weissmüller, and A. H. W. Ngan. Fast and Reversible Actuation of Metallic Muscles Composed of Nickel Nanowire-Forest. *Adv. Mater.*, 28(26):5315–5321, 2016.

[93] G. Dieter. *Mechanical metallurgy.* McGraw-Hill, London New York, 1988.

[94] O. Kraft, P. A. Gruber, R. Mönig, and D. Weygand. Plasticity in Confined Dimensions. *Annu. Rev. Mater. Res.*, 40(1):293–317, 2010.

[95] J. R. Greer and W. D. Nix. Size dependence of mechanical properties of gold at the sub-micron scale. *Appl. Phys. A Mater. Sci. Process.*, 80(8):1625–1629, 2005.

[96] J. R. Greer, W. C. Oliver, and W. D. Nix. Size dependence of mechanical properties of gold at the micron scale in the absence of strain gradients. *Acta Mater.*, 53(6):1821–1830, 2005.

[97] C. A. Volkert and E. T. Lilleodden. Size effects in the deformation of sub-micron Au columns. *Philos. Mag.*, 86(33-35):5567–5579, 2006.

[98] M. D. Uchic, P. A. Shade, and D. M. Dimiduk. Plasticity of Micrometer-Scale Single Crystals in Compression. *Annu. Rev. Mater. Res.*, 39(1):361–386, 2009.

[99] J.-H. Seo, H. S. Park, Y. Yoo, T.-Y. Seong, J. Li, J.-P. Ahn, B. Kim, and I.-S. Choi. Origin of Size Dependency in Coherent-Twin-Propagation-Mediated Tensile Deformation of Noble Metal Nanowires. *Nano Lett.*, 13(11):5112–5116, 2013.

[100] H. Hirakata, K. Shimbara, T. Kondo, and K. Minoshima. Size effect on tensile creep behavior of micrometer-sized single-crystal gold. *Materialia*, 1(April):221–228, 2018.

[101] Z. W. Shan, R. K. Mishra, S. A. Syed Asif, O. L. Warren, and A. M. Minor. Mechanical annealing and source-limited deformation in submicrometre-diameter Ni crystals. *Nat. Mater.*, 7(2):115–119, 2008.

[102] T. A. Parthasarathy, S. I. Rao, D. M. Dimiduk, M. D. Uchic, and D. R. Trinkle. Contribution to size effect of yield strength from the stochastics of dislocation source lengths in finite samples. *Scr. Mater.*, 56(4):313–316, 2007.

[103] H. Tang, K. Schwarz, and H. Espinosa. Dislocation escape-related size effects in single-crystal micropillars under uniaxial compression. *Acta Mater.*, 55(5):1607–1616, 2007.

[104] S. I. Rao, D. M. Dimiduk, T. A. Parthasarathy, M. D. Uchic, M. Tang, and C. Woodward. Athermal mechanisms of size-dependent crystal flow gleaned from three-dimensional discrete dislocation simulations. *Acta Mater.*, 56(13):3245–3259, 2008.

[105] C. R. Weinberger and W. Cai. Surface-controlled dislocation multiplication in metal micropillars. *Proc. Natl. Acad. Sci.*, 105(38):14304–14307, 2008.

[106] S. H. Oh, M. Legros, D. Kiener, and G. Dehm. In situ observation of dislocation nucleation and escape in a submicrometre aluminium single crystal. *Nat. Mater.*, 8(2):95–100, 2009.

[107] D. Kiener and A. M. Minor. Source Truncation and Exhaustion: Insights from Quantitative in situ TEM Tensile Testing. *Nano Lett.*, 11(9):3816–3820, 2011.

[108] G. Richter, K. Hillerich, D. S. Gianola, R. Mönig, O. Kraft, and C. A. Volkert. Ultrahigh Strength Single Crystalline Nanowhiskers Grown by Physical Vapor Deposition. *Nano Lett.*, 9(8):3048–3052, 2009.

[109] K. Gall, J. Diao, and M. L. Dunn. The Strength of Gold Nanowires. *Nano Lett.*, 4(12):2431–2436, 2004.

[110] J. Marian and J. Knap. Breakdown of Self-Similar Hardening Behavior in Au Nanopillar Microplasticity. *Int. J. Multiscale Comput. Eng.*, 5(3-4):287–294, 2007.

[111] A. Danescu. The Asaro–Tiller–Grinfeld instability revisited. *Int. J. Solids Struct.*, 38(26-27):4671–4684, 2001.

[112] Y. Lu, J. Song, J. Y. Huang, and J. Lou. Fracture of Sub-20nm Ultrathin Gold Nanowires. *Adv. Funct. Mater.*, 21(20):3982–3989, 2011.

[113] L. Y. Chen, G. Richter, J. P. Sullivan, and D. S. Gianola. Lattice Anharmonicity in Defect-Free Pd Nanowhiskers. *Phys. Rev. Lett.*, 109(12):125503, 2012.

[114] G. Stan, S. Krylyuk, A. V. Davydov, M. Vaudin, L. A. Bendersky, and R. F. Cook. Surface effects on the elastic modulus of Te nanowires. *Appl. Phys. Lett.*, 92(24):241908, 2008.

[115] S. Cuenot, C. Frétigny, S. Demoustier-Champagne, and B. Nysten. Surface tension effect on the mechanical properties of nanomaterials measured by atomic force microscopy. *Phys. Rev. B*, 69(16):165410, 2004.

[116] X. Li, T. Ono, Y. Wang, and M. Esashi. Ultrathin single-crystalline-silicon cantilever resonators: Fabrication technology and significant specimen size effect on Young's modulus. *Appl. Phys. Lett.*, 83(15):3081–3083, 2003.

[117] S. G. Nilsson, X. Borrisé, and L. Montelius. Size effect on Young's modulus of thin chromium cantilevers. *Appl. Phys. Lett.*, 85(16):3555–3557, 2004.

[118] D. A. Smith, V. C. Holmberg, D. C. Lee, and B. A. Korgel. Young's Modulus and Size-Dependent Mechanical Quality Factor of Nanoelectromechanical Germanium Nanowire Resonators. *J. Phys. Chem. C*, 112(29):10725–10729, 2008.

[119] L. Qiao and X. Zheng. Effect of surface stress on the stiffness of micro/nanocantilevers: Nanowire elastic modulus measured by nano-scale tensile and vibrational techniques. *J. Appl. Phys.*, 113(1):013508, 2013.

[120] B. A. M. Elsner, S. Müller, S. Bargmann, and J. Weissmüller. Surface excess elasticity of gold: Ab initio coefficients and impact on the effective elastic response of nanowires. *Acta Mater.*, 124:468–477, 2017.

[121] H. Liang, M. Upmanyu, and H. Huang. Size-dependent elasticity of nanowires: Nonlinear effects. *Phys. Rev. B*, 71(24):241403, 2005.

[122] A. Ngô, B.-N. D.and Stukowski, N. Mameka, J. Markmann, K. Albe, and J. Weissmüller. Anomalous compliance and early yielding of nanoporous gold. *Acta Mater.*, 93:144–155, 2015.

[123] H.-J. Jin, J. Weissmüller, and D. Farkas. Mechanical response of nanoporous metals: A story of size, surface stress, and severed struts. *MRS Bull.*, 43(1):35–42, 2018.

[124] J. Biener, A. M. Hodge, A. V. Hamza, L. M. Hsiung, and J. H. Satcher. Nanoporous Au: A high yield strength material. *J. Appl. Phys.*, 97(2):024301–4, 2005.

[125] J. Biener, A. M. Hodge, J.R. Hayes, C. A. Volkert, L. A. Zepeda-Ruiz, A. V. Hamza, and F. F. Abraham. Size Effects on the Mechanical Behavior of Nanoporous Au. *Nano Lett.*, 6(10):2379–2382, 2006.

[126] M. Hakamada and M. Mabuchi. Mechanical strength of nanoporous gold fabricated by dealloying. *Scr. Mater.*, 56(11):1003–1006, 2007.

[127] A. M. Hodge, J. Biener, J. R. Hayes, P. M. Bythrow, C. A. Volkert, and A. V. Hamza. Scaling equation for yield strength of nanoporous open-cell foams. *Acta Mater.*, 55(4):1343–1349, 2007.

[128] N. J. Briot and T. J. Balk. Focused ion beam characterization of deformation resulting from nanoindentation of nanoporous gold. *MRS Commun.*, 8(01):132–136, 2018.

[129] L. J. Gibson and M. F. Ashby. *Cellular Solids*. Cambridge Solid State Science Series. Cambridge University Press, Cambridge, 2 edition, 1997.

[130] E. Andrews, W. Sanders, and L. J. Gibson. Compressive and tensile behaviour of aluminum foams. *Mater. Sci. Eng. A*, 270(2):113–124, 1999.

[131] X. Badiche, S. Forest, T. Guibert, Y. Bienvenu, J.-D. Bartout, P. Ienny, M. Croset, and H. Bernet. Mechanical properties and non-homogeneous deformation of open-cell nickel foams: application of the mechanics of cellular solids and of porous materials. *Mater. Sci. Eng. A*, 289(1):276–288, 2000.

[132] X.-Y. Sun, G.-K. Xu, X. Li, X.-Q. Feng, and H. Gao. Mechanical properties and scaling laws of nanoporous gold. *J. Appl. Phys.*, 113(2):023505, 2013.

[133] D. Lee, X. Wei, X. Chen, M. Zhao, S. C. Jun, J. Hone, E. G. Herbert, W. C. Oliver, and J. W. Kysar. Microfabrication and mechanical properties of nanoporous gold at the nanoscale. *Scr. Mater.*, 56(5):437–440, 2007.

[134] A. M. Hodge, R. T. Doucette, M. M. Biener, J. Biener, O. Cervantes, and A. V. Hamza. Ag effects on the elastic modulus values of nanoporous Au foams. *J. Mater. Res.*, 24(04):1600–1606, 2009.

[135] C. A. Volkert, E. T. Lilleodden, D. Kramer, and J. Weissmüller. Approaching the theoretical strength in nanoporous Au. *Appl. Phys. Lett.*, 89(6):061920–1, 2006.

[136] N. J. Briot, T. Kennerknecht, C. Eberl, and T. J. Balk. Mechanical properties of bulk single crystalline nanoporous gold investigated by millimetre-scale tension and compression testing. *Philos. Mag.*, 94(8):847–866, 2014.

[137] L.-Z. Liu, X.-L. Ye, and H.-J. Jin. Interpreting anomalous low-strength and low-stiffness of nanoporous gold: Quantification of network connectivity. *Acta Mater.*, 118:77–87, 2016.

[138] E. M. Savickij, editor. *Handbook of precious metals*. Hemisphere Publ., New York u.a., 1989.

[139] C. Soyarslan, S. Bargmann, M. Pradas, and J. Weissmüller. 3D stochastic bicontinuous microstructures: Generation, topology and elasticity. *Acta Mater.*, 149:326–340, 2018.

[140] Y. Sun, J. Ye, Z. Shan, A. M. Minor, and T. J. Balk. The mechanical behavior of nanoporous gold thin films. *JOM*, 59(9):54–58, 2007.

[141] R. Dou and B. Derby. Deformation mechanisms in gold nanowires and nanoporous gold. *Philos. Mag.*, 91(7-9):1070–1083, 2011.

[142] D. Farkas, A. Caro, E. Bringa, and D. Crowson. Mechanical response of nanoporous gold. *Acta Mater.*, 61(9):3249–3256, 2013.

[143] S. Parida, D. Kramer, C. A. Volkert, H. Rösner, J. Erlebacher, and J. Weissmüller. Volume change during the formation of nanoporous gold by dealloying. *Phys. Rev. Lett.*, 97(3):4–7, 2006.

[144] S. Van Petegem, S. Brandstetter, A. M. Hodge, B. S. El-Dasher, J. Biener, B. Schmitt, C. Borca, and H. Van Swygenhoven. On the microstructure of nanoporous gold: an X-ray diffraction study. *Nano Lett.*, 9(3):1158–1163, 2009.

[145] R. Dou and B. Derby. Strain gradients and the strength of nanoporous gold. *J. Mater. Res.*, 25(04):746–753, 2010.

[146] S. S. R. Saane, K. R. Mangipudi, K. U. Loos, J. Th. M. De Hosson, and P. R. Onck. Multiscale modeling of charge-induced deformation of nanoporous gold structures. *J. Mech. Phys. Solids*, 66:1–15, 2014.

[147] N. Huber, R. N. Viswanath, N. Mameka, J. Markmann, and J. Weißmüller. Scaling laws of nanoporous metals under uniaxial compression. *Acta Mater.*, 67:252–265, 2014.

[148] J. Jiao and N. Huber. Deformation mechanisms in nanoporous metals: Effect of ligament shape and disorder. *Comput. Mater. Sci.*, 127:194–203, 2017.

[149] E. T. Lilleodden and P. W. Voorhees. On the topological, morphological, and microstructural characterization of nanoporous metals. *MRS Bull.*, 43(01):20–26, 2018.

[150] L.-Z. Liu and H.-J. Jin. Scaling equation for the elastic modulus of nanoporous gold with "fixed" network connectivity. *Appl. Phys. Lett.*, 110(21):211902, 2017.

[151] J. Erlebacher. Mechanism of Coarsening and Bubble Formation in High-Genus Nanoporous Metals. *Phys. Rev. Lett.*, 106(22):225504, 2011.

[152] K. R. Mangipudi, E. Epler, and C. A. Volkert. Topology-dependent scaling laws for the stiffness and strength of nanoporous gold. *Acta Mater.*, 119:115–122, 2016.

[153] Y. Li, B.-N. Dinh Ngô, J. Markmann, and J. Weissmüller. Topology evolution during coarsening of nanoscale metal network structures. *Phys. Rev. Mater.*, 3(7):076001, 2019.

[154] K. Hu, M. Ziehmer, K. Wang, and E. T. Lilleodden. Nanoporous gold: 3D structural analyses of representative volumes and their implications on scaling relations of mechanical behaviour. *Philos. Mag.*, 96(32-34):3322–3335, 2016.

[155] M. Ziehmer, K. Hu, K. Wang, and E. T. Lilleodden. A principle curvatures analysis of the isothermal evolution of nanoporous gold: Quantifying the characteristic length-scales. *Acta Mater.*, 120:24–31, 2016.

[156] H. Jeon, N.-R. Kang, E.-J. Gwak, J. Jang, H. N. Han, J. Y. Hwang, S. Lee, and J.-Y. Kim. Self-similarity in the structure of coarsened nanoporous gold. *Scr. Mater.*, 137:46–49, 2017.

[157] N. Huber. Connections Between Topology and Macroscopic Mechanical Properties of Three-Dimensional Open-Pore Materials. *Front. Mater.*, 5, 2018.

[158] N. Badwe, X. Chen, and K. Sieradzki. Mechanical properties of nanoporous gold in tension. *Acta Mater.*, 129:251–258, 2017.

[159] E.-J. Gwak, H. Jeon, E. Song, N.-R. Kang, and J.-Y. Kim. Twinned nanoporous gold with enhanced tensile strength. *Acta Mater.*, 155(1-3):253–261, 2018.

[160] M. W. D. Van Der Burg, V. Shulmeister, E. Van Der Geissen, and R. Marissen. On the Linear Elastic Properties of Regular and Random Open-Cell Foam Models. *J. Cell. Plast.*, 33(1):31–54, 1997.

[161] J. Needham. *Science and Civilisation in China*, volume 5, part 2 of *Chemistry and chemical technology*. Cambridge University Press, 1974.

[162] B. C. Syrett. Erosion-Corrosion of Copper-Nickel Alloys in Sea Water and Other Aqueous Environments—A Literature Review. *Corrosion*, 32(6):242–252, 1976.

[163] K. C. Bendall. Corrosion resistant alloys — an industry-wide overview of applications. *Anti-Corrosion Methods Mater.*, 42(2):12–15, 1995.

[164] L. Lührs, C. Soyarslan, J. Markmann, S. Bargmann, and J. Weissmüller. Elastic and plastic Poisson's ratios of nanoporous gold. *Scr. Mater.*, 110:65–69, 2016.

[165] L. Lührs, B. Zandersons, N. Huber, and J. Weissmüller. Plastic Poisson's Ratio of Nanoporous Metals: A Macroscopic Signature of Tension–Compression Asymmetry at the Nanoscale. *Nano Lett.*, 17(10):6258–6266, 2017.

[166] L. Lührs and J. Weissmüller. Nanoporous Copper-Nickel – Macroscopic bodies of a strong and deformable nanoporous base metal by dealloying. *Scr. Mater.*, 155:119–123, 2018.

[167] J. Erlebacher and R. Seshadri. Hard Materials with Tunable Porosity. *MRS Bull.*, 34(08):561–568, 2009.

[168] J. Rugolo, J. Erlebacher, and K. Sieradzki. Length scales in alloy dissolution and measurement of absolute interfacial free energy. *Nat. Mater.*, 5(12):946–949, 2006.

[169] T. Krekeler, A. V. Straßer, M. Graf, K. Wang, C. Hartig, M. Ritter, and J. Weissmüller. Silver-rich clusters in nanoporous gold. *Mater. Res. Lett.*, 5(5):314–321, 2017.

[170] L. H. Qian and M. Chen. Ultrafine nanoporous gold by low-temperature dealloying and kinetics of nanopore formation. *Appl. Phys. Lett.*, 91(8):083105, 2007.

[171] Y. Ding, Y. J. Kim, and J. Erlebacher. Nanoporous Gold Leaf: "Ancient Technology "/Advanced Material. *Adv. Mater.*, 16(21):1897–1900, 2004.

[172] J. Snyder, P. Asanithi, A. B. Dalton, and J. Erlebacher. Stabilized Nanoporous Metals by Dealloying Ternary Alloy Precursors. *Adv. Mater.*, 20(24):4883–4886, 2008.

[173] H.-J. Butt and M. Kappl. *Surface and Interfacial Forces*. Wiley-VCH Verlag GmbH & Co. KGaA, Weinheim, Germany, 2 edition, 2018.

[174] R. Shuttleworth. The Surface Energies of Inert-gas and Ionic Crystals. *Proc. Phys. Soc. Sect. A*, 62(3):167–179, 1949.

[175] G. Wulff. XXV. Zur Frage der Geschwindigkeit des Wachsthums und der Auflösung der Krystallflächen. *Zeitschrift für Krist. - Cryst. Mater.*, 34(1-6), 1901.

[176] R. Shuttleworth. The Surface Tension of Solids. *Proc. Phys. Soc. Sect. A*, 63(5):444–457, 1950.

[177] J. Weissmüller and D. Kramer. Balance of Force at Curved Solid Metal-Liquid Electrolyte Interfaces. *Langmuir*, 21(10):4592–4603, 2005.

[178] J. W. Cahn. Thermodynamics of Solid and Fluid Surfaces. In *The Selected Works of John W. Cahn*, Wiley Online Books, pages 379–399. John Wiley & Sons, Inc., Hoboken, NJ, USA, 2013.

[179] J. Kollár, L. Vitos, J. M. Osorio-Guillén, and R. Ahuja. Calculation of surface stress for fcc transition metals. *Phys. Rev. B*, 68(24):245417, 2003.

[180] J. W. Gibbs. *Scientific Papers Of J. Willard Gibbs, Volume 1.* Longmans, Green and Company, 1906.

[181] C. Lemier and J. Weissmüller. Grain boundary segregation, stress and stretch: Effects on hydrogen absorption in nanocrystalline palladium. *Acta Mater.*, 55(4):1241–1254, 2007.

[182] D. Kramer and J. Weissmüller. A note on surface stress and surface tension and their interrelation via Shuttleworth's equation and the Lippmann equation. *Surf. Sci.*, 601(14):3042–3051, 2007.

[183] W. Haiss. Surface stress of clean and adsorbate-covered solids. *Reports Prog. Phys.*, 64(5):591–648, 2001.

[184] W. Haiss, R. J. Nichols, J. K. Sass, and K. P. Charle. Linear correlation between surface stress and surface charge in anion adsorption on Au(111). *J. Electroanal. Chem.*, 452(2):199–202, 1998.

[185] D. Kramer, R. N. Viswanath, and J. Weissmüller. Surface-stress induced macroscopic bending of nanoporous gold cantilevers. *Nano Lett.*, 4(5):793–796, 2004.

[186] G. Lippmann. Relations entre les phénomènes électriques et capillaires. *Ann. Chim. Phys.*, 5:494–549, 1875.

[187] D. C. Grahame. The Electrical Double Layer and the Theory of Electrocapillarity. *Chem. Rev.*, 41(3):441–501, 1947.

[188] D. Kramer. Dependence of surface stress, surface energy and surface tension on potential and charge. *Phys. Chem. Chem. Phys.*, 10(1):168–177, 2008.

[189] J. Diao, K. Gall, and M. L. Dunn. Yield Strength Asymmetry in Metal Nanowires. *Nano Lett.*, 4(10):1863–1867, 2004.

[190] J. Diao, K. Gall, M. L. Dunn, and J. A. Zimmerman. Atomistic simulations of the yielding of gold nanowires. *Acta Mater.*, 54(3):643–653, 2006.

[191] W. Zhang, T. Wang, and X. Chen. Effect of surface stress on the asymmetric yield strength of nanowires. *J. Appl. Phys.*, 103(12):123527, 2008.

[192] C. R. Weinberger and W. Cai. Plasticity of metal nanowires. *J. Mater. Chem.*, 22(8):3277, 2012.

[193] J. Weissmüller and J. W. Cahn. Mean stresses in microstructures due to interface stresses: A generalization of a capillary equation for solids. *Acta Mater.*, 45(5):1899–1906, 1997.

[194] Y. Umeno, C. Elsässer, B. Meyer, P. Gumbsch, M. Nothacker, J. Weissmüller, and F. Evers. Ab initio study of surface stress response to charging. *Europhys. Lett.*, 78(1):13001, 2007.

[195] H. Udin, A. J. Schaler, and J. Wulff. The surface tension of solid copper. *Trans. AIME*, 185(2):186–190, 1949.

[196] F. H. Buttner, H. Udin, and J. Wulff. The surface tension of solid gold. *Trans. AIME*, 191(12):1209–1211, 1951.

[197] D. Josell and F. Spaepen. Determination of the interfacial tension by zero creep experiments on multilayers – ii. Experiment. *Acta Metall. Mater.*, 41(10):3017–3027, 1993.

[198] A. Pfützenreuter and G. Masing. Zunahme der Geschwindigkeit des Plastischen Fliessens von Metallen im Elektrolyten bei der Electrochemischen Polarisation. *Z. Metallkd.*, 51(12):361–370, 1951.

[199] R. W. Revie and H. H. Uhlig. Effect of applied potential and surface dissolution on the creep behavior of copper. *Acta Metall.*, 22(5):619–627, 1974.

[200] C. J. van der Wekken. The effect of cathodic polarization on the creep rate of gold. *J. Electrochem. Soc.*, 129(4):706–711, 1982.

[201] R. M. Latanision, H. Opperhauser Jr., and A. R. C. Westwood. The influence of surface charge density on the fracture of zinc single crystal electrodes. *Scripta Metall.*, 12(5):475–479, 1978.

[202] F. Hild and S. Roux. Digital Image Correlation: from Displacement Measurement to Identification of Elastic Properties - a Review. *Strain*, 42(2):69–80, 2006.

[203] A-F. Bastawros, H. Bart-Smith, and A.G. Evans. Experimental analysis of deformation mechanisms in a closed-cell aluminum alloy foam. *J. Mech. Phys. Solids*, 48(2):301 – 322, 2000.

[204] S. Cho, I. Chasiotis, T. A. Friedmann, and J. P. Sullivan. Young's modulus, Poisson's ratio and failure properties of tetrahedral amorphous diamond-like carbon for MEMS devices. *J. Micromechanics Microengineering*, 15(4):728–735, 2005.

[205] H. Schreier, J.-J. Orteu, and M. A. Sutton. *Image Correlation for Shape, Motion and Deformation Measurements*. Springer US, Boston, MA, 2009.

[206] H. Schreier and M. A. Sutton. Systematic Errors in Digital Image Correlation Due to Undermatched Subset Shape Functions. *Exp. Mech.*, 42(3):303–310, 2002.

[207] B. Pan, K. Qian, H. Xie, and A. Asundi. Two-dimensional digital image correlation for in-plane displacement and strain measurement: a review. *Meas. Sci. Technol.*, 20(6):062001, 2009.

[208] X. Gu, Y. Liang, and S. Fu. Evaluation and optimization of digital image correlation processing variables using genetic algorithm. *J. Strain Anal. Eng. Des.*, 51(6):408–415, 2016.

[209] T. C. Chu, W. F. Ranson, and M. A. Sutton. Applications of digital-image-correlation techniques to experimental mechanics. *Exp. Mech.*, 25(3):232–244, 1985.

[210] C. H. Hamann, A. Hamnett, and W. Vielstich. *Electrochemistry*. Wiley-VCH, Weinheim, 2 edition, 2007.

[211] J. N. Gaur and G. M. Schmid. Electrochemical behavior of gold in acidic chloride solutions. *J. Electroanal. Chem.*, 24(2-3):279–286, 1970.

[212] N. Perez. *Electrochemistry and Corrosion Science*. Kluwer Academic Publishers, 2004.

[213] B. E. Conway. Electrochemical oxide film formation at noble metals as a surface-chemical process. *Prog. Surf. Sci.*, 49(4):331–452, 1995.

[214] L. D. Burke, D. T. Buckley, and J. A. Morrissey. Novel view of the electrochemistry of gold. *Analyst*, 119(5):841, 1994.

[215] L. D. Burke and P. F. Nugent. The electrochemistry of gold: I the redox behaviour of the metal in aqueous media. *Gold Bull.*, 30(2):43–53, 1997.

[216] P. J. Spencer and J. N. Pratt. A study of the vapour pressure of manganese using a new high-temperature torsion - effusion apparatus. *Br. J. Appl. Phys.*, 18(10):1473–1478, 1967.

[217] V. E. Bazhenov. Phase diagram of the Cu-Ni-Mn system. *Russ. J. Non-Ferrous Met.*, 54(2):171–177, 2013.

[218] M. F. Ashby, A. G. Evans, N. A. Fleck, L. J. Gibson, J. W. Hutchinson, and H. N. G. Wadley. *Metal Foams: A Design Guide*. Butterworth-Heinemann, 2000.

[219] N. A. Gokcen. The Cu-Mn (Copper-Manganese) System. *J. Phase Equilibria*, 14(1):76–83, 1993.

[220] D. J. Chakrabarti, D. E. Laughlin, S. W. Chen, and Y. A. Chang. *Cu-Ni*, page 173. ASM International, Materials Park, OH, 2007.

[221] N. A. Gokcen. The Mn-Ni (Manganese-Nickel) System. *J. Phase Equilibria*, 12(3):313–321, 1991.

[222] J. D. Fritz and H. W. Pickering. Selective Anodic Dissolution of Cu-Au Alloys: TEM and Current Transient Study. *J. Electrochem. Soc.*, 138(11):3209, 1991.

[223] D. Bellet and L. Canham. Controlled drying: the key to better quality porous semiconductors. *Adv. Mater.*, 10(6):487–490, 1998.

[224] H. Okamoto and T. B. Massalski. The Ag-Au (Silver-Gold) system. *Bull. Alloy Phase Diagrams*, 4(1):30–38, 1983.

[225] S. Trasatti and O. A. Petrii. Real surface area measurements in electrochemistry. *J. Electroanal. Chem.*, 327(1-2):353–376, 1992.

[226] D. M. Kolb and J. Schneider. Surface reconstruction in electrochemistry: Au(100)-(5 x 20), Au(111)-(1 x 23) and Au(110)-(1 x 2). *Electrochim. Acta*, 31(8):929–936, 1986.

[227] A. E. Markaki and T. W. Clyne. The effect of cell wall microstructure on the deformation and fracture of aluminium-based foams. *Acta Mater.*, 49(9):1677–1686, 2001.

[228] P. Ahn and O. Balogun. Elastic characterization of nanoporous gold foams using laser based ultrasonics. *Ultrasonics*, 54(3):795–800, 2014.

[229] B. Roschning and N. Huber. Scaling laws of nanoporous gold under uniaxial compression: Effects of structural disorder on the solid fraction, elastic Poisson's ratio, Young's modulus and yield strength. *J. Mech. Phys. Solids*, 92:55–71, 2016.

[230] J. Kováčik. Correlation between Poisson's ratio and porosity in porous materials. *J. Mater. Sci.*, 41(4):1247–1249, 2006.

[231] T. Rouxel. Elastic Properties and Short-to Medium-Range Order in Glasses. *J. Am. Ceram. Soc.*, 90(10):3019–3039, 2007.

[232] G. N. Greaves, A. L. Greer, R. S. Lakes, and T. Rouxel. Poisson's ratio and modern materials. *Nat. Mater.*, 10(11):823–837, 2011.

[233] H. X. Zhu, J. F. Knott, and N. J. Mills. Analysis of the elastic properties of open-cell foams with tetrakaidecahedral cells. *J. Mech. Phys. Solids*, 45(3):319–343, 1997.

[234] V. Paserin, S. Marcuson, J. Shu, and D. S. Wilkinson. CVD technique for Inco nickel foam production. *Adv. Eng. Mater.*, 6(6):454–459, 2004.

[235] K. L. Calvert, K. P. Trumble, T. J. Webster, and L. A. Kirkpatrick. Characterization of commercial rigid polyurethane foams used as bone analogs for implant testing. *J. Mater. Sci. Mater. Med.*, 21(5):1453–1461, 2010.

[236] E. A. Friis, R. S. Lakes, and J. B. Park. Negative Poisson's ratio polymeric and metallic foams. *J. Mater. Sci.*, 23(12):4406–4414, 1988.

[237] D. Stauffer. *Introduction to percolation theory.* Taylor & Francis, London u.a., 2. ed. edition, 1992.

[238] J. P. Panakkal, H. Willems, and W. Arnold. Nondestructive evaluation of elastic parameters of sintered iron powder compacts. *J. Mater. Sci.*, 25(2):1397–1402, 1990.

[239] S. T. Szyniszewski, B. H. Smith, J. F. Hajjar, B. W. Schafer, and S. R. Arwade. The mechanical properties and modeling of a sintered hollow sphere steel foam. *Mater. Des.*, 54:1083–1094, 2014.

[240] M. C. Shaw and T. Sata. The plastic behavior of cellular materials. *Int. J. Mech. Sci.*, 8(7):469–478, 1966.

[241] H. Wang and M. Li. The ideal strength of gold under uniaxial stress: an ab initio study. *J. Phys. Condens. Matter*, 22(29):295405, 2010.

[242] H. E. Swanson and Tatge E. Standard X-ray Diffraction Powder Patterns. *Natl. Bur. Stand. (U.S.), Circ.*, 1(539):95, 1953.

[243] H. E. Swanson and Fuyat R. K. Standard X-ray Diffraction Powder Patterns. *Natl. Bur. Stand. (U.S.), Circ.*, 2(539):61, 1953.

[244] K. A. Shorlin, J. R. de Bruyn, M. Graham, and S. W. Morris. Development and geometry of isotropic and directional shrinkage-crack patterns. *Phys. Rev. E*, 61(6):6950–6957, 2000.

[245] L. Goehring and S. W. Morris. Order and disorder in columnar joints. *Europhys. Lett.*, 69(5):739–745, 2005.

[246] J. Ambrose, R. G. Barradas, and D. W. Shoesmith. Investigations of copper in aqueous alkaline solutions by cyclic voltammetry. *J. Electroanal. Chem. Interfacial Electrochem.*, 47(1):47–64, 1973.

[247] D. S. Hall, C. Bock, and B. R. MacDougall. The Electrochemistry of Metallic Nickel: Oxides, Hydroxides, Hydrides and Alkaline Hydrogen Evolution. *J. Electrochem. Soc.*, 160(3):F235–F243, 2013.

[248] B. Beverskog. Revised Pourbaix Diagrams for Copper at 25 to 300°C. *J. Electrochem. Soc.*, 144(10):3476, 1997.

[249] B. Beverskog and I. Puigdomenech. Revised Pourbaix diagrams for nickel at 25-300°C. *Corros. Sci.*, 39(5):969–980, 1997.

[250] M. J. Marcinkowski and N. Brown. Transformation—disorder to order in ni3mn. *Journal of Applied Physics*, 32(3):375–386, 1961.

[251] A. I. Lotkov, V. E. Panin, and V. P. Fadin. Kinetics of ordering in Ni3Mn alloy with additions of copper. *Sov. Phys. J.*, 20(3):306–309, 1977.

[252] A. I. Lotkov, V. E. Panin, V. P. Fadin, and V. V. Sarksyan. The nature of distribution of atoms, and its connection with electron structure in a number of ternary alloys on Ni3Mn basis. *Sov. Phys. J.*, 16(1):91–97, 1973.

[253] R. W. Cahn. Lattice parameter changes on disordering intermetallics. *Intermetallics*, 7(10):1089–1094, 1999.

[254] A. Watson, S. Wagner, E. Lysova, and L. Rokhlin. *Copper – Manganese – Nickel*, volume 11C3 of *Landolt-Börnstein - Group IV Physical Chemistry*. Springer, Berlin, Heidelberg, 2007.

[255] A. R. Miedema, P. F. de Châtel, and F. R. de Boer. Cohesion in alloys — fundamentals of a semi-empirical model. *Phys. B+C*, 100(1):1–28, 1980.

[256] A. M. Parvanian and M. Panjepour. Mechanical behavior improvement of open-pore copper foams synthesized through space holder technique. *Mater. Des.*, 49:834–841, 2013.

[257] N. Kränzlin and M. Niederberger. Wet-Chemical Preparation of Copper Foam Monoliths with Tunable Densities and Complex Macroscopic Shapes. *Adv. Mater.*, 25(39):5599–5604, 2013.

[258] M. Hakamada, Y. Asao, T. Kuromura, Y. Chen, H. Kusuda, and M. Mabuchi. Density dependence of the compressive properties of porous copper over a wide density range. *Acta Mater.*, 55(7):2291–2299, 2007.

[259] Y. Yamada, T. Banno, Z. K. Xie, Y. C. Li, and C. E. Wen. Preparation and Characterisation of Open-Cell Microporous Nickel. *Mater. Sci. Forum*, 539-543:1833–1838, 2007.

[260] S. L. Taylor, A. E. Jakus, R. N. Shah, and D. C. Dunand. Iron and Nickel Cellular Structures by Sintering of 3D-Printed Oxide or Metallic Particle Inks. *Adv. Eng. Mater.*, 19(11), 2017.

[261] H. Gleiter. *Korngrenzen in metallischen Werkstoffen*. Materialkundlich-Technische Reihe. Borntraeger, Stuttgart, 2. aufl edition, 1977.

[262] M. A. Meyers, A. Mishra, and D. J. Benson. Mechanical properties of nanocrystalline materials. *Prog. Mater. Sci.*, 51(4):427–556, 2006.

[263] Q. Wei, L. Kecskes, T. Jiao, K. T. Hartwig, K. T. Ramesh, and E. Ma. Adiabatic shear banding in ultrafine-grained Fe processed by severe plastic deformation. *Acta Mater.*, 52(7):1859–1869, 2004.

[264] A. I. Mardare, A. D. Yadav, A. P.and Wieck, M. Stratmann, and A. W. Hassel. Combinatorial electrochemistry on Al–Fe alloys. *Sci. Technol. Adv. Mater.*, 9(3):035009, 2008.

[265] Y. M. Kolotyrkin. The electrochemistry of alloys. *Electrochim. Acta*, 25(1):89–96, 1980.

[266] E. Detsi, P. Onck, and J. T. M. De Hosson. Metallic Muscles at Work: High Rate Actuation in Nanoporous Gold/Polyaniline Composites. *ACS Nano*, 7(5):4299–4306, 2013.

[267] B. Roschning and J. Weissmüller. Stress-charge coupling coefficient for thin-film polypyrrole actuators – Investigation of capacitive ion exchange in the oxidized state. *Electrochim. Acta*, 318:504–512, 2019.

[268] A. Quintana, E. Menéndez, E. Isarain-Chávez, J. Fornell, P. Solsona, F. Fauth, M. D. Baró, J. Nogués, E. Pellicer, and J. Sort. Tunable Magnetism in Nanoporous CuNi Alloys by Reversible Voltage-Driven Element-Selective Redox Processes. *Small*, 14(21):1704396, 2018.

[269] U. Herr, J. Jing, U. Gonser, and H. Gleiter. Alloy effects in consolidated binary mixtures of nanometer-sized crystals investigated by Mössbauer spectroscopy. *Solid State Commun.*, 76(2):197–202, 1990.

[270] G. Wilde. Nanostructures and nanocrystalline composite materials—synthesis, stability and phase transformations. *Surf. Interface Anal.*, 38(6):1047–1062, 2006.

[271] X. Wang, S. Wei, L. Xu, J. Li, X. Li, and K. Shan. Preparation of w–cu nanocomposite powders with high copper content using a chemical co-deposition technique. *Adv. Powder Technol.*, 29(6):1323–1330, 2018.

[272] H. Okamoto. *Fe-Mn*, page 197. ASM International, Materials Park, OH, 2007.

[273] K. Ishida and T. Nishizawa. The Co-Mn (Cobalt-Manganese) system. *Bull. Alloy Phase Diagrams*, 11(2):125–137, 1990.

[274] H. Okamoto. *Mn-V*, page 290. ASM International, Materials Park, OH, 2007.

[275] L. J. Swartzendruber, V. P. Itkin, and C. B. Alcock. The Fe-Ni (iron-nickel) system. *J. Phase Equilibria*, 12(3):288–312, 1991.